NORTHWESTERN UNIVERSITY

Continuum Modeling of Multidisperse and Polydisperse Granular Materials in Transient and Developing Flows

A DISSERTATION

SUBMITTED TO THE GRADUATE SCHOOL

IN PARTIAL FULFILLMENT OF THE REQUIREMENTS

for the degree

DOCTOR OF PHILOSOPHY

Field of Chemical and Biological Engineering

By

Zhekai Deng

EVANSTON, ILLINOIS

September 2019

© Copyright by Zhekai Deng 2019

All Rights Reserved

ABSTRACT

Continuum Modeling of Multidisperse and Polydisperse Granular Materials in Transient and Developing Flows

Zhekai Deng

Segregation of polydisperse granular materials remains to be a challenging problem in many industrial processes. However, most studies have focused either on bidisperse (two different particle size species) materials, which are not representative of most real mixtures, or on polydisperse materials in an idealized simple geometry. Additionally, most studies have focused on steady granular flows (time-independent flow kinematics), even though many flows encountered in industrial applications are unsteady (time-dependent flow kinematics).

To address these challenges, we study and extend the application of the modified continuum model for bidisperse segregation that captures the effects of segregation, diffusion, and advection to polydisperse (continuous distribution of particle size) segregating materials in three ways. First, we consider tridisperse (three different particle size species) size segregating flow in developing inclined chute flow, which is an important stepping stone between bidisperse segregation and polydisperse segregation. The continuum model is

validated using DEM simulations over a wide range of flow conditions. The approach accurately models tridisperse chute flow as indicated by the close agreement between its predictions and results from DEM simulations over a wide range of flow conditions including different incline angles, particle size distributions, flow rates, and flowing layer thicknesses. Second, we consider polydisperse segregating flow in developing segregation and transient segregation. In both cases, several terms in the model that were zero in the previously examined case of fully-developed streamwise-periodic steady segregation in a chute are now non-zero, which makes application of the model substantially more challenging. Predictions of the model agree quantitatively with experimentally validated discrete element method simulations of both size polydisperse and density polydisperse mixtures having uniform, triangular, and log-normal distributions. Finally, the continuum model is then extended to unsteady flows (time dependent flow kinematics) in feed-rate-modulated heap flow and hopper discharge flow, which could be viewed as a simplified version of industrial 3D conical heap filling and discharge operation. The model accurately predicts the segregation patterns inside the hopper and the discharge segregation profiles for both initially well-mixed and segregated conditions resulted from center filling. The agreement between experiment and continuum model further corroborates our modeling approach.

Acknowledgements

First of all, I thank my advisers Richard Lueptow, Paul Umbanhowar, and Julio Ottino. On academic level, all of them offered helpful comments and suggestions on my research and played a substantial role in shaping the research presented in this dissertation. Under their guidance, I become a much better scientist and engineer. On the personal level, all of them inspired me by their hardworking and passionate attitude towards life and work.

Besides my advisors, I thank my research collaborators, Conor Schlick, Austin Isner, Hongyi Xiao, Yongzhi (Sam) Zhao, and Yi Fan, who have influenced the my research. Conor helped get me started on numerical calculations for partial differential equations and also derived the general polydisperse equation, which later became the framework I worked on in my research. Austin developed GPU-based DEM simulation code which is used to validate the theoretical modeling that I have developed over the past several years. Hongyi performed a lot of experiments and extracted many elegant flow kinematics scalings, which were used in the latter part of this dissertation. Yongzhi, who was a visiting scholar in our lab, offered very helpful support on simulation code development. Yi, who left the lab before I joined the group, became my mentor at my Dow summer internship and provided helpful comments and suggestions for my project at Dow, which became a chapter in this dissertation.

In addition to Conor, Austin, Hongyi, Yongzhi, and Yi, I thank my other lab mates Darius Wheeler, Zafir ("Z") Zaman, Paul Park, Mengqi (Miki) Yu, Ryan Jones, Alexander Fry, Meng Shen, Thomas Lynn, Yifei Duan, Jing Lu, Song Gao, Mengying Wang, Suwei Liu, Adithya Shankar and Vidushi Dwivedi. Discussions with them about science and engineering positively affect my research. Discussion about non-research topics offered me a nice break from research. Because of these close-knit relationships and support we have for each other in our lab, Evanston and Chicago have become my home away from home.

I thank the ChBE faculty, specifically my committee members Linda Broadbelt and Wesley Burghardt. I also thank all the CHBE students I have known throughout my time at here. Both students and the faculty in CHBE have been supportive and helpful in teaching me the science and engineering knowledge that I need to know.

I also gratefully acknowledge financial support from NSF Grant CBET-1511450 and The Dow Chemical Company. At The Dow Chemical Company, I thank Karl Jacob, Madhusudhan Kodam, Yi Fan, Jim Koch, and Jörg Theuerkauf for helpful discussions.

Last but not least, I would like to thank my family and friends. This dissertation would not have been possible without their love, patience, and support.

Table of Contents

List of Tables

List of Figures

CHAPTER 1

Introduction

Granular flows are commonly encountered in many industrial settings. For example, many industrial processing units frequently handle granular materials such as pharmaceutical powders, agricultural products, and polymer pellets. Granular materials with different size, density or other material properties tend to segregate when they flow. However, in almost all industrial settings, segregation of granular materials is undesirable. For example, in the pharmaceutical industry, achieving a uniform mixture of the active pharmaceutical ingredients and excipient (fillers) is a key step to ensure drug efficacy and safety.

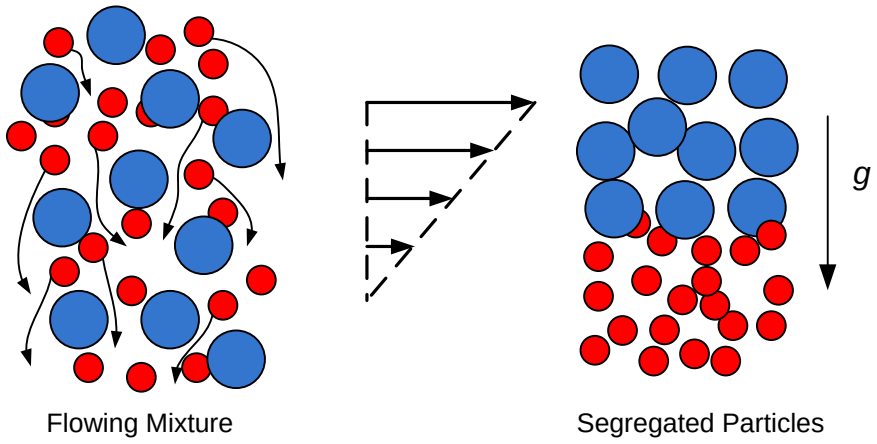

Figure 1.1. Segregation through particle percolation. Small particles fall through the voids between large particles under shear.

Despite its ubiquity and importance, segregation of polydisperse granular materials remains a challenging problem. Segregation of granular materials can be caused by differences in many material properties including size [86], density [102, 112], particle shape [119], and surface roughness [70]. Among these particle properties, size and density segregation are usually considered the most prominent mechanisms. Although many explanations have been proposed for the segregation mechanism, only a few studies have proposed a model that can predict segregation quantitatively because of the difficulty in capturing the relationship between local particle environment and particle segregation. As shown in figure 1.1, as an initially well bidisperse particle mixtures flows, small particles fall into the voids between large particles and percolate downward, resulting the large particles being pushed upward to the free surface. Consequently, this mechanism often leads to segregation, in which small particles are concentrated near the the bottom of the flow and large particles are concentrated near the free surface. In density driven segregation, due to the density difference between the light and heavy particles, light particles tend to rise toward the free surface, while heavy particles tend to sink toward the bottom of the flow. This mechanism often results similar segregation patterns to size segregation.

There is no universal governing equation for granular flow analogous to the Navier-Stokes equations for Newtonian fluid flow. As a result, most previous research [60, 86, 62, 81, 11, 47, 84, 26] has relied on canonical granular flow geometries including inclined chute, bounded heap, rotating tumbler and hopper flow, as shown in figure 1.2 , to better understand the granular flow kinematics and segregation scalings [76]. One way to study granular flows segregation and flow kinematics is through experiments through quasi-2D flows, in which the flow is confined within a narrow gap with thickness T to allow detailed

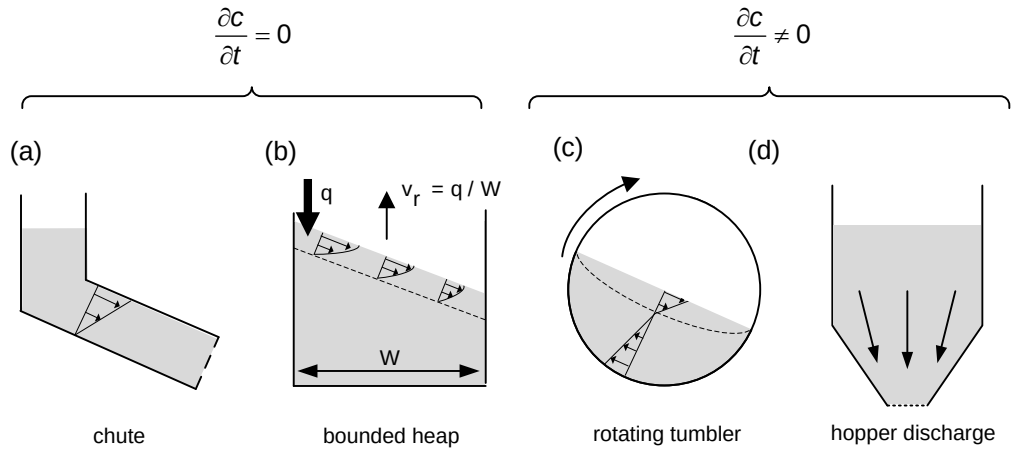

Figure 1.2. Canonical granular free surface flow geometries.

observation. These geometries are typically considered as simplified versions of 3D flows, which are frequently encountered in many industrial processes such as hopper filling.

As evident in figure 1.2, the simple chute flow makes it well-suited for the study of granular flows. As granular material flows down a chute, segregation drives the formation of layers enriched in a particular particle size. At steady state, the streamwise velocity in the chute flow remains essentially constant at different streamwise locations so the only thing that is changing with position is the particle concentration due to segregation. Flow in the bounded heap, shown in figure 1.2, is similar to chute flow in that particle concentration deposited on the heap is time-independent when feed flow rate is sufficient and constant. However, bounded heap flow differs from chute flow in that the velocity field is developing along the streamwise direction, which can affect the segregation. In quasi-2D one sided bounded heaps flows, particles mixtures are added to the heap at the top left corner at a volumetric feed rate Q. With a sufficient steady feed rate, a well mixed bidisperse particle mixture enters the heap at the top left feed zone and then particles

segregate as they flow downstream, resulting a small particle enriched region at the upstream portion of the heap and large particle enriched region at the downstream portion the heap. Flow in rotating tumblers, shown in figure 1.2, is similar to bounded heap flow in that the streamwise velocity and particle concentration both vary with streamwise position ($\frac{\partial}{\partial x} \neq 0$). However, rotating tumbler flow differs from steady bounded heap flow in that the segregation in rotating tumbler flow is transient ($\frac{\partial c}{\partial t} \neq 0$) during tumbler rotation. For initially mixed bidisperse particles in circular rotating tumbler flow, small particles percolate to the bottom of the flowing layer and deposit near the center of the tumbler, while large particles remain in the flowing layer and deposit near the periphery of the tumbler. Hopper discharge flow, on the other hand, differs from the chute flow, bounded heap flow, and rotating tumbler flow in that materials are first fed into the hopper and then discharged out of the hopper. As particles flow out of the hopper, particles initially on the center of the hopper flow out first followed by particles on the sidewalls. Consequently, the segregation in the hopper depends strongly on the detailed flow kinematics and initial conditions of the hopper.

A typical segregation pattern corresponding a quasi-2D heap is shown in figure 1.3 (a). When particle mixture flows, small (red) particles percolate downward within the thin surface flowing layer, segregate out of the flowing layer first, and deposit on the upstream portion of the heap, while large (blue) particles rise toward the free surface, flow further down the heap, and deposit on the downstream portion of the heap before they reach the downstream endwall. The result is a segregation pattern in the deposited heap with small particles deposited near the feed zone and large particles deposited further from the feed zone, as shown figure 1.3 (a).

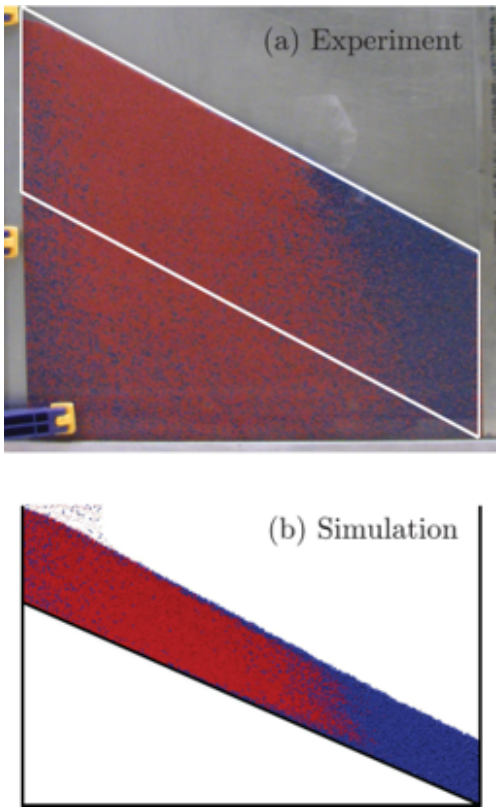

Figure 1.3. Segregation of a size bidisperse mixture (1 mm (red) and 2 mm (blue) glass sphere particles) of (a) experimental and (b) simulation in a quasi-2D bounded heap with width $W = 0.44$ m and gap thickness $T = 0.09$ m. Figure from Schlick et al. [89], ©2015 John Wiley & Sons.

While it is relatively easy to perform experiments and observe segregation phenomena using particles of different colors, measuring flow kinematics and extracting segregation parameters from experimental observations are often challenging and require sophisticated non-invasive experimental techniques. Alternatively, kinematics can also be explored by performing discrete element method (DEM) simulations to simulate and analyze particle flow. In DEM simulations, the forces on particles are calculated based on its contacts with other particles, and then each particle's velocity and position are updated according to Newton's Second Law at each time step. Due to increasing computation power, it is

possible to simulate millions of particles and achieve quantitative agreement with lab-scale experiment. This technique makes it possible to extract information that is difficult or impossible to obtain experimentally. An example of DEM simulation is shown in figure 1.3 (b), which demonstrates quantitative agreement between DEM simulation and experiment, justifying the use of DEM simulations. In DEM simulation, because the position and velocity are calculated at each time step, detailed flow kinematics such as concentration distribution, packing density, and stress distribution can be extracted easily. While DEM simulations can simulate lab-scale granular flow systems efficiently, it is still too computationally expensive to simulate large scale systems encountered in many industrial applications. For example, a typical industrial processing unit handles 10^{12} to 10^{14} particles, which is several orders of magnitude larger than what DEM simulations can currently candle (millions of particles). Consequently, DEM simulations are mainly used to understand the flow kinematics and extract segregation scalings. These scalings and parameters then become the inputs to the continuum model that can be solved quickly to quantitatively predict segregation.

Unlike experiments and DEM simulations, continuum models can be solved relatively quickly, thus allowing parametric studies to be performed. Additionally, and similiar to fluid flow, when governing equations are nondimensionalized, specific dimensionless parameters are identified. These dimensionless parameters control the system, yielding insight into the mechanisms that drive mixing and segregation. Various continuum models have been proposed for characterizing and modeling segregating granular flows. We focus on the advection-diffusion-segregation model derived from fluid mechanics, which

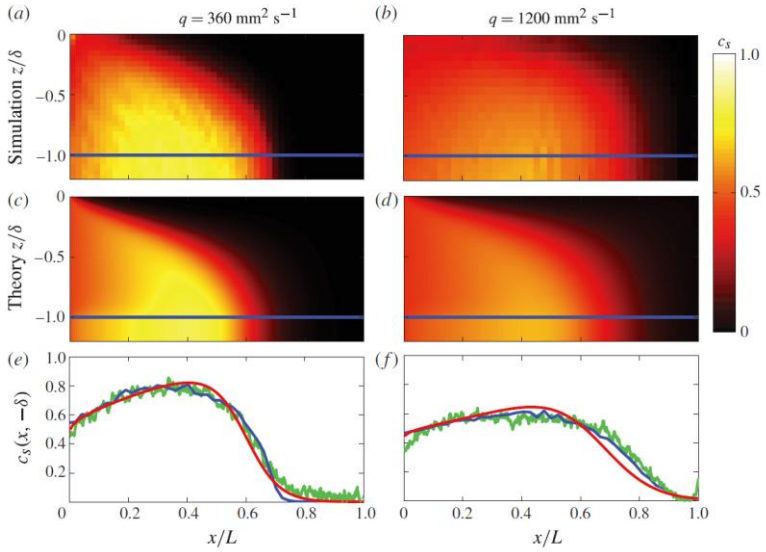

Figure 1.4. Comparision between continuum model, DEM simulations and experiments under the same operating conditions. Small-particle concentration from (a,b) DEM simulations and (c,d) continuum model. (e,f) Small-particle concentration, c_s, at the bottom of the flowing layer along the normalized streamwise location x/L, measured from DEM simulation (blue), continuum model (red), and experiment (green). Figure from [27], ©2014 Cambridge University Press.

describes how material is transported and mixed from a continuum viewpoint:

$$\frac{\partial c_i}{\partial t} + \underbrace{\nabla(\mathbf{u} \cdot c_i)}_{\text{advection}} + \underbrace{\frac{\partial (w_{p,i} c_i)}{\partial z}}_{\text{segregation}} = \underbrace{\nabla \cdot (D \nabla c_i)}_{\text{diffusion}}, \tag{1.1}$$

where for each species i, c_i is the particle species i concentration, $\boldsymbol{u}$ the velocity field, $w_{p,i}$ the relative segregation velocity, and D the diffusion coefficient. Here we define $w_{p,i} = w_i - \bar{w}$, that is, the normal direction velocity difference between particle species i with respect to the bulk mean flow. This approach is similar to previous approaches for modelling segregating granular flows [41, 42, 38, 100, 36, 72]. Numerically solving equation 1.1 with appropriate boundary conditions gives the local particle distribution of

segregating multidisperse granular materials. For example, figure 1.4 compares the small particle volume concentration contours at two different feed rates, predicted by equation 1.1 with results from DEM simulations. In both cases, the agreement is good. Similar quantitative agreement is also achieved when modeling segregation in size bidisperse quasi-2D tumbler flow [90], density bidisperse bounded heap flow [112], tridisperse bounded heap flow and polydispese periodic chute flow [91].

While bidisperse systems (two particle sizes or densities) are helpful in revealing segregation mechanism in the flow and in developing predictive model, almost no physical flow system involves only two particles species. In contrast, multidisperse and polydisperse systems (i.e. involving three or more monodisperse species or a continuous distribution of particular particle properties, respectively), even though far less studied, are nevertheless frequently encountered in many physical systems. Only a handful of studies have proposed models for polydisperse granular segregation, and these have been limited to idealized periodic chute flows in which periodic streamwise boundary conditions are used to model fully-developed segregation in a section of a chute [72, 71, 91]. While streamwise-periodic chute flow is suitable for initial model development, it is not representative of flows encountered in most physical systems. In this dissertation, we extend the application of the continuum model to substantially more challenging and realistic situations in both steady flows (time-independent kinematics) including developing (spatially-dependent) segregation in a bounded heap and transient (time-dependent) segregation in a rotating tumbler, and in unsteady flows (time-dependent kinematics) including modulated heap flow and hopper flow segregation.

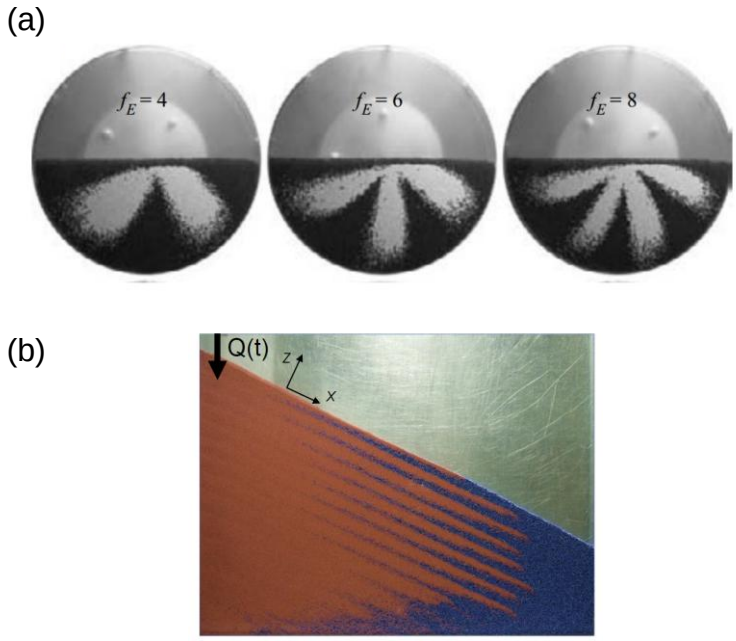

Figure 1.5. Segregation in unsteady flow. (a) Striped patterns produced using sinusoidal rotation rate modulation for mean frequencies of 4, 6, 8 cycles/rotation. Figure from [29], ©2005 Cambridge University Press. (b) Stratified pattern generated by feeding a bidisperse size mixture ($d_s = 0.5 \pm 0.04$ mm red particles and $d_l = 2.00 \pm 0.07$ mm blue particles) onto a quasi-2D bounded heap with a modulated 2D feed rate of $q_f = 23.6$ cm^2/s for $t_f = 5$ s and $q_s = 2.0$ cm^2/s for $t_s = 20s$. Figure from [113], ©2017 2017 Elsevier B.V..

The steady flow segregation (time-independent kinematics) cases described above are already challenging to understand and model. The unsteady flow segregation cases are even more challenging to understand and model. Because segregation depends strongly on flow kinematics, segregation in unsteady flow differs significantly from segregation in steady flow. The time dependent flow kinematics, which impacts the segregation of granular material in the normal direction, advection in the streamwise direction, and diffusion in both the normal and streamwise directions, controls the final particle distribution in the bed of particles below the flowing layer. Thus, a deeper understanding of the unsteady

flow kinematics is important to model the segregation mechanism for the modulated segregation pattern in the bounded heap and rotating tumbler. However, the few studies that focused on unsteady flow revealed complicated flow kinematics. In previous work [29], a rotating tumbler was forced with a sinusoidally-varying rotation speed to create striped patterns as shown in figure 1.5 (a). Another example is the stratification of particles in a quasi-2D heap. In figure 1.5 (b), a bidisperse particle mixture is alternately fed at a fast feed rate ($q_f = 37$ cm^2/s for a period $t_f = 3$ s) and a slow feed rate ($q_s = 0.4$ cm^2/s for a period $t_s = 62$ s). While the unsteady flows are significantly more challenging to understand and model, using the modulated feed rate offers the opportunity to intentionally create stripped granular layers that could potentially enhance streamwise mixing of the deposited materials on the heap. Additionally, in many industrial operations, the flow kinematics are unsteady due to unintentional modulation. For example, in hopper flow, as materials move downward toward the outlet, the materials in the surface flowing layer encounters different velocity at different depth of the hopper. Consequently, developing a predictive model that incorporates time dependent flow kinematics for polydisperse granular materials has important implications in many industrial processes.

1.1. Outline of the dissertation

In this dissertation, experiments, computational simulations, and theoretical modeling are utilized to understand granular flow and multidisperse and polydisperse segregation. A number of the chapters (Chaps. 2 and 3) are reproduced from published work and are preceded by a short introduction.

Chapter 2 describes multidisperse segregation in developing chute flows, and validates the model using DEM simulations over a wide range of flow conditions. Additionally, a parametric study of the influence of the dimensionless parameters demonstrates the effects of advection, segregation, and diffusion on multidisperse segregation.

Chapter 3 describes the results of extending the advection-diffusion-segregation continuum model to predict polydisperse size segregation (equal particle density) and polydisperse density segregation (equal particle size) in developing flow (bounded heap) and transient flow (rotating tumbler). Predictions of the model agree well with DEM simulation for both size polydisperse and density polydisperse mixtures over a wide range of operating conditions.

Chapter 4 applies the advection-diffusion-segregation continuum model to size bidisperse modulated heap flows. The results are validated against experiments.

Chapter 5 presents the results of applying the advection-diffusion-segregation continuum model to size polydisperse hopper flow, which consists of both hopper filling and hopper discharge operations. The results are validated against both DEM simulations and experiments.

Chapter 6 summarizes the main results of the dissertation and outlines possible future directions for the research.

CHAPTER 2

Continuum modeling of segregating tridisperse granular chute flow

Segregation and mixing of size multidisperse granular materials remain challenging problems in many industrial applications. In this chapter, we apply a continuum-based model that captures the effects of segregation, diffusion, and advection to size tridisperse granular flow in quasi-2D chute flow. The model takes as inputs the kinematics of the flow and other physical parameters such as the diffusion coefficient and the percolation length scale, quantities that can be determined directly from experiment, simulation or theory and that are not arbitrarily adjustable. The predictions from the model are consistent with experimentally validated discrete element method (DEM) simulations over a wide range of flow conditions and particle sizes. The degree of segregation depends on the Péclet number, Pe, defined as the ratio of the segregation rate to the diffusion rate, the relative segregation strength κ_{ij} between particle species i and j, and a characteristic length L, which is determined by the strength of segregation between the smallest and largest particles. A parametric study of particle size, κ_{ij}, Pe, and L demonstrates how particle segregation patterns depend on the interplay of advection, segregation, and diffusion. Finally, the segregation pattern is also affected by the velocity profile and the degree of basal slip at the chute bottom. The model is applicable to different flow geometries, and

should be easily adapted to segregation driven by other particle properties such as density and shape.

The material in this chapter was published in a slightly different form in Deng, *et al.,* "Continuum modeling of segregating tridisperse granular chute flow" *Proc R Soc A* (2018) [19] ©The Royal Society, reprinted with permission.

2.1. Introduction

Segregation of multidisperse granular materials is common in natural and industrial processes, such as landslides and processing of ores and polymers [4, 18, 45]. In gravity driven flows of initially well-mixed particles of different sizes, smaller particles fall through the interstices between larger particles causing size segregation. This mechanism is commonly referred to as particle percolation. In this chapter, we use a multidisperse segregation model to better understand the segregation of multidisperse mixtures in developing chute flow, and validate the model using DEM simulations over a wide range of flow conditions. While other researchers [36] have considered multidisperse developing segregation from a theoretical standpoint, here we utilize a segregation length scale unique to developing segregation, introduce a new non-dimensionalization scheme to accommodate multidisperse mixtures, and quantitatively compare the model results to DEM simulations. We further examine the effects of particle size, operating conditions (using dimensionless parameters), and the velocity profile on segregation in chute flow.

Most theoretical approaches to modelling segregation in granular flows have focused on bidisperse mixtures in order to understand the underlying mechanisms and develop predictive frameworks [21, 86, 22, 41, 42, 38, 100, 73, 110, 24, 99, 64, 104, 65]. Although

not as commonly studied, segregation in multidisperse (multi-component) systems made up of several discrete particle sizes and in polydisperse systems containing a range of particle sizes characterized by a continuous probability distribution, such as a log normal distribution have been explored both in experiments [80, 16, 46, 9] and in simulations using the discrete element method (DEM) [72, 46, 82, 9] for different flow geometries. In spite of this previous research, a generally applicable model for predicting multidisperse or polydisperse segregation is only now developing.

The simple geometry of chute flow makes it well-suited for the study of multidisperse and polydisperse flows. Over the past three decades, there has been substantial study of segregation in chute flow, see table 2.1 for a sample of past research on the topic. For example, Gray and Ancey [36] developed a continuum model to describe the segregation of flowing multidisperse mixtures based on the interaction of advection, segregation, and diffusion in the flowing layer. [72] developed a continuum model for polydisperse segregation that relies on a fitting parameter determined from DEM simulations. Recently, a stochastic lattice model incorporating the effects of segregation, mixing and crushing was used to predict steady-state grain size distributions in uniformly sheared granular flows [71]. Although this approach can connect micro- and macroscale advection-driven processes for polydisperse systems, it provides only qualitative agreement with experimentally measured grain size distributions. These and other models often include adjustable parameters, some of which are challenging to directly relate to physical quantities, making it difficult to apply the results to specific particle sizes, shapes, and densities or to generalize the model to a continuous distribution of particle sizes.

Table 2.1. A sample of past dense granular segregation research in chutes.

References	Methods	Dispersity
Savage and Lun [86]	Theory & Experiment	Bidisperse
Dolgunin et al. [22]	Theory & Experiment	Bidisperse
Dolgunin and Ukolov [21]	Theory & Experiment	Bidisperse
Gray and Thornton [41]	Theory	Bidisperse
Gray et al. [42]	Theory	Bidisperse
Gray and Chugunov [38]	Theory	Bidisperse
Thornton et al. [100]	Theory	Bidisperse
Wiederseiner et al. [110]	Theory & Experiment	Bidisperse
Thornton et al. [99]	DEM	Bidisperse
Tunuguntla et al. [104]	Theory & DEM	Bidisperse
Larcher and Jenkins [64]	Theory & DEM	Bidisperse
Larcher and Jenkins [65]	Theory & DEM	Bidisperse
Gray and Ancey [36]	Theory	Multidisperse
Marks et al. [72]	Theory & DEM	Polydisperse
Bhattacharya and McCarthy [9]	DEM & Experiment	Multi- & Polydisperse
Marks and Einav [71]	Theory	Polydisperse
Schlick et al. [91]	Theory & DEM	Multi- & Polydisperse

Recently, a continuum-based segregation model for bidisperse mixtures that was successfully applied to gravity-driven flows in quasi-2D bounded heaps [27] and circular tumblers [90] was extended to fully developed multi- and polydisperse segregation, where it demonstrated quantitative agreement with DEM simulation results [91]. The modeling approach utilizes segregation parameters and material-dependent scalings obtained from DEM simulations that are directly connected to the physics of segregation and are applicable to a wide range of flow rates, particle size ratios, particle size distributions, flow geometries, and even density driven segregation [112]. Here, we use this continuum modeling framework to examine the segregation of tridisperse (rather than bidisperse) granular mixtures for developing segregation (rather than fully developed segregation) in chute flow resulting from the interaction between advection, segregation, and diffusion. We further

introduce a new non-dimensionlization scheme for multidisperse systems incorporating a streamwise segregation length scale that characterizes developing segregation.

As granular material flows down a chute, segregation drives the formation of sublayers enriched in a particular particle size while, simultaneously, collisional diffusion acts to remix particles. The velocity field of the flow is determined by the chute's surface roughness and inclination angle as well as the volumetric flow rate. In steady state, the total streamwise flux of each species remains constant along the entire length of the chute. Sufficiently far downstream, fully developed segregation occurs in which there is a balance between segregation and diffusion, and, consequently, the concentration profiles of the material through the depth of the flowing layer remain constant.

Here we compare the theoretical predictions of our continuum modeling framework for tridisperse chute flow to results from equivalent DEM simulations and explore the model predictions for a range of parameters to gain insight into multidisperse segregation in developing flows. Even though the model and parameters can be easily extended to more than three particle species, the tridisperse system provides an important stepping stone between bidisperse and polydisperse systems and, at the same time, allows easy data visualization.

2.2. Segregation model

We consider size segregation of tridisperse granular materials flowing down a chute, shown schematically in figure 2.1 (a). The streamwise and normal directions are x and z, respectively, and the origin is at the most upstream position of the bottom of the flowing layer. A δ thick mixture of three particle sizes flows at volumetric flow rate,

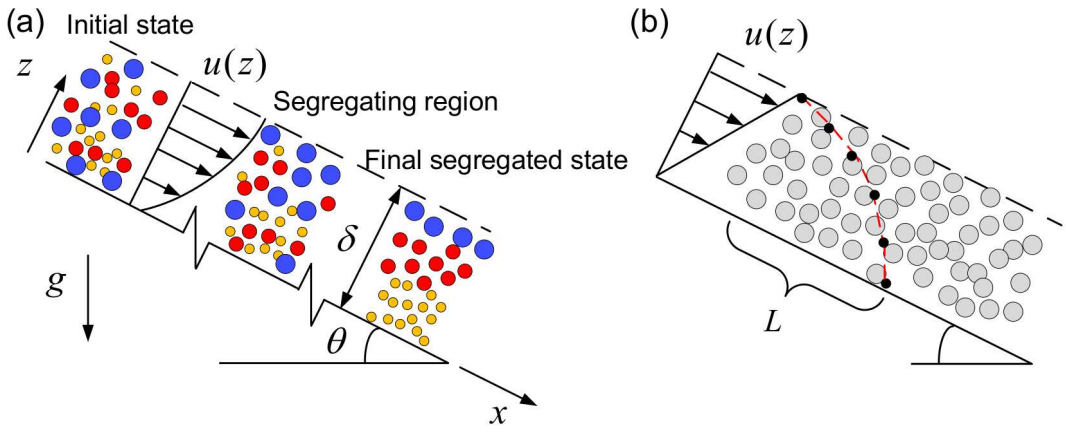

Figure 2.1. (a) Sketch of quasi-2D chute flow showing the flow geometry, evolution of the segregation, and a schematic streamwise velocity profile. (b) The characteristic streamwise segregation length scale, L, is defined as streamwise distance traveled by a small particle as it moves from the free surface to the bottom of a flowing layer composed of large particles at a characteristic streamwise surface velocity u_{surf}.

Q, down a chute inclined at angle θ with respect to horizontal with a fully developed velocity profile $u(z)$, that is assumed, to first order, to be independent of the local particle concentration. The gap thickness between the two side walls of the chute is T, and the two-dimensional flow rate is $q = Q/T$. While there can be streamwise variation in the flowing layer thickness under certain conditions [3, 110], here we assume that δ is constant for purpose of simplicity, similar to previous studies [110, 41, 36]. In section 2.4.1, we show that a constant value of δ reproduces spatial concentration fields consistent with DEM simulations.

The model is based on the scalar advection diffusion transport equation for the concentration of species i:

$$\frac{\partial c_i}{\partial t} + \nabla \cdot (\boldsymbol{u}_i c_i) = \nabla \cdot (D \nabla c_i), \tag{2.1}$$

where $\boldsymbol{u}_i$ is the velocity of species i, c_i is the volume concentration of species i, and D is the scalar collisional diffusion coefficient. For quasi-2D chute flow, we assume no net motion of species in the spanwise (y) direction (i.e. zero spanwise velocity $v_i = 0$). Consequently, $\boldsymbol{u}_i = u_i\hat{x} + w_i\hat{z}$ with streamwise and normal velocity components u_i and w_i, respectively, for species i. The streamwise velocity component of species i is written most generally as $u_i = u + u_{p,i}$, where $u_{p,i}$ is the streamwise component of the gravity-driven percolation velocity of species i relative to the mean streamwise flow velocity u. However, for this case and most other free surface flows, $u_{p,i} \ll u$ so that u_i can be accurately approximated as equal to u. The normal velocity component of species i is written as $w_i = w + w_{p,i}$, where $w_{p,i}$ is the segregation driving normal component of the percolation velocity of species i relative to the mean normal flow velocity w. With these assumptions, the transport equation 2.1 can be written as [27, 89, 90]

$$\frac{\partial c_i}{\partial t} + \frac{\partial (u c_i)}{\partial x} + \frac{\partial (w c_i)}{\partial z} + \frac{\partial (w_{p,i} c_i)}{\partial z} = D\frac{\partial^2 c_i}{\partial x^2} + D\frac{\partial^2 c_i}{\partial z^2}. \tag{2.2}$$

Although diffusion can be anisotropic [106], for simplicity we assume here that D is isotropic and homogeneous. This simplified assumption has yielded results that reproduce data from experiment and simulation in a variety of situations including plug flow [38], chute flow [72, 110, 99, 91], and bounded heap flow [27, 91, 112].

This approach to modeling segregation in flowing granular materials was first suggested by Bridgwater et al. [13] in a slightly different form. Over the last decades, many researchers have used similar approaches with a variety of expressions for the segregation flux, which is the last term of the left hand side of equation 2.2 [21, 22, 41, 36, 72, 104, 65].

Here we follow the form used by [27] and [90, 89, 91]. The key to the subsequent formulation of the model is the semi-empirical relation for the component of the segregation velocity normal to the free surface, $w_{p,i}$, which is derived from size bidisperse mixtures composed of particles with diameters α_i and α_j. The segregation velocity of species i depends on the local shear rate, $\dot{\gamma}$, and the concentration of the other species, c_j, as

$$w_{p,i} = S(\alpha_i, \alpha_j)\dot{\gamma}c_j, \tag{2.3}$$

where S is an empirically determined segregation length scale [27]. Equation 2.3 can be obtained by linearizing a more complicated expression for size segregation of bidisperse particles derived by Savage and Lun [86]. Gray and Ancey [36] used an approach similar to equation 2.3 except that their formulation did not explicitly include shear rate, $\dot{\gamma}$, which the [86] model requires to account for local effects due to relative flow that allow percolation to occur. We further note that equation 2.3 is applicable only to free surface flowing layers where the relatively small effects of lithostatic pressure on segregation are included in the coefficient $S(\alpha_i, \alpha_j)$, unlike other situations where there is a large overburden [34]. For spherical glass particles, the segregation length scale can be expressed as a function of the particle size ratio:

$$S(\alpha_i, \alpha_j) = B \min(\alpha_i, \alpha_j) \ln(\alpha_i/\alpha_j), \tag{2.4}$$

where ln is the natural logarithm and B is a constant dependent on intrinsic properties of the particles [89]. Based on DEM simulations of spherical glass particles in bidisperse bounded heap flow, $B = 0.26$ for particle size ratios in the range $1/3 \leq \alpha_i/\alpha_j \leq 3$ and $1 \text{ mm} \leq \alpha_i \leq 3 \text{ mm}$ [89]; we use this value of B for the rest of chapter.

Equations 2.3 and 2.4 capture the downward percolation of small particles and the upward movement of large particles in a flowing mixture. Equation 2.3 is based on the local shear rate and local particle concentrations, and, thus, is valid everywhere in dense, bidisperse, and gravity driven granular surface flows provided $\dot{\gamma}$ and c_j are known. Using equations 2.3 and 2.4 in the framework described above, quantitative agreement between segregation in the model, DEM simulations, and experiments has been demonstrated for size bidisperse flow in a bounded heap [27] and in a circular tumbler [90], and for density bidisperse flow in a bounded heap, where particle sizes α_i and α_j are replaced by particle densities ρ_i and ρ_j [112]. We note that there is a slight asymmetry in the segregation velocity for shear flows in which a small particle surrounded by large particles moves downward faster than a large particle surrounded by small particles moves upward [86, 34, 107, 32]. However, equation 2.3 captures the leading order behavior and is sufficient to accurately predict the overall behavior of segregating flows [90, 27, 91, 112]. It is possible to extend equation equation 2.3 and 2.4 to a wider size ratio as long as $S(\alpha_i, \alpha_j)$ can be measured from DEM simulations. Furthermore, for size ratios greater than about 6, "free sifting" occurs, in which small particles percolate between large particles without being significantly influenced by the large particle flow [92, 66, 25, 86]. The model described here will not properly account for the physics in this situation.

The expression for the segregation velocity in bidisperse mixtures (equation 2.3) was recently generalized to describe multidisperse (more than two different particle sizes) and polydisperse (continuous size distribution) segregation [91]. This generalization assumes that the segregation velocity of particle i depends on a linear combination of the segregation length scales $S(\alpha_i, \alpha_j)$ weighted by the corresponding concentration of each

surrounding species j, and neglects higher order interactions. For n distinct particle sizes in a mixture, each with diameter α_j and local concentration c_j, the percolation velocity is generalized to

$$w_{p,i} = \sum_{j=1}^{n} S(\alpha_i, \alpha_j)\dot{\gamma}c_j. \tag{2.5}$$

This equation differs from the approach used by [36] for a tridisperse mixture ($n = 3$) by virtue of the crucial explicit inclusion of the shear rate in equation 2.5 that allows the expression to describe the local flow effects. As will be shown later, it is necessary to include the shear rate to account for the impact of different velocity profiles that can occur in chute flow on the segregation. Equation 2.5 has a further advantage over the approach of [36] in that $S(\alpha_i, \alpha_j)$ can be defined purely in terms of the particle sizes (equation 2.4), whereas the [36] approach provides no means to determine their equivalent parameters. Equation 2.5 also differs from the approach proposed by [72], which includes a free parameter C (equation 3.2 of [72]), which was postulated to be related to particle shape, surface roughness, and the shear rate profile.

Substituting equation 2.5 into equation 2.2 yields the full scalar transport equations for particle mixtures with n distinct particle sizes:

$$\frac{\partial c_i}{\partial t} + \frac{\partial (uc_i)}{\partial x} + \frac{\partial (wc_i)}{\partial z} + \sum_{j=1}^{n} S(\alpha_i, \alpha_j)\frac{\partial}{\partial z}\left(\dot{\gamma}c_j c_i\right) = D\frac{\partial^2 c_i}{\partial x^2} + D\frac{\partial^2 c_i}{\partial z^2}. \tag{2.6}$$

Later in this chapter we demonstrate that the streamwise velocity profile, u, can be accurately assumed to be fully developed and independent of the local particle concentration or position along the length of the chute. Through conservation of mass, the overall mean particle velocity normal to the free surface, w, is zero. Consequently, the transport equation in the chute can be expressed as

$$\frac{\partial c_i}{\partial t} + u\frac{\partial c_i}{\partial x} + \sum_{j=1}^{n} S(\alpha_i, \alpha_j)\frac{\partial}{\partial z}\left(\dot{\gamma} c_j c_i\right) = D\frac{\partial^2 c_i}{\partial x^2} + D\frac{\partial^2 c_i}{\partial z^2}. \tag{2.7}$$

This system of n coupled partial differential equations can be simplified to $n-1$ partial differential equations because the sum of the species concentrations $\sum_{i=1}^{n} c_i = 1$. Equation 2.7 describes how the local volume concentration of species i is determined by advection due to the mean flow, segregation due to percolation, and diffusion due to random particle collisions. It includes the dependence of the segregation velocity on both the spatially varying local shear rate and the local particle concentrations, as well as the dependence of concentration on advection via the streamwise velocity u and diffusion via the diffusion coefficient D.

Equation 2.7 is non-dimensionalized using characteristic streamwise and normal length scales L and δ, respectively, and a characteristic streamwise surface velocity scale $2q/\delta$ as follows:

$$\tilde{x} = \frac{x}{L}, \quad \tilde{z} = \frac{z}{\delta}, \quad \tilde{t} = \frac{t}{\delta L/2q}, \quad \tilde{u} = \frac{u}{2q/\delta} \quad \text{and} \quad \tilde{\dot{\gamma}} = \frac{\dot{\gamma}}{2q/\delta^2}. \tag{2.8}$$

The dimensionless governing equation for the concentration of species i is then:

$$\frac{\partial c_i}{\partial \tilde{t}} + \tilde{u}\frac{\partial c_i}{\partial \tilde{x}} + \left(\frac{L}{\delta^2}\right)\left[\sum_{j=1}^{n} S(\alpha_i, \alpha_j)\frac{\partial}{\partial \tilde{z}}(\tilde{\dot{\gamma}} c_j c_i)\right] = \left(\frac{\delta}{2qL}\right) D\frac{\partial^2 c_i}{\partial \tilde{x}^2} + \left(\frac{L}{2q\delta}\right) D\frac{\partial^2 c_i}{\partial \tilde{z}^2}. \tag{2.9}$$

The streamwise segregation length scale, L, characterizing the developing segregation is based on the streamwise distance traveled by the smallest species, see figure 2.1 (b). The time for a small particle to move from the top to the bottom of a flowing layer is of order

$$t_s \propto \frac{\delta}{w_{p,i}}. \tag{2.10}$$

From equation 2.3, a small particle in a flowing layer comprised entirely of large particles has the characteristic segregation velocity

$$w_{p,i} \propto \langle\dot{\gamma}\rangle S_{l,s}, \tag{2.11}$$

where $\langle\dot{\gamma}\rangle$ is the depth averaged shear rate, and the subscripts l and s refer to the largest and smallest particles, respectively. We define the characteristic length scale, L, as the idealized streamwise displacement of the small particle as it moves from the free surface to the bottom of a flowing layer composed only of large particles:

$$L \propto u_{\text{surf}} t_s \propto \langle\dot{\gamma}\rangle\delta\frac{\delta}{\langle\dot{\gamma}\rangle S_{l,s}} \propto \frac{\delta^2}{S_{l,s}}, \tag{2.12}$$

where we assume that, regardless of its depth, the particle continues in the streamwise direction at the surface velocity, u_{surf}, which is the maximum velocity in the flowing layer. Since L is based on segregation for the smallest and largest species, it represents

the shortest segregation length scale in a multidisperse or polydisperse system and is independent of particle species concentration. A similar expression could be achieved using similar logic for a large particle to move from the bottom to the top of a flowing layer ignoring asymmetric segregation effects. An alternative definition characterizes the average velocity in the flowing layers as $u_{\text{surf}}/2$, assuming a velocity profile linear in depth. However, the difference is only a factor of 2, which we prefer to avoid for simplicity later on. The influence of L on the model predicted segregation is discussed in Section 2.5.

Substituting expression 2.12 into equation 2.9 yields

$$\frac{\partial c_i}{\partial \tilde{t}} + \tilde{u}\frac{\partial c_i}{\partial \tilde{x}} + \sum_{j=1}^{n} \kappa_{i,j}\frac{\partial}{\partial \tilde{z}}(\tilde{\dot{\gamma}} c_j c_i) = \left(\frac{S_{l,s}}{\delta}\right)^2 \frac{1}{Pe}\frac{\partial^2 c_i}{\partial \tilde{x}^2} + \frac{1}{Pe}\frac{\partial^2 c_i}{\partial \tilde{z}^2}, \tag{2.13}$$

where $\kappa_{i,j} = S_{i,j}/S_{l,s}$ and $Pe = 2qS_{l,s}/(\delta D)$. Since $S(\alpha_i, \alpha_j) = -S(\alpha_j, \alpha_i)$, it follows that $\kappa(\alpha_i, \alpha_j) = -\kappa(\alpha_j, \alpha_i)$, $\kappa_{l,s} = 1$, and $\kappa_{s,l} = -1$ by definition. Pe is the ratio of the diffusion time scale, δ^2/D, to the segregation time scale $L/(2q/\delta) = \delta L/2q = \delta^3/2qS_{l,s}$, and $\kappa(\alpha_i, \alpha_j)$ is the ratio of the segregation length for species i and species j to the segregation length for the smallest and largest species pair. $\kappa_{i,j}$ and Pe depend only on particle and flow properties, which are either determined directly by the control parameters of the problem (α_i and q) or can be directly measured from experiments or simulations (δ, S, and D).

$S(\alpha_i, \alpha_j)$ is $O(\bar{\alpha}/10)$ [90], where $\bar{\alpha}$ is the average particle diameter, and δ is generally $O(10\bar{\alpha})$ [3, 110]. Consequently, the ratio, $(S_{l,s}/\delta)^2$, in the streamwise diffusion term is $O(10^{-4})$. Thus, the first term on the right hand side of equation 2.13 can be safely ignored.

The non-dimensional multidisperse scalar transport equations can then be written as

$$\frac{\partial c_i}{\partial \tilde{t}} + \tilde{u}\frac{\partial c_i}{\partial \tilde{x}} + \sum_{j=1}^{n} \kappa_{i,j}\frac{\partial}{\partial \tilde{z}}(\tilde{\dot{\gamma}} c_j c_i) = \frac{1}{Pe}\frac{\partial^2 c_i}{\partial \tilde{z}^2}. \tag{2.14}$$

The boundary conditions for this equation are based on balancing the segregation flux with the diffusive flux at the top and bottom of the flowing layer ($\tilde{z} = 1$ and 0) [42]. Thus, at these two boundaries, the boundary conditions can be expressed as

$$\sum_{j=1}^{n} \kappa_{i,j}\frac{\partial}{\partial \tilde{z}}(\tilde{\dot{\gamma}} c_j c_i) = \frac{1}{Pe}\frac{\partial^2 c_i}{\partial \tilde{z}^2}. \tag{2.15}$$

Particles enter at the upstream end of the domain and exit at the downstream end of the domain via advection due to the streamwise velocity. Because $\kappa_{i,j} = -\kappa_{j,i}$ by definition, we use $\kappa_{i,j}$, where $\kappa_{i,j} \geq 0$, and replace $\kappa_{j,i}$ with $-\kappa_{i,j}$ in the rest of this chapter.

Lastly, because $\sum_{j=1}^{n} c_j = 1$, equations 2.14 for a tridisperse mixture ($n = 3$) can be expressed as

$$\begin{aligned} \tilde{u}\frac{\partial c_s}{\partial \tilde{x}} - \kappa_{l,s}\frac{\partial}{\partial \tilde{z}}\left[\tilde{\dot{\gamma}}(1 - c_m - c_s)c_s\right] - \kappa_{m,s}\frac{\partial}{\partial \tilde{z}}(\tilde{\dot{\gamma}} c_m c_s) &= \frac{1}{Pe}\frac{\partial^2 c_s}{\partial \tilde{z}^2} \\ \tilde{u}\frac{\partial c_m}{\partial \tilde{x}} + \kappa_{m,s}\frac{\partial}{\partial \tilde{z}}(\tilde{\dot{\gamma}} c_s c_m) - \kappa_{l,m}\frac{\partial}{\partial \tilde{z}}\left[\tilde{\dot{\gamma}}(1 - c_s - c_m)c_m\right] &= \frac{1}{Pe}\frac{\partial^2 c_m}{\partial \tilde{z}^2}, \end{aligned} \tag{2.16}$$

for steady flow, where s, m, and l represent small, medium and large size particle species, respectively.

They can be solved using standard initial boundary-value routines for systems of parabolic equations. Here, the *pdepe* routine in Matlab is used. The inlet concentration profiles can be arbitrarily specified (e.g., perfectly mixed or perfectly segregated) or can

be based on concentration profiles measured from experiments or DEM simulations. The streamwise velocity profile $\tilde{u}$ is assumed to be fully developed and independent of the local particle concentration or position along the length of the chute, though these assumptions are not required to apply the formalism. The boundary conditions (equations 2.15) at the free surface and the bottom of flowing layer can be specified in terms of the fluxes of small and medium particles as

$$\begin{aligned} -\kappa_{l,s}\frac{\partial}{\partial\tilde{z}}\left[\tilde{\dot{\gamma}}(1-c_m-c_s)c_s\right] - \kappa_{m,s}\frac{\partial}{\partial\tilde{z}}(\tilde{\dot{\gamma}}c_m c_s) &= \frac{1}{Pe}\frac{\partial^2 c_s}{\partial\tilde{z}^2}, \\ \kappa_{m,s}\frac{\partial}{\partial\tilde{z}}(\tilde{\dot{\gamma}}c_s c_m) - \kappa_{l,m}\frac{\partial}{\partial\tilde{z}}\left[\tilde{\dot{\gamma}}(1-c_s-c_m)c_m\right] &= \frac{1}{Pe}\frac{\partial^2 c_m}{\partial\tilde{z}^2}. \end{aligned} \tag{2.17}$$

Numerically, the inlet values for concentration are integrated forward from $\tilde{x} = 0$ to the furthest downstream extent of the flow to determine the concentrations of small and medium particle species c_s and c_m, respectively. The large particle concentration is $c_l = 1 - c_s - c_m$.

2.3. DEM Simulations and Flow Kinematics

To validate the predictions of the model and to acquire necessary kinematic information for the model, DEM simulations of a tridisperse mixture of spherical glass particles in a developing chute flow are performed based on the flow geometry shown in figure 2.2. Particles are dispensed from a vertical channel at volumetric flow rate Q. At a given chute angle, θ, and below a critical flow rate, q_c, the flowing layer thickness, δ, is essentially constant [3]. For the DEM simulation example presented below, an equal volume by component particle mixture with mean particle diameters, $\alpha_i = 2$, 3.2, and 5 mm

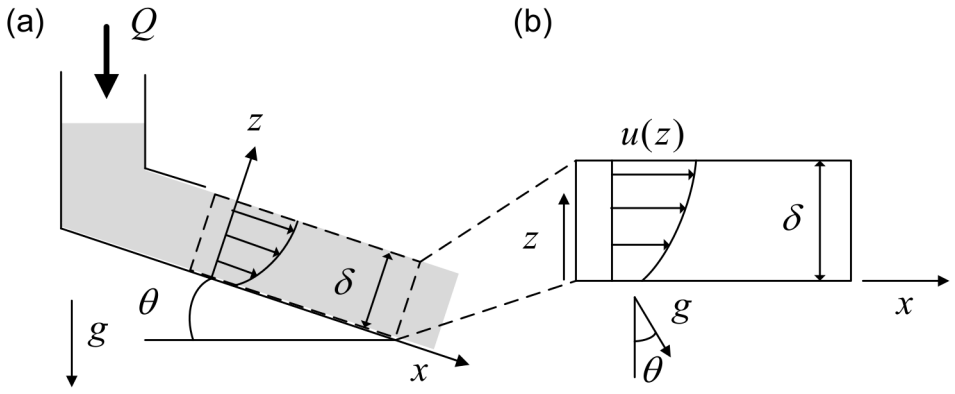

Figure 2.2. (a) Sketch of quasi-2D segregating chute flow with transverse gap thickness T and chute angle θ. Granular material is fed into the chute at a volumetric feed rate Q. (b) Sketch of the computational domain in a rotated coordinate system.

(corresponding to size ratios of $R = 1 : 1.6 : 2.5$ with respect to the smallest particle) and density $\rho = 2500$ kg/m^3 flows down a 2.5 cm wide chute inclined at an angle of $\theta = 26.5°$ with a simulated flowing length $l = 0.7$ m. To reduce particle ordering, the diameter of each species is distributed uniformly between 0.95 α_i and 1.05 α_i for all DEM simulations. The parameter κ_{ij} is based on the mean diameters. The bottom wall boundary condition is set such that particles that initially contact the flat bottom wall are immobilized to increase surface roughness and friction. Thereafter, all particles flow over these immobilized particles. The smooth, flat vertical side wall uses the same parameters as the particle-particle interaction. The DEM simulation parameters used here have been validated by numerous experiments using spherical glass particles; further details of the DEM methodology can be found in related publications [14, 117, 118, 26, 27, 112, 91] and Appendix A.

To implement the segregation model for tridisperse mixtures, the flowing layer depth, velocity profile, and diffusion coefficient are needed. Here, these characteristics of the flow

are measured from the DEM simulations. However, DEM simulations are not necessary to determine the parameters used in the model. For instance, the diffusion coefficient can come from correlations based on shear rate and particle size [89, 28]; the velocity profile can be based on theory, such as the Bagnold profile [6, 76], and so on. In all cases, the model results are calculated using parameters derived directly from the flow. Parameter values used in the model are either measured from DEM simulations, use values from previous studies based on bidisperse mixtures of particles, or are based on standard velocity profiles typical of chute flow. In other words, if S, D, and the velocity profile are known, whether from simulations, theory, or experiment, the model can be used to predict the segregation.

From previous studies [94, 95, 10], the streamwise velocity in the flowing layer can be approximated as

$$u(z) = Uf(z), \tag{2.18}$$

where $f(z)$ characterizes the depth dependence with $f(\delta) = 1$ so that $u(\delta) = U$, and U is determined by q and $f(z)$ as

$$U = \frac{q}{\int_0^\delta f(z)dz}. \tag{2.19}$$

The segregation model used here allows any functional form $f(z)$ to characterize the velocity profile, so that later in this chapter we can consider how the segregation pattern depends on the form of the velocity profile. To obtain the velocity field to compare the model results to DEM simulations, a bin averaging method was used to characterize streamwise velocity profiles at different streamwise locations as shown in figure 2.3 (a). A

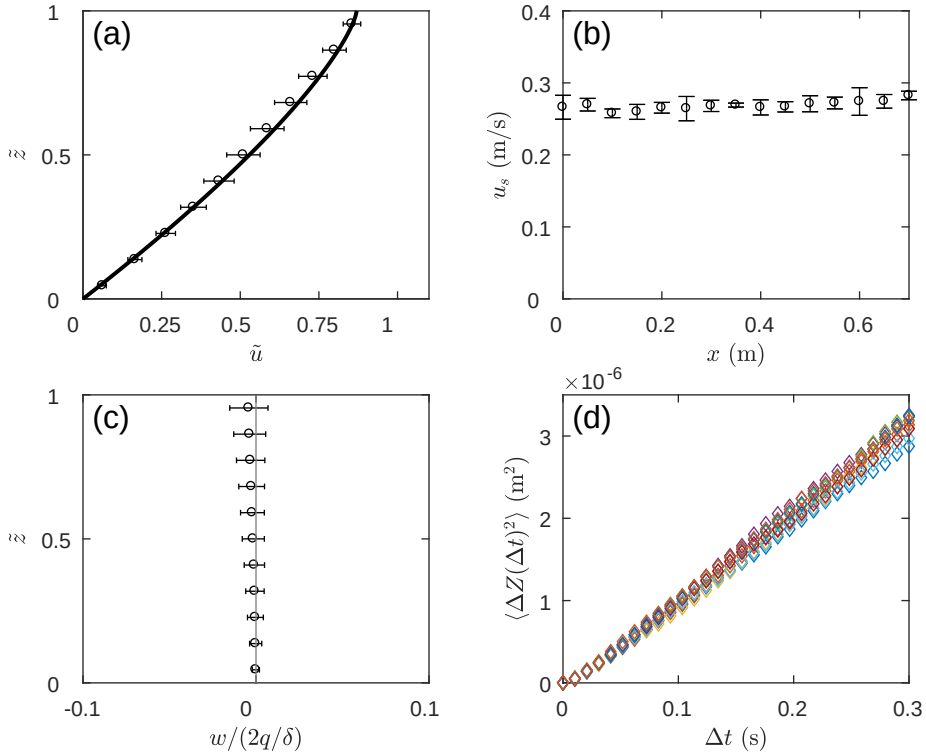

Figure 2.3. Kinematics of a particle mixture ($\alpha_i = 2, 3.2$ and 5 mm) at $q = 3400$ mm^2 s^{-1} from DEM simulations. (a) Averaged streamwise velocity profile vs. depth at different streamwise locations. Black curve is a least squares fit of the data to a "relaxed" Bagnold velocity profile, see equation 2.20. (b) Surface velocity u_s is nearly independent of streamwise position. (c) Scaled average normal direction velocity $w/(2q/\delta)$ is approximately zero through the depth of the flowing layer at different streamwise locations. (d) Normal direction mean squared displacement, $\langle \Delta Z(\Delta t)^2 \rangle$, over the entire flow domain vs. time for nine different time intervals (colors) (see text). Error bars in (a-c) indicate one standard deviation.

"relaxed Bagnold" expression $f(z) = 1 - (1 - z/\delta)^\beta$ [10] provides a reasonable approximation to the velocity profile. This expression becomes the classic Bagnold velocity profile when $\beta = 1.5$. Combining equations 2.8, 2.18, and 2.19, the dimensionless expression for

the mean velocity field is:

$$\tilde{u}(\tilde{z}) = \frac{u(z/\delta)}{2q/\delta} = \frac{\beta+1}{2\beta}\left[1-(1-\tilde{z})^{\beta}\right]. \tag{2.20}$$

Fitting data from the DEM simulation to this equation gives $\beta = 1.37$, which is similar to other numerical simulations [94, 95]. Hence, this value is used for the velocity profile in the continuum model for comparison to DEM simulations, in Section 2.4.1. The streamwise velocity profiles and free surface velocities are nearly constant along the entire length of the flow domain, as shown in Figure 2.3 (a) and (b), supporting the assumption that the velocity field is fully developed. The scaled normal velocity in figure 2.3 (c) is approximately 100 times smaller than the characteristic streamwise free surface velocity. Within the flow domain, advection dominates in the streamwise direction, so we assume that diffusion is important only in the normal direction. To obtain the diffusion coefficient, the mean squared displacement normal to the free surface for the entire flow domain, $\langle \Delta Z(\Delta t)^2 \rangle$, was measured over nine time intervals, each with a duration of $\Delta t = 0.3$ s. The details concerning how the diffusion coefficient is obtained from $\langle \Delta Z(\Delta t)^2 \rangle$ are included in Appendix C. Assuming diffusion to be homogeneous and isotropic within the entire flow domain as in earlier work [27, 91, 90, 112], the diffusion coefficient in the normal direction is approximated as $D = \langle \Delta Z(\Delta t)^2 \rangle / 2\Delta t$. The resulting diffusion coefficient is $D = 5.1$ mm^2 s^{-1}, consistent with the value $D = 6.22$ mm^2 s^{-1} calculated using a semi-empirical relation for the bidisperse quasi-2D bounded heap [89]. The difference between these two values of D is likely due to the different velocity fields for each flow, correspondingly different mean shear rates , and the fact that the value for D in this study is for tridisperse flow while the previous study considered bidisperse flow. Even though

there is 20% difference between D obtained from the two different methods, segregation is relatively insensitive to D, as will be shown later for different values of Pe.

2.4. Model predictions

2.4.1. Comparison with DEM simulations

To validate the continuum transport model for tridisperse segregation, we compare steady-state concentration fields predicted by equation 2.16 (using the velocity profile obtained from fitting the DEM data to equation 2.20 and $D = 5.1 \times 10^{-6}\,\mathrm{m^2 s^{-1}}$) with DEM simulation results at the same operating conditions (feed rate, flowing layer thickness, and inlet condition). In DEM simulations, the particles segregate slightly before leaving the vertical feed channel, so $c_s(0,\tilde{z}) \neq c_m(0,\tilde{z}) \neq c_l(0,\tilde{z}) \neq 1/3$. To account for this, the inlet concentration profile at the upstream end of the computational domain for the model was matched to the corresponding profile in the DEM simulation. Figure 2.4 compares results from the model and DEM simulation for an equal volume concentration mixture of 2, 3.2, and 5 mm diameter particles (for which we use the shorthand for the ratios $R = 1 : 1.6 : 2.5$) at $q = 3400$ mm^2/s and $\theta = 26.5\,^\circ$, which results in $\delta = 22\,\mathrm{mm}$ in the DEM simulation. In the model, the values of the four dimensionless parameters $\kappa_{l,s}$, $\kappa_{l,m}$, $\kappa_{m,s}$, and Pe were calculated based on the imposed feed rate (q), δ and D from DEM simulations, and the semi-empirical expression for the segregation length scale (S) for bidisperse spherical glass particles obtained from DEM simulations of bounded heap flow [89].

The volume concentration contours of the three different species for both the DEM simulation and the model are shown in figure 2.4 (a,b). Each image represents the flow

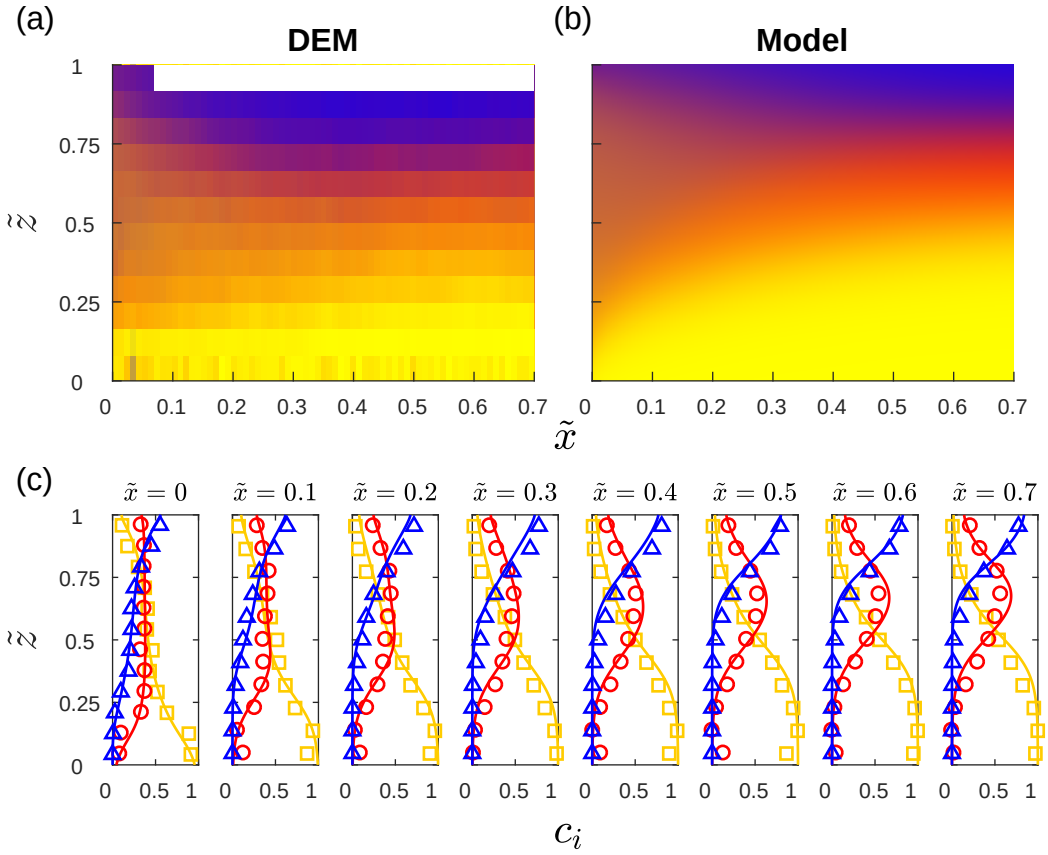

Figure 2.4. Comparison of concentration from DEM simulation and continuum model for tridisperse chute flow. (a) Particle concentration from DEM simulation. (b) Particle concentration from model. (c) Particle concentration profiles from simulation (markers) and model (curves) at different streamwise positions, x/L, from 0 to 0.7, where red, yellow, and blue represent the concentration of small, medium, and large particles, respectively. $S_{l,s} = 0.48\,\mathrm{mm}$, $S_{l,m} = 0.37\,\mathrm{mm}$, $S_{m,s} = 0.24\,\mathrm{mm}$, $D = 5.1\,\mathrm{mm}^2/\mathrm{s}$, $\delta = 22\,\mathrm{mm}$, $q = 3400\,\mathrm{mm}^2/s$, $\theta = 26.5\,^\circ$, $\kappa_{l,s} = 1.0$, $\kappa_{l,m} = 0.78$, $\kappa_{m,s} = 0.52$, $Pe = 29$.

domain extending from the free surface at the top of the image to the bottom of the chute and from the domain inlet on the left to $0.7L$ on the right, where the segregation is nearly fully developed. The DEM simulation results exhibit a slight decrease in the flowing layer thickness with downstream position, reflected as a step change in the upper surface of

figure 2.4 (a), which is not included in the model. Blue, red and yellow represent pure concentrations of large, medium, and small particles, respectively. Where species mix, the corresponding color is also mixed based on the concentrations of each species. Thus, an equal mixture of large (blue) and medium (red) particle species is represented by purple; an equal mixture of medium (red) and small (yellow) particle species is represented by orange; and an equal mixture of all three species is represented by brown. Figure 2.4 (a) demonstrates tridisperse segregation similar to the qualitative prediction by [36] using their multi-component particle size segregation model (Figure 15 and Figure 16 [36]). It is evident that segregation occurs in the direction normal to the free surface of the flowing layer. Large particles segregate toward the free surface and form a layer of segregated large particles at the top of the flowing layer (blue region). Small particles percolate downward to the bottom of the flowing layer and form a layer of segregated small particles just above the bottom surface of the chute (yellow region). Medium particles segregate upward from small particle rich regions and percolate downward from large particle rich regions to form a middle layer of segregated medium particles (red region). Because the flux of any species i, $\int_0^\delta u(x,z)c_i \; dz$, is conserved at any streamwise position x, the upper layer of large particles is thinner than the lower layer of small particles due to the higher velocity near the surface. Figure 2.4 (b) demonstrates how the model accurately predicts the tridisperse segregation pattern, similar to the general pattern from the approach used by [36], but with physical parameters that are easily connected to actual flow conditions. The reason behind the close match between DEM results and the model is two-fold. First, as the tridisperse system starts to segregate, two bidisperse systems form locally: a large and medium bidisperse flow in the upper portion of the flow and a medium and

small bidisperse flow in the bottom portion of the flow. Second, it has been shown that segregation is not strongly affected by the shear rate dependence of the diffusion coefficient [27]. Thus, a constant diffusion coefficient is sufficient to generate quantitative agreement between model and DEM simulations.

Compared with previous work [36], the physical parameters (S_{ij} and D) needed for the model are reduced. In [36], the segregation parameters equivalent to those used in our approach ($S_{\nu\mu}$ in their work) were not specified. In fact, the number of segregation parameters needed, N_n, grows quadratically for a mixture of n components ($N_n = \frac{1}{2}n(n-1)$). While it is possible to apply the model proposed by [41] and [36] to a bidisperse case ($N_n = 1$) by manually fitting model parameters to experimental results as done by [110], this only achieves qualitative comparison with the bidisperse case. This is further complicated by the increased number of parameters for three or more components, which makes the model proposed by [36] even more challenging to apply.

The segregation predicted using the model matches DEM simulation results not only at the end of the simulated region, where the three components of the mixture are nearly fully segregated though there is ongoing remixing between species because of collisional diffusion, but also at different streamwise positions where segregation is still developing. This agreement is remarkable considering the simplifying assumptions incorporated in the model. First, the model uses a single velocity profile that is assumed constant at all streamwise positions, independent of the concentration. Second, the model uses a single averaged diffusion coefficient even though the diffusion coefficient depends on local particle size and shear rate [89, 28]. Finally, the model uses a segregation coefficient derived from an entirely different flow geometry (bounded heap flow) for bidisperse (not

tridisperse) segregation. Nevertheless, concentration profiles from the model still match well with the DEM simulation at different streamwise positions, as shown in figure 2.4 (c), demonstrating not only the accuracy of the model but also its robust character. Note that the DEM data is plotted in figure 2.4 (c) such that the free surface data is always at $\tilde{z} = 1$ to account for the small decrease in surface height in the flow direction. Since the dimensionless parameters Pe, κ_{ij}, and characteristic segregation length scale L depend on physical control parameters, we further validate the predictions of the model by comparing with DEM simulations over a wider range of flow operating conditions in the Appendix D.

2.4.2. Influence of α_i, Pe, and $\kappa_{i,j}$ on segregation

Having validated the continuum model against DEM simulation, we now use the model to systematically investigate the effects of α_i and Pe on segregation for a well-mixed inlet. We first illustrate the effect of α_m on segregation for fixed α_s and α_l at different Pe, but a similar analysis can be performed for any of the species. We use a no-slip linear velocity profile because of its simplicity and ability to accurately approximate the velocity field for flow depths < 20 particles diameters thick [94, 76]. Figure 2.5 depicts an array of concentration contour maps, as in figure 2.4 (b), each corresponding to the flowing region for $0 \leq \tilde{x} \leq 1$ and $0 \leq \tilde{z} \leq 1$ over a wide range of Pe and α_m. Here we set $\alpha_s = 1$ mm and $\alpha_l = 3$ mm to investigate the effects of α_m and Pe. $\kappa_{i,j}$ are calculated based on the corresponding set of particle diameters. At high Pe, segregation dominates resulting in segregated layers, while at low Pe, diffusion dominates resulting in mixed particles (brown in the concentration contour maps). In the high Pe regime, the borders between different

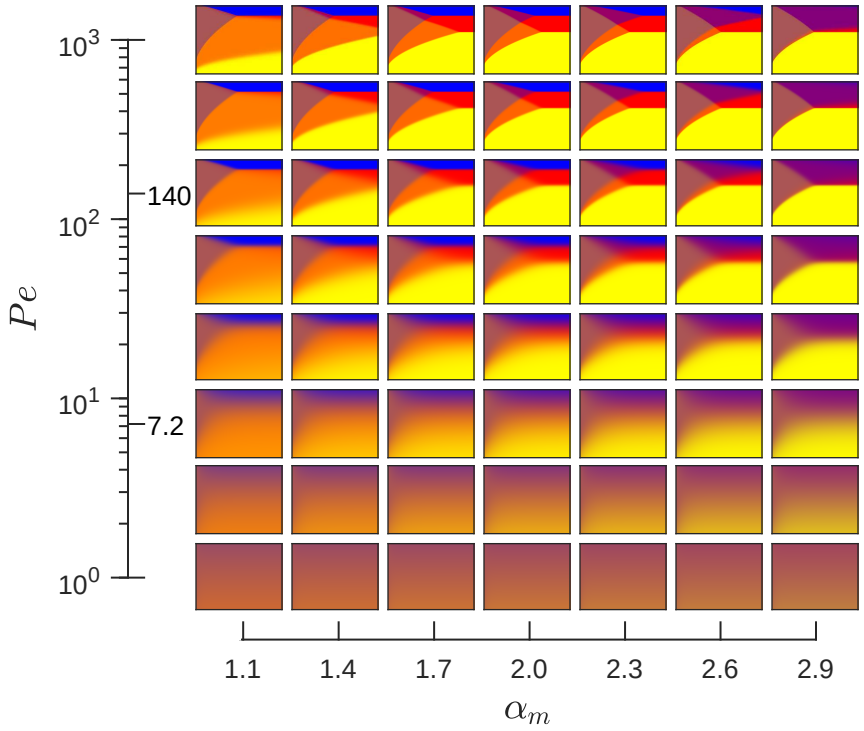

Figure 2.5. Tridisperse particle concentration contours in the flowing layer from the continuum model for different α_m and Pe for a well-mixed inlet condition with a no-slip linear velocity profile ($u = u_{\text{surf}}\tilde{z}$), $\alpha_s = 1$ mm, and $\alpha_l = 3$ mm. Each small box shows the entire flowing layer domain ($0 \leq \tilde{x} \leq 1$, $0 \leq \tilde{z} \leq 1$). Colour are as in figure 2.4.

species are relatively sharp for 1.4 mm $\leq \alpha_m \leq$ 2.6 mm, indicating a distinct transition from one pure species to another. However, the smaller difference in particle size for small α_m at high Pe in the upper left of figure 2.5 results in reduced segregation of the small and medium particles (orange region). For $Pe < 100$, the small size difference between medium and small particles ($\alpha_s = 1$ mm and $\alpha_m = 1.4$ mm) along with strong diffusion results in no fully segregated layers of small and medium particles at one characteristic length scale downstream. As Pe increases, even a small size difference produces segregated layers of small and medium particles. The model predictions for the tridisperse case collapse to the

bidisperse case when α_m is close to either its lower bound, α_s (left column) or its upper bound, α_l (right column). When $\alpha_l \gg \alpha_m \approx \alpha_s$ (left column), large particles quickly separate from medium and small particles, which remain in a mostly mixed state (orange region) unless the diffusion is minimal so that segregation dominates (high Pe). When $\alpha_s \ll \alpha_m \approx \alpha_l$ (right column), small particles quickly separate from medium and large particles, which remain mostly mixed (purple region) unless segregation dominates (high Pe). An interesting observation is that in the high Pe region, the segregation between small and medium particles is stronger when α_m approaches α_s (upper left corner) than the segregation between medium and large particles when the size of the medium particles approach the size of the large particles (upper right corner). There are two reasons for this phenomenon. First, the segregation length scale, S, in the empirical expression in equation 2.4 depends logarithmically on size ratio, and the size ratio is larger when the medium particle size approaches the small particle size than when the medium particle size approaches the large particle size. Second, the flow is slower in the lower portion of the flowing layer giving small and medium particles more time to segregate. Note that Pe measured from the DEM results presented in previous sections are generally less than 100. However, this does not imply that Pe is restricted to be less than 100 for all operating conditions. Considerable insight can be gained from the high Pe region ($Pe \approx 10^3$) in figure 2.5 where the impact of the size ratio R is clearer.

In addition to the effects of α_i and Pe on segregation, the model can also reveal the effects of $\kappa_{i,j}$ on segregation where $\kappa_{i,j}$ is the relative segregation strength between particle species i and j. Because $\kappa_{l,s} = 1$ by definition, the remaining parameters are $\kappa_{l,m}$ and $\kappa_{m,s}$. While similar analysis can be done for systems with more than three

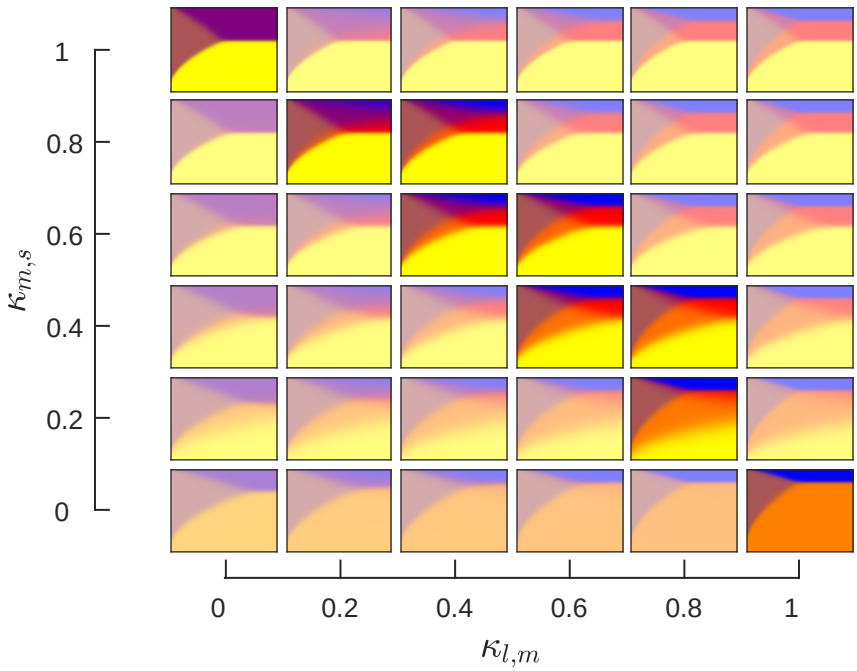

Figure 2.6. Tridisperse particle concentration contours in the flowing layer for different $\kappa_{l,m}$ and $\kappa_{m,s}$ for the well-mixed inlet condition with a no-slip linear velocity profile and $Pe = 100$. Each small box represents the entire flowing layer domain ($0 \leq \tilde{x} \leq 1$, $0 \leq \tilde{z} \leq 1$). The unshaded boxes represents the physically accessible region for spherical glass particles with $1/3 \leq \alpha_i/\alpha_j \leq 3$ and 1 mm $\leq \alpha_i \leq 3$ mm. Colour are as in figure 2.4.

particle species, tridisperse flow provides an intermediate step between bidisperse and polydisperse while allowing easy data visualization for aiding physical insight. Figure 2.6 shows an array of concentration contour maps for a well-mixed inlet condition over a range of $\kappa_{l,m}$ and $\kappa_{m,s}$, again assuming a no-slip linear velocity profile. The magnitude of $\kappa_{l,m}$ controls the segregation between large and medium species. As $\kappa_{l,m}$ increases at fixed $\kappa_{m,s}$ (rows), the segregation between the large and medium species increases. On the other hand, the magnitude of $\kappa_{m,s}$ controls the segregation between medium and small species. As $\kappa_{m,s}$ increases at fixed $\kappa_{l,m}$ (columns), the segregation between medium and small species increases. Restrictions imposed by particle size ($\alpha_s < \alpha_m < \alpha_l$) and the

empirical expression for S (equation 2.4) limit the physically accessible range of $\kappa_{l,m}$ and $\kappa_{m,s}$ for 1 to 3 mm glass spheres to the unshaded region in the figure 2.6. This is because the size of the medium particle bounds $S_{m,s}$ relative to $S_{m,l}$. To explain, when $\kappa_{m,s}$ is near 1, α_m must be close to α_l so that $S_{m,s} \approx S_{l,s}$. But when this is the case, $\kappa_{l,m}$ is necessarily small. Likewise, when $\kappa_{l,m}$ is near 1, α_m must be close to α_s so $\kappa_{m,s}$ is necessarily small. Consequently, only the two extreme cases located at the upper left and lower right corners in figure 2.6 are possible for $\kappa_{m,s} = 1$ and $\kappa_{l,m} = 1$, respectively. When $\kappa_{l,m} = 0$ and $\kappa_{m,s} = 1$ (upper left), the model collapses back to the bidisperse case because the large and medium species are the same size. The physical context corresponding to this scenario is medium and large particles so similar in size that they are inseparable, while small particles segregate from medium and large particles. A similar situation occurs when $\kappa_{l,m} = 1$ and $\kappa_{m,s} = 0$ (lower right). In this case, the medium and small species are the same size and do not segregate.

Since $\kappa_{i,j}$ is defined as the ratio of $S_{i,j}$ to $S_{l,s}$, which may depend not only on size ratio, but also on other particle properties such as density ratio, shape difference, surface roughness, and so on, the empirical expression for the segregation length scale (equation 2.4) may be different. Consequently, the value and functional dependence of $S_{i,j}$ could be different and, along with it, the $\kappa_{i,j}$ space. For example, based on equation 2.4, there is a small region where $S_{l,m}$ is slightly larger than $S_{l,s}$ because of the dependence of S on the actual particle size. This results in a small region where $\kappa_{l,m}$ is slightly greater than 1 (not shown in figure 2.6). Relationships for S other than the logarithmic expression in equation 2.4 result in a different physically accessible space than that shown in figure 2.6.

2.5. Interplay of advection, segregation, and diffusion

The dimensionless governing equation (2.13) indicates that the dimensionless parameters $\kappa_{i,j}$ and Pe control the concentration field through the interplay of segregation and diffusion in segregating chute flow. However, advection also plays a role via the streamwise segregation length, L. This is readily apparent when one considers the time scales for segregation, $t_s = \delta/w_p$, diffusion, $t_d = \delta^2/D$, and advection, $t_a = l/u_{\text{surf}}$, where l is the streamwise length of the domain. Segregation dominates advection within the domain when $t_s < t_a$, which after some simple manipulation can be shown to be equivalent to $L < l$. By considering the analytical solution of equation 2.14 in the absence of advection and segregation, the dimensionless form of the diffusion time scale, $\tilde{t}_d$, can be estimated as $\tilde{t}_d = Pe/\pi^2 \approx Pe/10$. The competition between different time scales is evident in figure 2.5. If the flow domain is at least L long ($\tilde{x} \geq 1$), then particles remained mixed when diffusion dominates (small Pe) and segregate when diffusion is weak (large Pe). If $l \ll L$ ($\tilde{x} \ll 1$ in figure 2.5), then the strong advection preserves the inlet condition to a significant extent.

To better understand the competition between different time scales, it is helpful to consider an "inverted" segregated inlet condition, where small particles are initially at the top, medium particles at the center, and large particles at the bottom of the flowing layer, such that

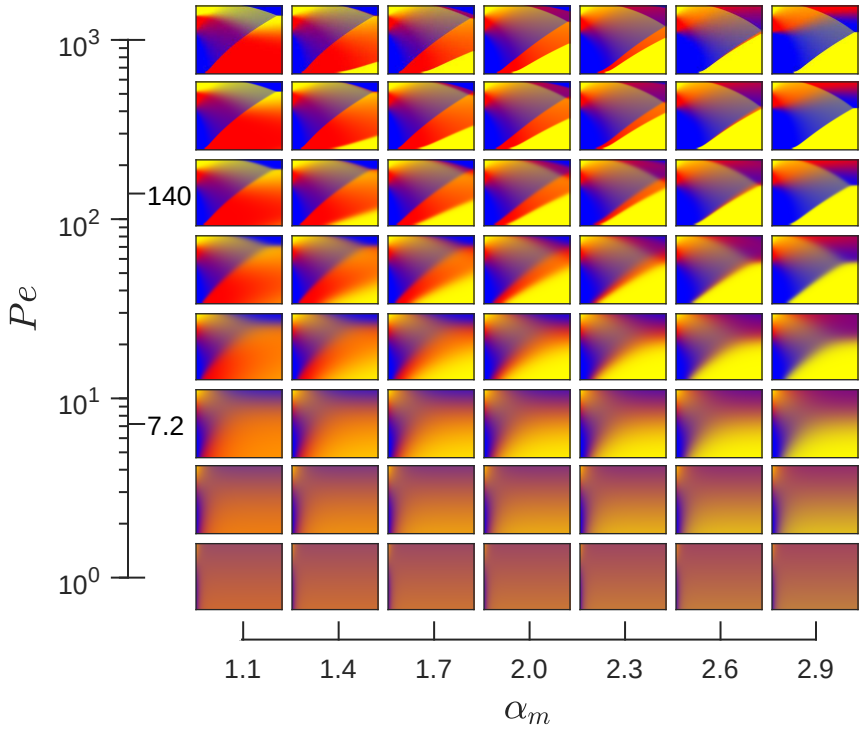

Figure 2.7. Tridisperse particle concentration contours for the "inverted" inlet condition for different α_m and Pe with a no-slip linear velocity profile, $\alpha_s = 1$ mm, and $\alpha_l = 3$ mm. Each small box shows the entire computational domain ($0 \leq \tilde{x} \leq 1$ and $0 \leq \tilde{z} \leq 1$). Colour are as in figure 2.4.

$$c_s(0,\tilde{z}) = \begin{cases} 1 & 0.817 \leq \tilde{z} \leq 1, \\ 0 & \tilde{z} < 0.817, \end{cases}$$

$$c_m(0,\tilde{z}) = \begin{cases} 1 & 0.577 \leq \tilde{z} \leq 0.817, \\ 0 & \tilde{z} < 0.577, \end{cases} \tag{2.21}$$

$$c_l(0,\tilde{z}) = \begin{cases} 1 & \tilde{z} \leq 0.577, \\ 0 & 0.577 < \tilde{z} \leq 1. \end{cases}$$

With this inlet concentration boundary condition and a no-slip linear velocity profile, the fluxes of small, medium and large particles entering the chute at $\tilde{x} = 0$ are approximately equal. Figure 2.7 shows an array of $Pe - \alpha_m$ contour maps (similar to figure 2.5) for an "inverted" inlet condition with a no-slip linear velocity profile. Consistent with physical insight gained from figure 2.5 for a mixed inlet condition, a strongly segregated state occurs at high Pe, and a well-mixed state occurs at low Pe. As Pe is increased, the situation is more complicated than for the mixed inlet. At high Pe and low α_m (upper left), segregation between medium and small particles is smaller than between medium and large particles. Consequently, medium particles stay below the small particles but large particles quickly rise through the layers of medium and small particles to the top of the flowing layer. As α_m approaches α_l (upper right), segregation between medium and small particles is stronger than between medium and large particles. In this case, medium particles stay above the large particles but the small particles quickly percolate through the medium and large particle layers to the bottom of the flowing layer. Thus, varying α_m changes the trajectory of the medium particle species to downward at small α_m and to upward at large α_m. At moderate values of α_m, medium particles that are initially close to large particles, first sink together with the small particles to the bottom of the flowing layer and then move upward away from the small particles. In contrast, medium particles that are initially close to small particles, first rise together with large particles and then later percolate downward to form a layer rich in medium particles below the large particle layer and above the small particle layer. Of course, if advection is significantly faster than segregation, corresponding to small $\tilde{x}$ (or $l \ll L$), then the inlet condition is preserved.

2.6. Influence of the velocity profile on segregation

Previous studies have demonstrated that segregation patterns in granular flow depend on the depthwise variation of the streamwise velocity [27]. Using an information entropy approach, Savage and Lun [86] predicted the dependence of the segregation velocity on the local shear rate $\dot{\gamma}$ leading, in part, to the percolation model in equation 2.3 where the local percolation velocity depends on the velocity profile through the local shear rate. For a no-slip linear velocity profile, which has been assumed to this point, the local shear rate is constant and the segregation velocity only depends on the local concentration. For a non-linear velocity profile (e.g., Bagnold or exponential), the local shear rate is a function of depth. As a result, the segregation velocity varies with depth even if the local particle concentrations are the same. This can significantly change particle distributions. In this section, we consider several different velocity profiles to demonstrate the dependence of the concentration field on the velocity profile.

To explore the effects of the velocity profile on segregation, we consider no-slip linear, Bagnold ($\beta = 1.5$ in equation 2.20), and exponential velocity profiles with the same flow rate q for a mixed inlet condition with equal volumes of small, medium and large particles. Combining equations 2.8, 2.18, and 2.19 with $f(z) = e^{kz/\delta}$, a dimensionless expression for the exponential velocity profile is given by

$$\tilde{u}(\tilde{z}) = \frac{k}{2(e^k - 1)} e^{k\tilde{z}}, \tag{2.22}$$

where k determines the slip velocity at the wall. When $k = 3$, the slip at the wall is 5% of the surface velocity.

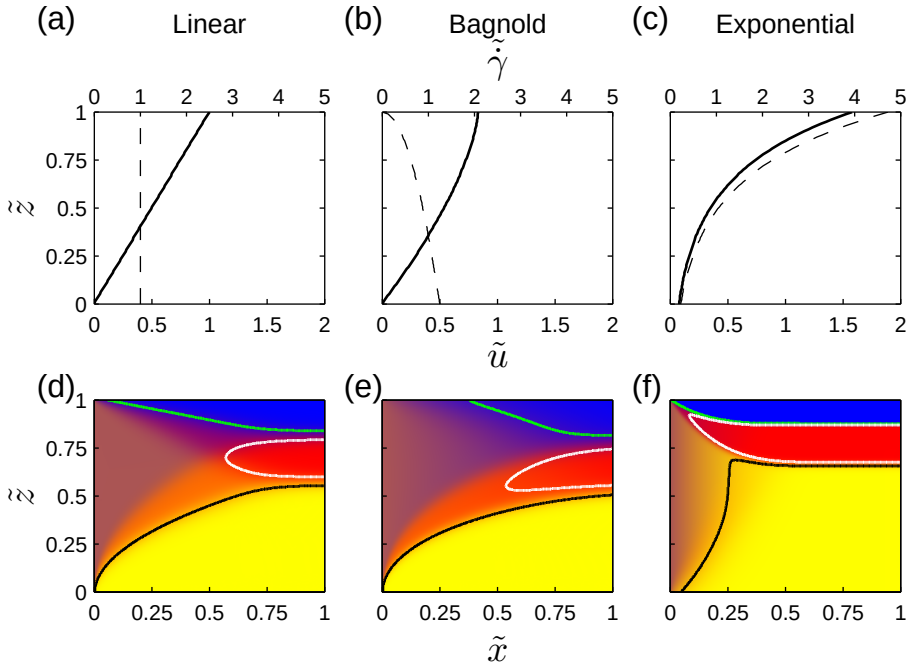

Figure 2.8. Comparision of tridisperse particle concentration fields for no-slip linear (left), Bagnold (middle), and exponential (right) velocity profiles (solid curves). For (a-c), solid curves represent the dimensionless streamwise velocity (bottom axis) and dashed curves represent the dimensionless shear rate magnitude (top axis). For (d-f), solid curves indicate the $c_i = 0.75$ contour for each species. $Pe = 100$ and $\kappa_{l,s} = 1.0, \kappa_{m,s} = 0.63, \kappa_{l,m} = 0.74$, which correspond to $\alpha_s = 1\,\text{mm}, \alpha_m = 2\,\text{mm}$ and $\alpha_l = 3\,\text{mm}$, respectively.

The dimensionless velocity profiles $\tilde{u}(\tilde{z})$ and the corresponding dimensionless local shear rates $\dot{\gamma}$ are shown in figure 2.8 (a-c) for the three velocity profiles. The corresponding segregation patterns for identical Pe and $\kappa_{i,j}$ are shown in figure 2.8 (d-f). Near the free surface of the flow, the exponential velocity profile produces the strongest and fastest segregation of medium and large particles compared to the other profiles, while the Bagnold profile results in the weakest and slowest segregation. This is because the exponential profile has the largest shear rate in the upper part of the flow, while the Bagnold profile has the smallest shear rate. Near the bottom of the chute, the Bagnold and

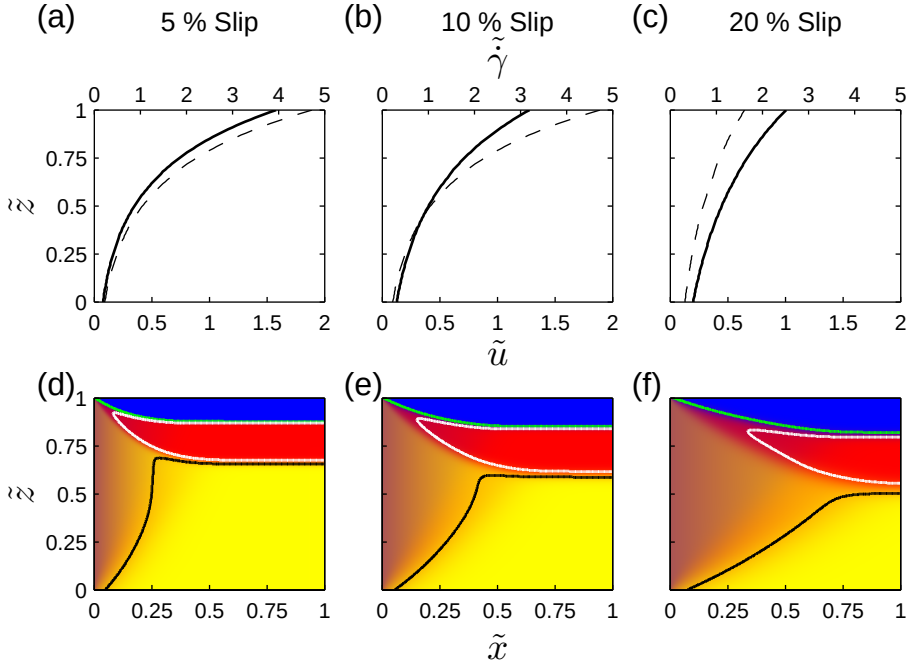

Figure 2.9. Effect of bottom boundary slip condition on tridisperse particle concentration in chute flow for exponential velocity profiles with 5%, 10% and 20% slip. For (a-c), solid curves represent the dimensionless streamwise velocity (bottom axis) and dashed curves represent the dimensionless shear rate magnitude (top axis). For (d-f), solid curves indicate the $c_i = 0.75$ contour for each species. $Pe = 100, \kappa_{l,s} = 1.0, \kappa_{m,s} = 0.63, \kappa_{l,m} = 0.74$, which correspond to $\alpha_s = 1\,\text{mm}, \alpha_m = 2\,\text{mm}$ and $\alpha_l = 3\,\text{mm}$, respectively.

no-slip linear velocity profiles have faster initial segregation than the exponential velocity profile because of their relatively large shear rates near the bottom of the flowing layer. Moving upward in the flowing layer the shear rate for the exponential velocity profile becomes large compared to the no-slip linear or Bagnold profiles leading to stronger overall segregation and a thicker layer of segregated small particles further downstream.

The roughness of the bottom wall of the chute also affects the velocity profile. With a rough bottom wall, the basal velocity ($\tilde{u}(0)$) is approximately zero [3, 83, 95]. However, with a smooth bottom wall, slip is possible at the bottom wall [108, 94, 67], which can

be expressed as a percentage of the free surface velocity. Recent work suggests that slip or nonslip boundary conditions can be predicted by their proposed base roughness parameter which is a function of basal particle size ratio and basal particle construction [52, 54]. Figure 2.9 demonstrates how slip affects particle segregation in the flowing layer for an exponential velocity profile with constant streamwise flux. As noted above, $k = 3$ provides a slip of 5%; when $k = 2.3$, the slip is 10%; and when $k = 1.61$, the slip is 20%. The velocity profiles for these three values of k are plotted in figure 2.9 (a-c) along with the corresponding local shear rate profiles which vary substantially with the degree of slip, particularly the magnitude of the local shear rate near the top of the flowing layer. The corresponding solutions of the continuum model are shown in figure 2.9 (d-f). Because the 5% slip profile has the largest average $\dot{\gamma}$ throughout the flowing layer, the overall degree of segregation is the strongest as shown by the rapid flattening of the concentration contours. The 20% slip case has the smallest average $\dot{\gamma}$ throughout the flowing layer, and, consequently, the overall degree of segregation is so weak that the concentration profile is still developing at the end of one characteristic length. The segregation of the small particles is particularly slow in this case because of the low shear for $0 \leq \tilde{z} \leq 0.5$. From a practical standpoint, segregation in a chute can be reduced by a large slip velocity.

2.7. Conclusion

Tridisperse flow provides an important connection between bidisperse and polydisperse flow because it tests the pair-wise interaction hypothesis of the percolation model and provides more straightforward physical insight than is possible with polydisperse systems. This chapter use a continuum transport model to explore segregation of tridisperse

granular material in a gravity driven flow. The approach accurately models tridisperse chute flow as indicated by the close agreement between its predictions and results from DEM simulation over a wide range of flow conditions including different incline angles, particle size distributions, flow rates, and flowing layer thicknesses. The model is based on an understanding of the kinematics of granular flow and has no arbitrarily adjustable fitting parameters, though the dependence of the segregation length scale on the size ratio must be known for bidisperse mixtures. Particle segregation depends on $Pe = 2qS_{l,s}/(\delta D)$, which is the ratio of the segregation rate to the diffusion rate, $\kappa_{i,j} = S_{i,j}/S_{l,s}$, which is the relative segregation strength between particle species i and j, and $L = \delta^2/S_{l,s}$, which is a characteristic length scale based on the segregation between the smallest and largest particle.

The advantage of this model is that it allows exploration of the effects of relative particle size, diffusion and the velocity profile on the segregation characteristics. Unlike cases where particles flow in a thin layer down a surface of other particles at a natural dynamic angle of repose, chute flow is affected by the roughness of the surface on which the particles flow and the angle of the surface. These effects can be included in the model via the velocity profile, provided it can be determined from experiments, simulations, or theory. An important aspect of chute flow is that the flowing layer thickness or velocity profile may change with streamwise position. While this complicates the analysis, it is possible to model these effects provided the streamwise variation in the velocity profile and flowing layer thickness are known, again from experiments, simulations, or theory. Also, the velocity profile appears to couple only weakly to the degree of segregation for

the cases we have studied, which is also the case for the other free surface granular flows we have studied [27, 112].

While we have demonstrated the effectiveness of the tridisperse modeling framework for spherical particles segregating by size, it is likely that it can be readily adapted to other types of particle dispersity (e.g., particle density or shape), provided that relations for the dependence of the segregation velocity and the diffusion on the kinematics and concentration can be determined either through experiment or DEM simulation. The framework also captures how different velocity profiles and the degree of slip affect the segregation pattern in a chute flow. However, challenges remain. For example, we have not considered the coupling between the segregation and rheology or velocity feedback from the segregation, which is likely to be important when size ratios are large or the degree of segregation is high. These mechanisms can potentially be incorporated into the formalism by deriving the velocity field from a momentum equation with a rheology model (for example $\mu(I)$ rheology [83, 84, 39, 23, 7]) dependent on the local particle concentration. Also, recent work indicates that for a small friction coefficient (≈ 0.1), the segregation mechanism can be different [53], which is a possibility not considered in this work. These extensions will further complement the current model and advance it toward becoming part of a general framework for modeling segregating particle flows.

CHAPTER 3

Modeling segregation of polydisperse granular materials in developing and transient free surface flows

Even though size segregation of polydisperse granular material is prevalent in many industries, a general segregation model to predict polydisperse segregation encountered in physical systems is still lacking. In this chapter, we extend the application of a general predictive continuum model that captures the effects of segregation, diffusion, and advection in two ways. First, we consider polydisperse segregating flow in developing steady segregation and developing unsteady segregation. In both cases, several terms in the model that were zero in the previously examined case of fully-developed streamwise-periodic steady segregation in a chute are now non-zero, which makes application of the model substantially more challenging. Second, we apply the polydisperse approach to density polydisperse materials with the same particle size. Predictions of the model agree quantitatively with experimentally validated discrete element method simulations of both size polydisperse and density polydisperse mixtures having uniform, triangular, and log-normal distributions.

The material in this chapter was published in a slightly different form in Deng, *et al.,* "Modeling segregation of polydisperse granular materials in developing and transient free surface flows" *AIChE J* (2019) [20] ©The American Institute of Chemical Engineers, reprinted with permission.

3.1. Introduction

Size segregation of polydisperse granular materials is common in many industrial processes and natural settings. Until recently, most theoretical approaches to modeling segregation in granular flows have focused on size bidisperse mixtures (two particle sizes). These approaches have been helpful in understanding the underlying physical mechanisms in segregating flows and in developing predictive frameworks for bidisperse segregating systems [21, 86, 22, 41, 42, 38, 100, 73, 110, 24, 99, 64, 104, 65]. Multidisperse and polydisperse granular segregation (i.e., involving three or more monodisperse species or a continuous distribution, respectively, of a particular particle property), though far less studied, are nevertheless frequently encountered in physical systems. These systems have been explored both in experiments [46, 80, 9, 16] and in simulations using the discrete element method (DEM) [72, 46, 82, 9] for various flow geometries. Multidisperse flow is easier to model analytically than polydisperse flow; for example, tridisperse segregation (three species) has been modeled in a chute [36, 19] and a bounded heap [91]. Polydisperse segregation is more difficult to handle analytically. Only a few studies have proposed models for polydisperse granular segregation, and these have been limited to the idealized case of streamwise-periodic chute flow in which periodic streamwise boundary conditions are used to model fully-developed segregation in a section of a chute [72, 71, 91].

The simple geometry of periodic chute flow makes it relatively straightforward to apply models for segregating polydisperse flows. For example, Marks et al. [72] developed a continuum model for polydisperse segregation in a periodic chute that relies on a fitting parameter determined from DEM simulations. Recently, the same group used a stochastic lattice model incorporating the effects of segregation, mixing, and crushing to predict

steady state particle size distributions in uniformly sheared granular flows in a periodic chute [71]. Although this approach connects micro- and macroscale advection-driven processes for polydisperse systems, its agreement with experimentally measured particle size distributions is only qualitative. Moreover, these models of polydisperse segregation include some adjustable parameters that are challenging to directly relate to physical quantities. This makes it difficult to extend the results to specific particle sizes, shapes, and densities or to generalize the model to a continuous distribution of particle sizes or to other flow geometries. Furthermore, previous models of polydisperse segregation [72, 71, 91] have focused on fully-developed segregation in a streamwise-periodic chute using DEM simulations. While the streamwise-periodic chute geometry is suitable for initial testing and validation of segregation models due to its simplicity, this geometry only produces segregation in the depthwise direction and corresponds to a pre-filled chute infinite in length or to the downstream region of the chute where material advected from the top of the chute has not reached.

In this chapter, we go well beyond previous studies by extending the application of a general predictive continuum model for bidisperse segregation to polydisperse segregating materials in the substantially more challenging (and realistic) situations of developing (spatially-dependent) segregation in a bounded heap and transient (time-dependent) segregation in a rotating tumbler. Both bounded heap flow and rotating tumbler flow differ in several key aspects from periodic chute flow. In periodic chute flow, shown in figure 3.1(a), the periodic boundary condition enforces that the flow and segregation are implicitly fully developed ($\frac{\partial}{\partial x} = 0$). Hence, periodic chute flow only captures depthwise

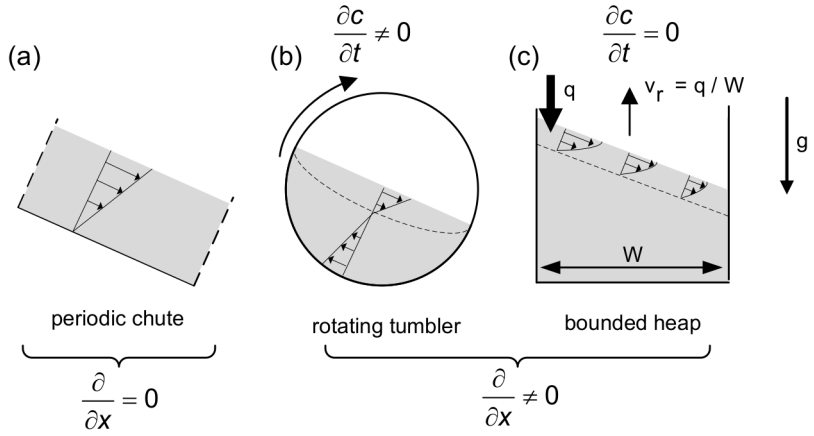

Figure 3.1. Canonical configurations of granular flow in a quasi-two-dimensional geometry of gap thickness T, where u is the velocity field, c is the concentration, x is the streamwise direction, $q = Q/T$ is the two-dimensional feed rate, Q is the bulk volumetric feed rate and g is the acceleration due to gravity. Dashed lines in (a) represent periodic boundary conditions.

evolution of the segregation. On the other hand, in rotating tumbler flow and gravity-driven bounded heap flow, the flow is developing ($\frac{\partial}{\partial x} \neq 0$). Consider first the bounded heap flow, shown in figure 3.1(c). Because the flow is stopped by a wall at the downstream end of the heap, the surface of the heap rises at a constant rise velocity v_r, and the streamwise velocity u in the thin flowing layer decreases with streamwise position, so $\frac{\partial u}{\partial x} \neq 0$. As bidisperse particles flow down the slope, the concentration of the particle species c varies with streamwise position, so $\frac{\partial c}{\partial x} \neq 0$. Small particles percolate to the bottom of the flowing layer and deposit onto the upstream portion of the static bed, while large particles deposit onto the downstream portion of the bed. Flow in rotating tumblers, shown in figure 3.1(b), is similar to bounded heap flow in that the streamwise velocity and particle concentration both vary with streamwise position ($\frac{\partial}{\partial x} \neq 0$) in the lens-shaped surface flowing layer [81, 11]. However, rotating tumbler flow differs from steady bounded heap

flow in that the segregation in rotating tumbler flow is transient ($\frac{\partial c}{\partial t} \neq 0$) during start up. For initially mixed bidisperse particles in circular rotating tumbler flow, small particles percolate to the bottom of the flowing layer and deposit near the center of the tumbler, while large particles remain in the flowing layer and deposit near the periphery of the tumbler. As a result, the concentration of particles in the flowing layer varies with time until the segregation reaches a steady state after 5-10 tumbler rotations. Consequently, both bounded heap flow and rotating tumbler flow have substantially more complicated flow kinematics than periodic chute flow.

Recently, we were able to successfully apply a relatively simple continuum segregation model for bidisperse granular mixtures to quasi-2D bounded heaps [27] and circular tumblers [90]. This particular approach utilizes segregation parameters and material-dependent scalings, typically obtained from DEM simulations, that are directly connected to the physics of segregation at the particle scale and consequently are independent of the flow geometry. As a result, the approach is applicable to a wide range of flow rates, particle size ratios, particle size distributions, flow geometries, and even density driven segregation [112]. This model has been applied to segregation in steady polydisperse streamwise-periodic chute flow, where it reduces to an easily solved one-dimensional equation (depthwise variation only) that does not include advection effects or transient effects [91]. The goal of this chapter is to further extend the application of this continuum modeling framework [27, 91, 90] to the segregation of polydisperse granular mixtures resulting from the interaction between advection, segregation, and diffusion in developing steady segregation and in developing transient segregation. Specifically, we apply the model to polydisperse particles in two different flow geometries: 1) Spatially-dependent segregation

in steady quasi-2D one-side bounded heap flow [figure 3.1(c)]; and 2) Transient segregation in a rotating circular tumbler flow upon start-up with an initially mixed state [figure 3.1(b)]. In addition to considering polydisperse size segregation, we demonstrate that a model similar to that for size polydisperse segregation works equally well for density polydisperse segregation, where particles have the same size, but a distribution of densities. The key result of this chapter is to provide an analytic framework for predicting the segregation of polydisperse material in a general flow field that can be developing and transient.

The remainder of the chapter is organized as follows. The transport equations for segregating polydisperse flow are initially developed. To validate the continuum model, the spatial distributions of particle diameters from polydisperse DEM simulations are compared with the model prediction for developing bounded heap flows and for transient rotating tumbler flows. After validating the model for size polydisperse segregation, we demonstrate that a similar formulation works equally well for density polydisperse segregation. Concluding remarks are provided in the end.

3.2. Model derivation

Bridgwater et al. [13] were apparently the first to propose a modified advection-diffusion equation with a segregation term to model segregating granular flows through a scalar transport equation. While many variations on this approach have been proposed [21, 22, 41, 42, 38, 36, 39, 27, 91], here we use the approach of Fan et al. [27] and Schlick et al. [91]:

$$\frac{\partial c_i}{\partial t} + \nabla \cdot (\mathbf{u} c_i) + \frac{\partial}{\partial z}\left(w_{p,i} c_i\right) = \nabla \cdot (D \nabla c_i), \tag{3.1}$$

where $\mathbf{u} = u\hat{\mathbf{x}} + v\hat{\mathbf{y}} + w\hat{\mathbf{z}}$ is the bulk particle velocity with streamwise ($\hat{x}$), spanwise ($\hat{y}$), and normal components ($\hat{z}$), u, v, and w, respectively; c_i is the volume concentration of species i; D is a diffusion coefficient that accounts for random particle collisions (remixing); and $w_{p,i} = w_i - w$, where $w_{p,i}$ is the normal component of the percolation velocity due to segregation of species i based on the normal velocity of species, w_i, relative to the mean normal flow velocity, w. This model has been applied successfully to bidisperse segregation in bounded heaps [27, 89] and rotating tumblers [90], tridisperse segregation in inclined chutes [19], tridisperse segregation in bounded heaps [91], and polydisperse segregation in fully developed steady streamwise-periodic chute flow [91]. In all cases, predictions of the model agree quantitatively with both validated DEM simulations and experiments.

The key to accurately describing bidisperse segregation is the semi-empirical relation for the component of the segregation velocity normal to the free surface, $w_{p,i}$, which is based on a linearization of Savage and Lun's kinetic sieve model [86, 55] for size bidisperse mixtures composed of particles with diameters α_i and α_j [91, 27]. The segregation velocity of species i depends on the local shear rate, $\dot{\gamma}$, and the concentration of the other species, c_j, as

$$w_{p,i} = S(\alpha_i, \alpha_j)\dot{\gamma} c_j, \tag{3.2}$$

where $S(\alpha_i, \alpha_j)$ is an empirically determined segregation length scale dependent on size ratio and particle diameters [89] as well as gravity and local pressure [31]. This equation differs from previous approaches used by Gray and Thornton [41], Kowalski and McElwaine [63], Kimberly and Fan [61] for bidisperse mixtures by virtue of the explicit

inclusion of the local shear rate. Additionally, equation 3.2 has a further advantage in that $S(\alpha_i, \alpha_j)$ can be specified in terms of particle sizes as shown below, whereas previous work [41, 63, 61, 98] provides no means to determine equivalent parameters. $S(\alpha_i, \alpha_j)$ can be expressed as a function of the particle size ratio:

$$S(\alpha_i, \alpha_j) = B \min(\alpha_i, \alpha_j) \ln(\alpha_i/\alpha_j), \tag{3.3}$$

where B is a dimensionless constant independent of particle size [89]. From one-sided bounded heap DEM simulations of mm-sized spherical glass particles with size ratios $1/3 \leq \alpha_i/\alpha_j \leq 3$, $B = 0.26$ [89], and we use this value for the rest of this chapter. For size ratios beyond this range, $S(\alpha_i, \alpha_j)$ could still be measured by performing bidisperse bounded heap DEM simulations similar to previous work [27, 89], even though the functional dependence on size ratio might be different. Equations 3.2 and 3.3 capture the downward percolation of small particles due to kinetic sieving and the upward movement of large particles due to squeeze expulsion in a flowing size bidisperse mixture [86]. Note that since S in equation 3.2 is directly measured from the segregation in DEM simulations of the flowing layer of a gravity-driven one-sided bounded heap flow, the effect of gravity is implicitly included in S, and, consequently, g does not explicitly appear in equation 3.2.

To model polydisperse segregation, we consider a continuous distribution of particles sizes with diameters $\alpha_{\min} \leq \alpha \leq \alpha_{\max}$. Schlick et al. [91] generalized equation 3.1 to polydisperse mixtures as

$$\frac{\partial c(\mathbf{x},t,\alpha)}{\partial t} + \nabla \cdot [\mathbf{u}c(\mathbf{x},t,\alpha)] + \frac{\partial}{\partial z}\int_{\alpha_{\min}}^{\alpha_{\max}} S(\alpha,\beta)\dot{\gamma}c(\mathbf{x},t,\alpha)c(\mathbf{x},t,\beta)d\beta = \nabla \cdot [D\nabla c(\mathbf{x},t,\alpha)], \tag{3.4}$$

where, unlike the bidisperse model (equation 3.1) in which c_i represents the concentration of particle species i, $c(\mathbf{x},t,\alpha)$ represents the probability density function for particles with diameter α at position $\mathbf{x}$ at time t for particle diameters extending from $\alpha_{\min}$ to $\alpha_{\max}$. The connection between equations 3.1 and 3.4 is achieved by noting that for the multidisperse case with a finite number of distinct particle sizes having diameter α_i and concentration $c_i (i = 1, ..., n)$, the probability density function is related to the concentration of individual species by

$$c(\mathbf{x},t,\alpha) = \sum_{i=1}^{n} c_i(\mathbf{x},t)\delta(\alpha - \alpha_i), \tag{3.5}$$

where $\delta(\alpha - \alpha_i)$ is the Dirac delta function. Equation 3.4 is obtained by substituting equation 3.5 along with equation 3.2 into equation 3.1 and replacing the summation by an integral. In addition, the expression for the percolation velocity for a particle of size α can be generalized from equation 3.2 as:

$$w_p(\alpha) = \int_{\alpha_{\min}}^{\alpha_{\max}} S(\alpha,\beta)\dot{\gamma}c(\mathbf{x},t,\beta)d\beta. \tag{3.6}$$

That is, the percolation velocity of a particle of size α is based on a linear combination of the segregation length scales $S(\alpha,\beta)$ and concentrations of the surrounding particles [91, 19]. While equation 3.4 can be applied to any arbitrary particle size distribution, here we nondimensionalize the particle size as $\tilde{\alpha} = \alpha/d_0$, where d_0 is a typical particle

Table 3.1. Particle size distributions considered in this study

Distribution	$c(\tilde{\alpha})$	Domain	First moment	Second moment
Log-normal $\sigma = 0.3$	$\frac{1}{\tilde{\alpha}\sigma\sqrt{2\pi}} \exp\left[-\frac{(\log\tilde{\alpha})^2}{2\sigma^2}\right]$	$\tilde{\alpha} > 0$	1.04	1.17
Uniform	$2/3$	$0.5 < \tilde{\alpha} < 2$	1.25	1.75
Triangular	$\begin{cases} \frac{16}{9}(\tilde{\alpha} - 0.5) & \text{if } 0.5 \leq \tilde{\alpha} \leq 1.25 \\ \frac{16}{9}(2 - \tilde{\alpha}) & \text{if } 1.25 \leq \tilde{\alpha} \leq 2 \end{cases}$	$0.5 < \tilde{\alpha} < 2$	1.25	1.66

diameter, and consider different probability density functions, $c(\tilde{\alpha})$, corresponding to log-normal, uniform, and triangular particle size distributions (table 3.1) with $d_0 = 2$mm for 1 mm $\leq \alpha \leq$ 4 mm for demonstration purposes. A similar analysis could be done using different d_0. The log-normal distribution is truncated between $\alpha_{\min}$ and $\alpha_{\max}$ to avoid the infinitely long tails of the distribution.

If equations 3.4 and 3.6 are applied to steady fully developed streamwise-periodic chute flow [figure 3.1(a)], equation 3.4 reduces to a much simpler one-dimensional equation [91], in which the first two terms of equation 3.4 drop out:

$$\frac{\partial}{\partial z}\int_{\alpha_{\min}}^{\alpha_{\max}} S(\alpha,\beta)\dot{\gamma}c(\mathbf{x},t,\alpha)c(\mathbf{x},t,\beta)d\beta - \nabla\cdot[D\nabla c(\mathbf{x},t,\alpha)] = 0. \tag{3.7}$$

However, for developing segregation in a one-sided bounded heap [figure 3.1(c)] and considered here, only the unsteady term ($\frac{\partial c}{\partial t}$) can be neglected, while for developing flow with unsteady segregation in a rotating tumbler [figure 3.1(b)], all terms in equation 3.4 must be included.

It is helpful to compare the approach here to previous studies. Marks et al. [72] proposed a polydisperse theory based on mass and momentum conservation, in which $w_p(\alpha)$ depends linearly on the shear rate to account for kinetic sieving [86], and also depends linearly on the component of gravity in the surface normal direction (z) to account for

gravity-driven segregation. The influence of the local particle concentration is characterized by the ratio $\alpha/\bar{\alpha}$, where $\bar{\alpha}$ is the local average particle size, which can vary in time and space. Their expression for the percolation velocity also includes a fit parameter to match the numerical solution of the model to specific DEM simulations, but its exact functional dependence on shear rate and particle size was not specified. Gray and Ancey [36] proposed a multicomponent expression for the percolation velocity of a mixture of n discrete particle sizes based on the bidisperse theory of Gray and Thornton [41] that could theoretically be generalized to a polydisperse mixture as n approaches infinity. However, because the number of segregation coefficients grows quadratically with n [36], this approach quickly becomes challenging to apply. The model uses a gravity-related term to account for the gravity-driven nature of the segregation, and the local particle concentration effect is handled in terms of the linear combination of the concentration of surrounding particles, as in equation 3.6. The approach also incorporates a non-dimensional parameter for the magnitude of the pressure perturbation on particle species i due to the presence of particle species j. However, it is not clear how this parameter for a finite number of particles sizes could be extended to the continuous range of particle sizes necessary for describing polydisperse segregation. Furthermore, Gray and Ancey [36] do not explicitly include any dependence on the local shear rate, which is inherent in the standard kinetic sieving model [86]. It is important to explicitly include the shear rate to account for the impact of the local velocity profile on the segregation [27, 19].

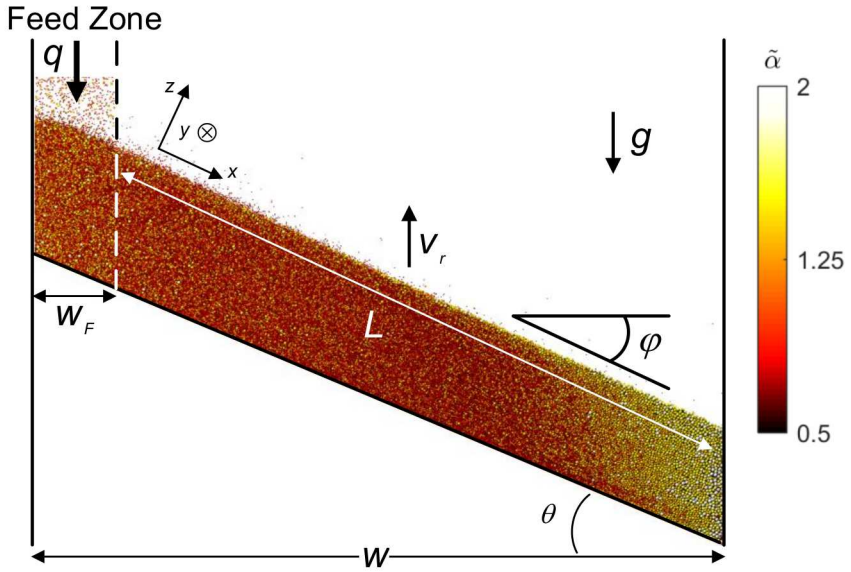

Figure 3.2. Quasi-2D one-sided bounded heap of width W and thickness T (in the transverse y direction) with bottom wall inclined by angle θ in DEM simulations. The length of the flowing layer from the right edge of the feed zone to the downstream bounding wall is L. The heap dynamic repose angle is φ. A log-normal distribution of polydisperse particles ranging from 1 mm (dark) to 4 mm (light) are used in the simulation shown.

3.3. Developing steady bounded heap segregation ($\frac{\partial}{\partial x} \neq 0, \frac{\partial c}{\partial t} = 0$)

To validate the polydisperse model (equation 3.4) for developing ($\frac{\partial}{\partial x} \neq 0$), steady ($\frac{\partial c}{\partial t} = 0$) flow, we compare the model results to DEM simulations of polydisperse segregation in the flowing layer of a quasi-two-dimensional (2D) one-sided bounded heap, which is the same flow geometry considered in previous studies of segregation in size bidisperse mixtures [27, 89] and tridisperse mixtures [91]. DEM simulations for size polydisperse spherical particles with a uniform, triangular, and log-normal distributions are considered. All the simulations are performed with DEMSLab [1], a commercial DEM simulation software package. Details of the DEM simulations are provided in Appendix A and in

previous chapters [118, 117]. In quasi-2D bounded heap flow, granular material is fed by gravity at bulk volumetric feed rate Q in a W_F wide feed zone on the left side of the W wide heap with gap thickness T between the front and back walls. The bottom wall is inclined at angle θ in order to save computation time associated with filling the apparatus to the point where the heap spans both end walls [27]. Due to the quasi-2D nature of the flow, the two-dimensional flow rate $q = Q/T$, where Q is the bulk volumetric flow rate, is used to characterize the feed rate.

Here, we focus on the steady filling stage of heap flows as identified in previous work [25]. At a sufficiently high feed rate, material flows continuously down the slope, and the heap surface rises with a uniform velocity $v_r = Q/TW$. If the coordinate system is placed at the top of the free surface and rises together with the heap surface at a uniform rise velocity v_r, the flow can be considered as a steady state flow problem [27, 89, 91]. Typical segregation patterns corresponding to an initially well-mixed polydisperse material are shown in figure 3.2. For these simulations, the width of the heap W is 0.69 m, the gap thickness T is 0.02 m, and the bottom wall is inclined at $\theta = 24°$. The flowing layer from the right edge of the feedzone to the bounding wall is inclined at the heap dynamic repose angle, φ, and has length $L = (W - W_F)/\cos(\varphi)$. The smallest particles quickly percolate to the bottom of the flowing layer and deposit on the upstream portion of the heap. The largest particles rise to the top of the flowing layer and are advected to the downstream portion of the heap to be deposited there. The intermediate size particles rise above the smallest particles but fall below the largest particles and deposit midway along the slope of the heap. As a result, the final distribution of particles deposited on the heap in figure 3.2 varies from mostly small particles upstream (on the left) to mostly large

particles downstream (on the right). A larger fraction of the heap is dark corresponding to small particles, because the log-normal size distribution has more small particles than large particles by volume. Note that some large particles are trapped in the feed zone, because they are immediately buried by other particles before having a chance to flow down the slope of the heap. Further note that some large particles are deposited on the upstream portion of the heap with the small particles. This comes about because the large particles entering the left end of the flowing layer are distributed across the thickness of the flowing layer. The large particles nearest the bottom of the flowing layer do not have adequate time to rise to the upper portion of the flowing layer and before they, instead, are deposited further upstream with the smaller particles. On the other hand, few small particles are deposited at the downstream end of the heap because the smallest particles, even those starting near the top of the flowing layer at the upstream end of the heap, have adequate time to segregate through the entire flowing layer to deposit further upstream, leaving only the larger particles at the downstream end of the heap.

To solve the continuum segregation model (equation 3.4) for bounded heaps, the flowing layer thickness, δ, which is defined as the depth where the streamwise velocity is one tenth the free surface velocity, is approximated as constant [26], which has been successfully assumed previously [27, 91, 89, 19]. The particle diameter is non-dimensionalized using $\tilde{\alpha} = \alpha/d_0$, where $d_0 = 2$ mm. Particle sizes are restricted to $0.5 < \tilde{\alpha} < 2$ (or, since $d_0 = 2$ mm, particle diameters are between 1 and 4 mm). Note that this size range slightly extrapolates the applicability of equation 3.3, but this has negligible impact on the results because pairs of particles with a large size ratio interact infrequently due to

their small numbers [91]. Additionally, equation 3.4 is non-dimensionalized using

$$\tilde{x} = \frac{x}{L},\ \tilde{z} = \frac{z}{\delta},\ \tilde{u} = \frac{u}{2q/\delta} \text{ and } \tilde{w} = \frac{w}{2q/L} \tag{3.8}$$

and becomes

$$\frac{\partial}{\partial\tilde{x}}(\tilde{u}c) + \frac{\partial}{\partial\tilde{z}}(\tilde{w}c) + \frac{\partial}{\partial\tilde{z}}\int_{\tilde{\alpha}_{\min}}^{\tilde{\alpha}_{\max}} S(\tilde{\alpha},\tilde{\beta})\tilde{\dot{\gamma}}c(\tilde{\alpha})c(\tilde{\beta})d\tilde{\beta} - DL/2q\delta^2\frac{\partial^2 c}{\partial\tilde{z}^2} = 0, \tag{3.9}$$

assuming homogeneous and isotropic diffusion [27] and $\delta/L \ll 1$. In this way, the domain (the flowing layer) becomes a square domain ($0 \leq \tilde{x} \leq 1$ and $-1 \leq \tilde{z} \leq 0$). Details about heap flow kinematics are provided in Appendix E. The *pdepe* routine in Matlab is used to solve equation 3.4 without the transient term. The inlet particle distributions can be arbitrarily specified (e.g., log normal or uniform), or can be based on the actual inlet particle distributions measured from experiments or DEM simulations. The boundary conditions at the free surface and bottom of the flowing layer are specified in terms of the particle distribution fluxes [91, 41, 38, 36]. Equation 3.4 is solved by discretizing $c(\tilde{\mathbf{x}},\tilde{\alpha})$ along the $\tilde{x}$ and $\tilde{z}$ directions using a regularly spaced mesh with $\Delta\tilde{x} = \Delta\tilde{z} = 0.005$. Similarly, the particle diameter, $\tilde{\alpha}$, is discretized between $\tilde{\alpha}_{\min}$ and $\tilde{\alpha}_{\max}$ with a resolution of $\Delta\tilde{\alpha} = 0.03$ to ensure solution convergence. A finite difference method using the midpoint rule is used to approximate the integral term in equation 3.4. Numerically, the inlet values for particle distributions are integrated from $\tilde{x} = 0$ to the downstream end of the heap to determine the particle diameter distribution for discretized $\tilde{\alpha}$ within the flowing domain.

To demonstrate the effectiveness of the model, we compare the steady state solutions of the continuum model to segregation patterns obtained from DEM simulations at the same operating conditions (feed rate, size distribution and inlet particle distribution). Figure 3.3 compares the segregation patterns from the model and the DEM simulations

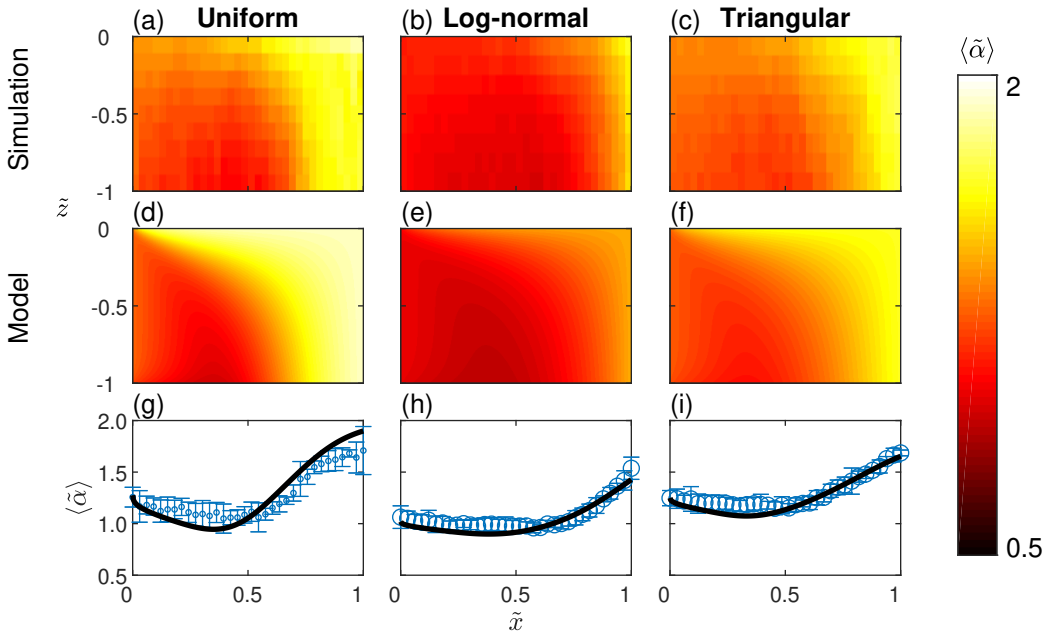

Figure 3.3. Comparison of segregation in bounded heap flow between DEM simulation and model predictions for uniform, log-normal, and triangular particle size distributions. Left column: particles distributed uniformly with $0.5 \leq \tilde{\alpha} \leq 2$ and $q = 1700$ mm^2/s. Middle column: log normal size distribution with mean $\ln(\tilde{\alpha}) = 0$ and $\sigma = 0.3$ for $0.5 \leq \tilde{\alpha} \leq 2$ with $q = 1600$ mm^2/s. Right column: triangular size distribution with $\tilde{\alpha}_{\min} = 0.5$ and $\tilde{\alpha}_{\max} = 2$ with $q = 1600$ mm^2/s. Mean dimensionless diameter, $\langle\tilde{\alpha}\rangle$, from (a-c) DEM simulations and (d-f) model predictions. (g-i) Mean dimensionless diameter, $\langle\tilde{\alpha}\rangle$, at the bottom of the flowing layer (equivalent to the mean dimensionless diameter deposited on the heap) from DEM simulations (open symbols) and model predictions (curves). Error bars indicate three standard deviations.

for three different particle size distributions, each at a different feed rate. The left column shows results for a uniform size distribution with $0.5 \leq \tilde{\alpha} \leq 2$ and $q = 1700$ mm^2/s, the middle column shows results for a truncated log-normally distributed mixture with $\ln(\tilde{\alpha}) = 0$ and standard deviation $\sigma = 0.3$ for particle diameters between $0.5 \leq \tilde{\alpha} \leq 2$ and $q = 1600$ mm^2/s, and the right column shows results for a triangular size distribution

with $0.5 \leq \tilde{\alpha} \leq 2$ and $q = 1600$ mm^2/s. The first two rows of figure 3.3 plot the local average particle diameter $\langle\tilde{\alpha}\rangle$ from DEM simulations (a-c) and model predictions (d-f) for the three different distributions and flow rates in the flowing layer. The left boundary of each panel ($\tilde{x} = x/L = 0$) is the inlet to the flowing layer from the right side of the feed zone; the top ($\tilde{z} = z/\delta = 0$) is the flowing layer surface; the bottom ($\tilde{z} = -1$) is where particles deposit onto the static portion of the heap; the right side ($\tilde{x} = 1$) represents the downstream endwall of the bounded heap. The color scale indicates the local volume averaged particle diameter, $\langle\tilde{\alpha}\rangle$, at that location. The agreement between DEM simulation and model prediction is quite good throughout the flowing layer. In all cases, larger particles (large $\langle\tilde{\alpha}\rangle$) flow further downstream than the smaller particles (lighter color on the right). As a result, they deposit further down the heap, as shown in figure 3.2. The segregation from the top of the flowing layer to the bottom is also evident as the lighter color (large $\langle\alpha\rangle$) toward the top of the flowing layer and darker color (small $\langle\alpha\rangle$) near the bottom of the flowing layer, most evident for the uniform particle distribution (figure 3.3 a and d). This is a result of the relative number of large particles in the distributions. For the log-normal and triangular distribution, the region with larger particles is smaller and the region with smaller particles is larger than for the uniform distribution because of the smaller percentage of large particles in the log-normal and triangular distribution. DEM simulation data (a-c) appears to be more pixelated than model predictions (d-f) because the simulation data is processed using a bin averaging method as done in many previous studies [27], which limits the resolution to one large particle diameter. The DEM simulation concentration data could be smoothed by using

other averaging techniques such as coarse graining [105]. Nevertheless, it would not affect the quantitative comparison at the base of flowing layer (g-i).

The average size of particles deposited on the static heap, which corresponds to the bottom edge ($\tilde{z} = -1$) of the average concentrations in figures 3.3(a-f), is shown in figures 3.3(g-i). For all three particle size distributions, the average size of the particles deposited on the heap predicted by the model matches the DEM simulation results reasonably well. That is, the smaller particles are deposited upstream and the largest particles are deposited downstream. The deviations between the model and simulations at small ($\tilde{x}$) for the uniform and log-normal distribution are likely due to small particles being trapped in the heap below the feed zone and small particles bouncing along the heap surface in the DEM simulations, both of which deplete the small particles that would have been deposited in the upstream region. These effects are less noticeable for the triangular distribution because there are relatively fewer small particles. Of course, it is possible to account for this by using the actual particle size distribution entering the left side of the computational domain thereby accounting for the particles already trapped below the feed zone. We did not do this here to show how robust the approach is even with the many simplifying assumptions.

While comparisons of the particle distributions in the flowing layer between DEM simulations and the model demonstrate good qualitative agreement, it is also possible to quantitatively compare the particle size distributions of the particles deposited on the heap at various locations along the length of the heap. Figure 3.4(a-c) shows the model and simulation predictions for particle size distributions at the bottom of the flowing layer ($\tilde{z} = -1$), which match the particles deposited on the heap, in the upstream ($\tilde{x} \leq 1/3$,

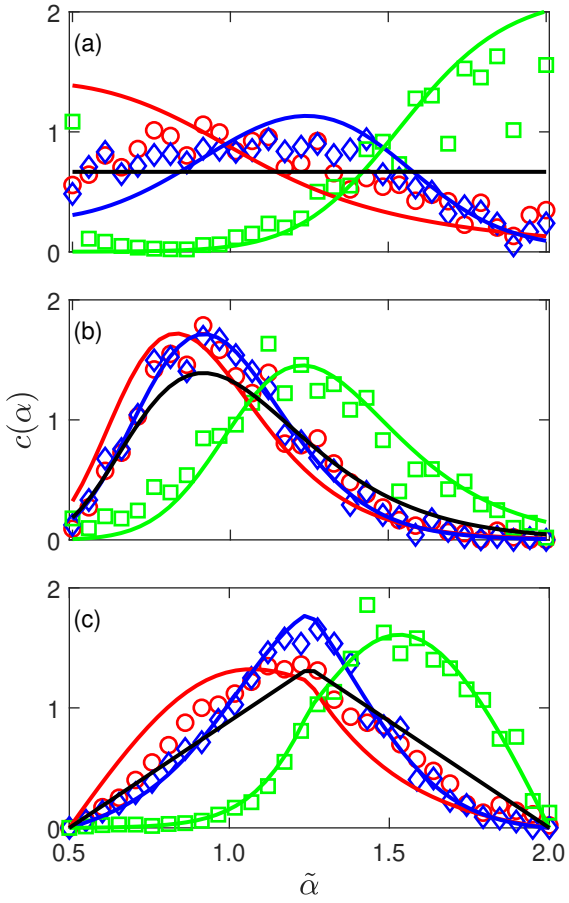

Figure 3.4. Comparison of particle size distributions in bounded heap flow between DEM simulation (open symbols) and model predictions (curves) for (a) uniform, (b) log-normal, and (c) triangular particle size distributions. Particle probability density distributions at the bottom of the flowing layer (equivalent to the size distribution of particles deposited on the heap) from DEM simulations from upstream ($\tilde{x} \leq 1/3$) (red circles), from midstream ($1/3 \leq \tilde{x} \leq 2/3$) (blue diamonds), from downstream ($\tilde{x} > 2/3$) (green squares). Black curves represent the initial particle size distributions.

red), midstream ($1/3 \leq \tilde{x} \leq 2/3$, blue) and downstream ($\tilde{x} \geq 2/3$, green) regions for three different initial particle distributions. The particles deposited upstream are smaller than those deposited downstream, while the particles deposited in the middle of the heap are

intermediate in size. The DEM simulation and model results match better in the mid-stream and downstream region than in the upstream regions. Again, this is most likely due to particles depositing in the feed zone (prior to entering the flowing layer) or bouncing along the surface, as neither effect is included in the model. Nevertheless, for these particle size distributions and feed rates, the model predictions match reasonably well with the DEM simulations. This is remarkable given that: 1) The velocity profiles are assumed to be independent of the size segregation; 2) The flowing layer thickness is assumed constant even though the flowing layer actually thins by approximately 50% in the lower 25% of the flowing layer [26]; 3) The expression for the segregation velocity is based on the linear combination of the concentration of surrounding particles (equation 3.6) and further is based on a simple linearized representation of kinetic sieving for bidisperse segregation (equation 2) using parameters found exclusively from bidisperse simulations (equation 3); and 4) The diffusion coefficient, D, is assumed constant even though it varies with both the local shear rate and particle size [27, 28].

3.4. Transient developing segregation in a rotating tumbler ($\frac{\partial}{\partial x} \neq 0, \frac{\partial c}{\partial t} \neq 0$)

To demonstrate the application of the model in a developing ($\frac{\partial}{\partial x} \neq 0$) and transient ($\frac{\partial c}{\partial t} \neq 0$) flow, we compare the model to DEM simulations of the initial segregation transient in a rotating circular tumbler in which an initially mixed polydisperse material segregates as the tumbler rotates, reaching a steady state after a few rotations. Here, for simplicity, we consider only approximately half-full circular tumblers, see figure 3.5, although the approach can be readily applied to other fill levels and tumbler geometries. The tumbler is not exactly half-full in the simulations shown in figure 3.5 for two reasons.

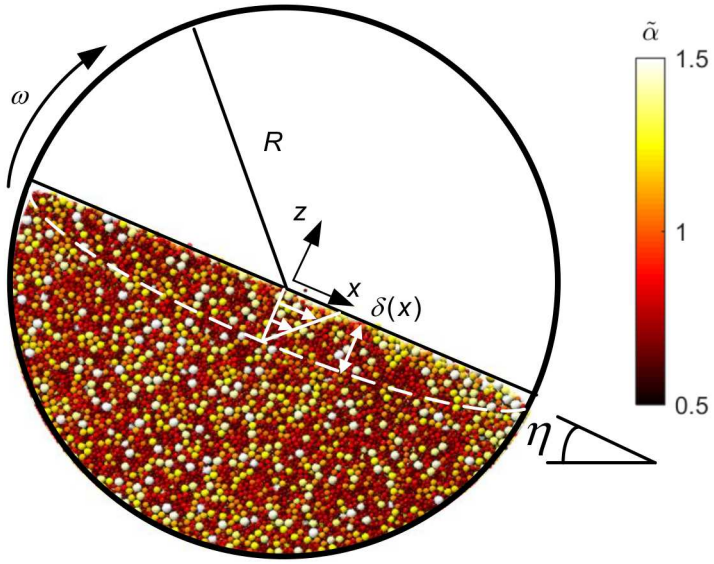

Figure 3.5. DEM simulation of size-polydisperse particles for a uniform size distribution from 1 mm (dark) to 3 mm (light) in a quasi-2D rotating tumbler of radius R and thickness T with rotation rate ω just prior to flow starting. The material has dynamic repose angle η. Dashed curve indicates the bottom of the flowing layer.

First, dilation occurs in the flowing layer upon rotation. Second, particles pack more efficiently when mixed than after segregation. Note that, we consider only continuously flowing material for which the flowing layer surface is flat. This occurs when the Froude number, $Fr = \omega^2 R/g$, which represents the ratio of inertial to gravitational forces, is in the approximate range $10^{-4} < Fr < 10^{-2}$ [74, 75]. For Froude numbers below this range, periodic avalanches occur, while above this range, cataracting or centrifuging flow occurs.

In contrast to quasi-2D bounded heap flow in the previous section, tumbler flow presents new challenges. First, the flowing layer depth varies with streamwise position, while in a quasi-2D bounded heap segregation can be accurately modeled by assuming the flowing layer depth is constant. Second, in tumbler flow the segregation is transient and depends on the number of tumbler rotations, while in bounded heap flow the segregation

is steady in a coordinate system that rises with the surface of the heap. Third, in tumbler flow particles accelerate in the upstream half of the flowing layer and decelerate in the downstream half. This is in contrast to the quasi-2D heap where the particle velocity decreases linearly down the heap. Fourth, in a tumbler, particles that exit the flowing layer to deposit in the fixed bed in the downstream region later re-enter the upstream region of the flowing layer with a different spatial distribution than the previous time they entered the flowing layer, whereas the spatial distribution of particles entering the flowing layer in a quasi-2D heap is time invariant. Specifically, particles exiting the tumbler flowing layer at bottom right remain on concentric circular streamlines in the fixed bed below the flowing layer until they re-enter the flowing layer, only to continue segregating based on size differences within the flowing layer until the segregation reaches a steady state pattern. Finally, particles in tumbler flow enter the flowing layer from the fixed bed via the curved lower boundary in the upstream portion of the flowing layer and are deposited from the curved lower boundary of the downstream portion of the flowing layer, while in the heap particles enter the flowing layer at its upstream end and are deposited along the entire length of the nearly flat bottom of the flowing layer.

Given these many differences, using equation 3.4 to model transient polydisperse segregation in a rotating tumbler presents significant challenges. Here, we used the same flow model as in a previous study [90] to describe the flow kinematics in the tumbler. Neglecting diffusion in the streamwise (x) direction and assuming D is constant in the flowing layer [27, 90], equation 3.4 is non-dimensionalized using

$$\tilde{t} = \frac{t}{1/\omega}, \tilde{x} = \frac{x}{R},\ \tilde{z} = \frac{z}{R},\ \tilde{u} = \frac{u}{R/(1/\omega)} \text{ and } \tilde{w} = \frac{w}{R/(1/\omega)} \tag{3.10}$$

and becomes

$$\frac{\partial c}{\partial \tilde{t}} + \frac{\partial}{\partial \tilde{x}}(\tilde{u}c) + \frac{\partial}{\partial \tilde{z}}(\tilde{w}c) + \frac{1-\epsilon^2}{R\epsilon^2}\frac{\partial}{\partial \tilde{z}}\int_{\tilde{\alpha}_{\min}}^{\tilde{\alpha}_{\max}} S(\tilde{\alpha},\tilde{\beta})\tilde{\dot{\gamma}}c(\tilde{\alpha})c(\tilde{\beta})d\tilde{\beta} = \frac{D}{\omega R^2}\frac{\partial^2 c}{\partial \tilde{z}^2}, \tag{3.11}$$

where $\epsilon \equiv \frac{\delta_0}{R}$, and δ_0 is the maximum flowing layer thickness. In this way, the domain (the half-filled tumbler) becomes a half-filled circle having dynamic repose angle η with $-1 \leq \tilde{x} \leq 1$, $-1 \leq \tilde{z} \leq 0$, and $0 \leq \tilde{r} \leq 1$. More details on velocity field profiles and flow kinematics are provided in Appendix F. A 3D finite element mesh generator, Gmsh [33], is used to construct a solution domain and generate a triangular mesh for the lower half of the tumbler. The dimensionless characteristic length, which prescribes the desired element mesh, of the triangular mesh throughout the solution domain is 0.01. A finite volume based partial differential equation (PDE) solver, Fipy [43], is used to solve equation 3.4. A uniform particle diameter distribution is used with particle diameter α discretized between $\tilde{\alpha}_{\min} = 0.5$ and $\tilde{\alpha}_{\max} = 1.5$ with $\Delta\tilde{\alpha} = 0.05$. The finite difference method with midpoint rule is used to approximate the integral term in equation 3.4. The Crank-Nicholson method with a non-dimensionalized time step $\Delta\tilde{t} = 0.001$ is used to update temporal development of the particle segregation. The diffusion coefficient D is based on the dependence of D on the shear rate in bounded heap flow [89, 27] using the average shear rate from the velocity field given by equation F.1 (Appendix F). The segregation length scale, $S(\alpha_i, \alpha_j)$ is taken from size bidisperse DEM simulations of one-sided bounded heap segregation [89].

To validate the model, we compare the transient solutions of the continuum model with the DEM simulations at different rotations of the tumbler starting from a mixed initial condition. Figure 3.6 shows the mean local particle diameter throughout the tumbler at 0, 1/4, 1/2, and 1 rotation. The top row displays DEM simulation results for the

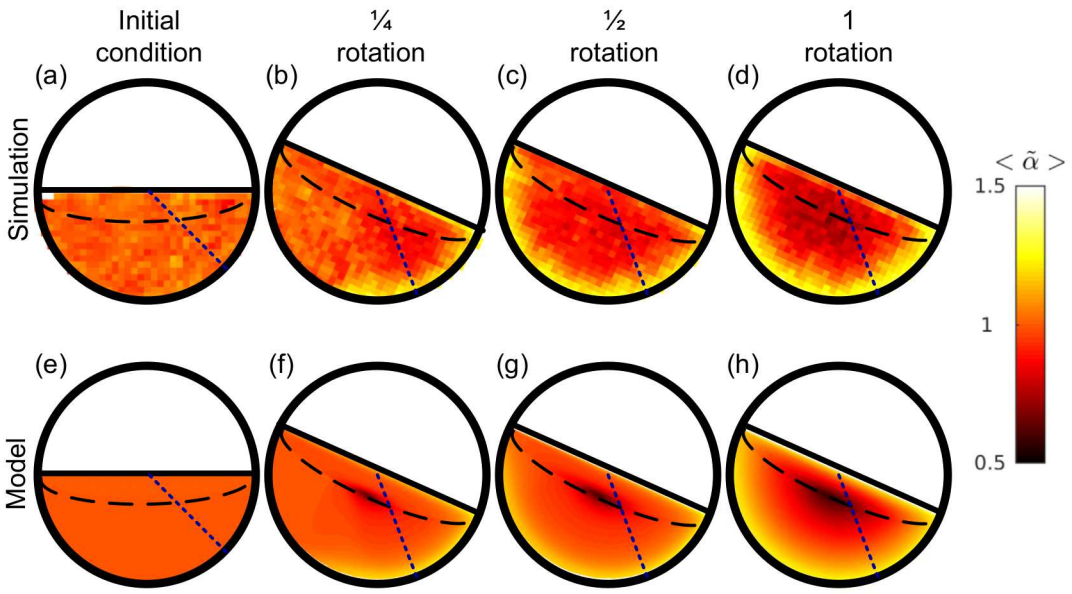

Figure 3.6. Comparison of segregation in a quasi-2D half-filled rotating tumbler with $R = 0.075$ m, $T = 0.015$ m, and $\omega = 0.25$ rad/s between DEM simulations (top row) and continuum model predictions (bottom row) for an initially well-mixed and uniformly distributed particle size distribution between $\tilde{\alpha}_{\min} = 0.5$ and $\tilde{\alpha}_{\max} = 1.5$ at 0, 1/4, 1/2 and 1 rotations. $\langle\tilde{\alpha}\rangle$ profiles along a radial slice (short dashed line) at 45° clockwise starting from the flowing layer surface are shown in figure 3.7.

average dimensionless particle diameter $\langle\tilde{\alpha}\rangle$ throughout the tumbler for an initial uniform size distribution ranging from $0.5 < \tilde{\alpha} < 1.5$ with tumbler radius $R = 0.075$ m and rotation speed $\omega = 0.25$ rad/s ($Fr \approx 5.7 \times 10^{-4}$). The bottom row depicts the corresponding continuum model predictions for the same conditions. The continuum model predictions qualitatively match the results from simulation, as shown in the figure 3.6. Specifically, after one-quarter rotation larger particles (light color) appear near the surface of the flowing layer, particularly toward its downstream end, because of segregation of the initially

mixed particles in the flowing layer. Because of this segregation, the larger particles deposit in the fixed bed at the wall of the tumbler with smaller particles depositing further inward from the tumbler wall and the smallest particles (darkest color) at the mid-length of the flowing layer just under the flowing layer. Note that the light colored band at the tumbler wall corresponding to larger particles only extends about one-quarter of the tumbler circumference from the downstream end of the flowing layer. This is because it is only these particles that have passed through the flowing layer during the one-quarter rotation of the tumbler giving them a chance to segregate. Particles that have not yet entered the flowing layer remain well mixed. By 1/2 rotation, all particles have passed through the flowing layer at least once, so the light-colored band of large particles near the wall extends the entire half-circumference of the filled portion of the tumbler. By 1 rotation, all the particles have passed through the flowing layer twice, and the segregation is enhanced compared to 1/2 rotation. As shown in figure 3.6, the segregation model predictions qualitatively match with the corresponding DEM simulation in terms of the mean particle diameter during the transient segregation.

Again, it is helpful to quantitatively compare the DEM simulations with the model predictions. To do this, we consider the average particle size along a radial line that is 45 degrees below the surface (short dashed radial lines in figure 3.6). The line extends from the midpoint of the top of the flowing layer through the flowing layer and into the fixed bed of particles. The model predictions quantitatively match the DEM simulations, temporally averaged over an interval of 2 s, as shown in figure 3.7, where the predicted mean diameter from the continuum model (solid curve) and simulations (open symbols) along the radial line match quite well. In figure 3.7(a), the average particle diameter

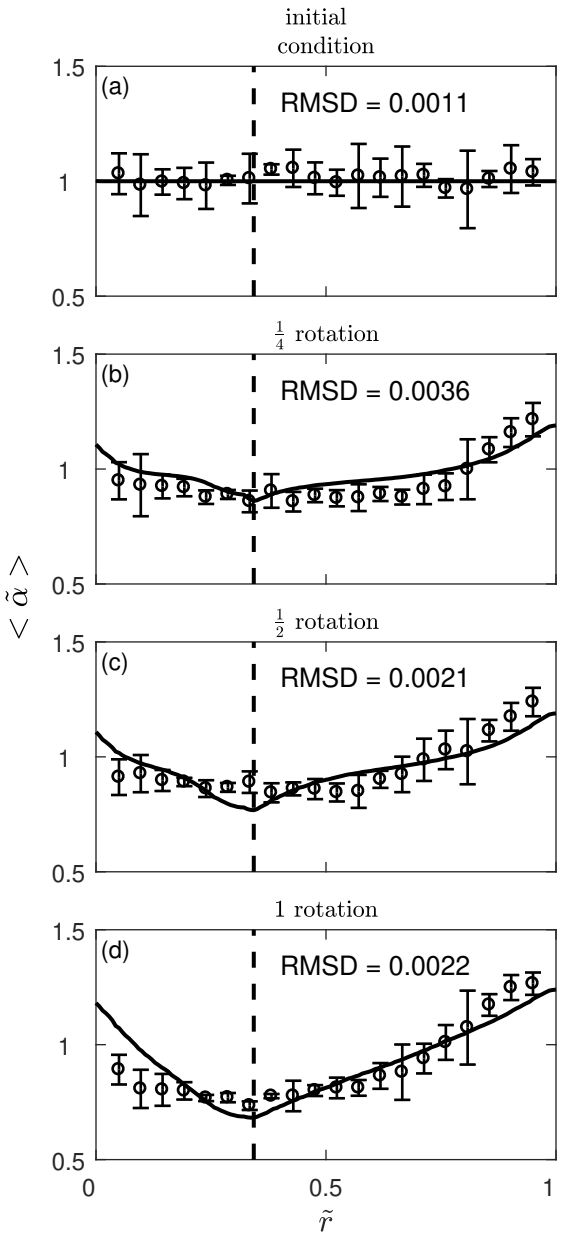

Figure 3.7. Comparison of mean particle size from simulation (open symbols) and model (curves) along a radial slice at 45° clockwise below the flowing layer surface in a half-filled rotating tumbler with $R = 0.075$ m, $T = 0.015$ m, and $\omega = 0.25$ rad/s at 0, 0.25, 0.5, and 1 rotations. Error bars indicate three standard deviations. The vertical red dashed lines indicate the location of the bottom of the flowing layer.

is uniform throughout the tumbler because no segregation has yet occurred. After one-quarter rotation in figure 3.7(b), the segregation becomes evident. In the flowing layer (to the left of the vertical dashed line), the largest particles are at $r = 0$, corresponding to the top of the flowing layer, and the particle size decreases with depth in the flowing layer to reach the smallest value at the bottom of the flowing layer (vertical dashed line). In the fixed bed (to the right of the vertical dashed line), the largest particles have deposited near the outer wall of the tumbler ($\tilde{r}$=1) due to segregation in the flowing layer. Closer to the flowing layer, but still in the fixed bed, the particle size decreases. Results are similar after 1/2 rotation, as shown in figure 3.7(c). By 1 rotation, all the particles have passed through the flowing layer twice. Consequently, the segregation is stronger both within the flowing layer (to the left of the vertical dashed line) and in the fixed bed (to the right of the vertical dashed line) compared to 1/2 rotation.

There are some minor discrepancies between the model and the DEM results evident in figure 3.7(c) close to the bottom of the flowing layer and at the periphery of the tumbler ($\tilde{r} \approx 1$). Specifically, the model and DEM simulations appear to deviate in opposite directions right at the boundary of the flowing layer. However, this is not unexpected, given the difficulty in defining the exact location of the bottom of the flowing layer and the discrete nature of the particles in the DEM simulations versus a continuum assumption in the model. The root-mean-square deviation (RMSD) is applied to quantify the quality of the theoretical predictions in the fixed bed (to the right of the vertical dash line) and is calculated as RMSD $= \sqrt{\sum_{j=1}^{n}(\tilde{\alpha}_{j,t} - \tilde{\alpha}_{j,s})^2/n}$, where $\tilde{\alpha}_{j,t}$ denotes the theoretical predictions, $\tilde{\alpha}_{j,s}$ denotes the data points from the simulation, and n is the total number of data points in the fixed bed. The discrepancy at 1/4 rotation is slightly higher,

which could be due to the fact that model did not consider the initial tumbler start-up transition. Nevertheless, the RMSDs are small, indicating that the continuum model captures the overall character of transient polydisperse segregation quite well. Again, the agreement is remarkable given the simplifying assumptions behind the model. First, the model assumes a simple linear velocity profile with a discontinuity at the bottom of the flowing layer. In fact, the kinematics from the standard tumbler model only approximate the surface velocity along the length of the flowing layer and the velocity profile in the flowing layer, as shown in Appendix F. Second, the segregation length scale, $S(\alpha_i, \alpha_j)$, is measured from bidisperse, not polydisperse or multidisperse, DEM simulations, and $w_{p,i}$ uses a linear combination of the bidisperse segregation results for the polydisperse segregation term with a simple linearization of the kinetic sieving model [86] (equation 3.2). Furthermore, the segregation length scale is measured in a completely different flow, bounded heap flow, rather than tumbler flow. Last, a constant diffusion coefficient, also measured in a bounded heap flow, is assumed. Thus, we demonstrate that the continuum model framework of equations 3.2 and 3.4 can model not only developing polydisperse size segregation (like that in a bounded heap) where $\frac{\partial}{\partial x} \neq 0$, but also combined developing ($\frac{\partial}{\partial x} \neq 0$) and transient ($\frac{\partial}{\partial t} \neq 0$) polydisperse size segregation like that in a rotating tumbler.

Density polydisperse segregation

To here, we have considered developing and transient segregation for size polydisperse granular materials and shown that predictions from the model (equation 3.4) are consistent with DEM simulation results. However, the same approach should also be

applicable to density polydisperse granular materials. Recently, Tripathi and Khakhar [102], Tunuguntla et al. [104] and Gray and Ancey [37] incorporated bidisperse density segregation into the continuum model and showed qualitative agreement with simulation results, but detailed quantitative validation of the model predictions was not presented. We have previously shown that it is possible to use an analogous approach to equations 3.2 and 3.3 for density bidisperse segregation to achieve quantitative agreement between the model, DEM simulations, and experiments [112]. In this section, we demonstrate that the same generalization of the size bidisperse interaction to the size polydisperse case works equally well for density polydisperse materials having the same particle size. While density polydisperse segregation is not as common as size polydisperse segregation, Section 3.4 provides the foundation for a future segregation model capable of simultaneously capturing the effects of both size and density polydispersity. For spherical particles of the same size but different density, the segregation length scale can be expressed as a function of the particle density ratio:

$$S(\rho_i, \rho_j) = C_D d \ln(\rho_i/\rho_j), \tag{3.12}$$

where C_D is a constant with value 0.081 for millimeter sized particles, $0.1 \leq \rho_i/\rho_j \leq 10$, and d is the particle diameter [112]. In analogy with equation 3.2, equation 3.12 captures the downward sinking of heavy particles and the upward buoyancy of light particles in a flowing bidisperse mixture.

To test the accuracy of equation 3.4 for predicting the segregation of a density polydisperse mixture, predictions of the model for segregation in a quasi-2D bounded heap

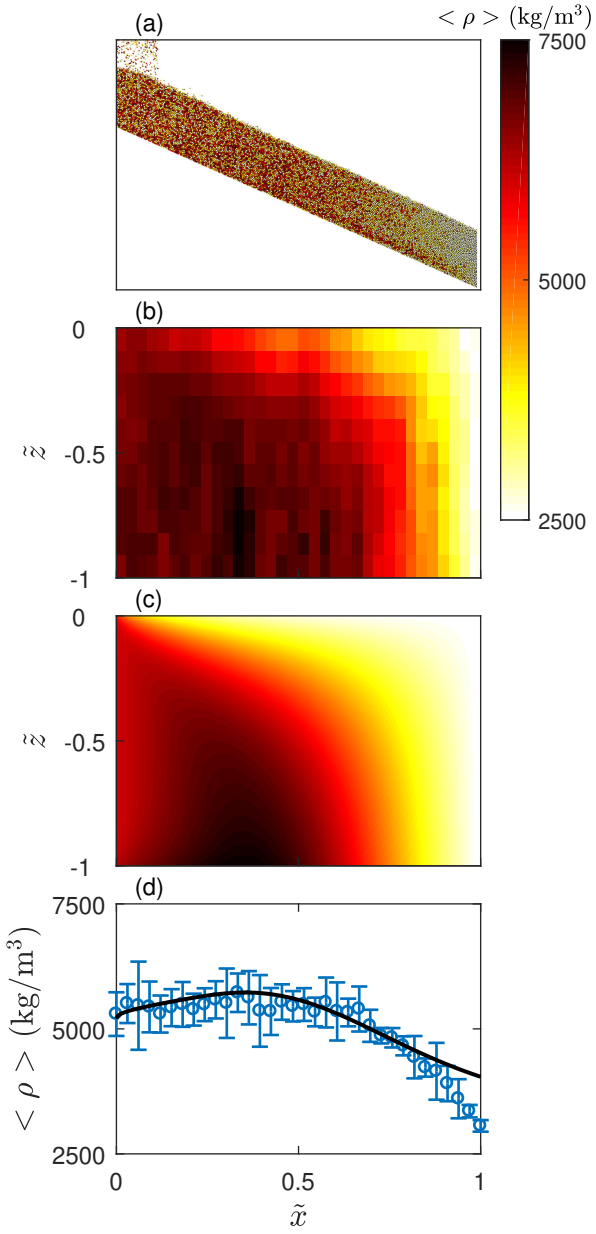

Figure 3.8. Density polydisperse segregation in quasi-2D bounded heap flow with the same dimensions as in figure 3.2 at $q = 1700$ mm^2/s. (a) DEM simulation of uniform density polydisperse distribution ($2500 \leq \rho \leq 7500$ kg/m^3). Mean local density in the flowing layer from (b) DEM simulation and (c) model prediction. (d) Mean particle density, $\langle \rho \rangle$, at the bottom of the flowing layer (equivalent to the mean density of material deposited on the heap) from DEM simulations (open symbols) and model predictions (curves). Error bars indicate three standard deviations.

(similar to those in Section 3.3) are compared to DEM simulation for polydisperse spherical particles with uniform density distribution in a quasi-2D bounded heap flow. As figure 3.8(a) shows, at a sufficiently high feed rate, an initially well-mixed density polydisperse material (same particle size) fed via a vertical feed zone flows continuously down the slope and the heap surface rises with a constant rise velocity. The heaviest particles (dark colors) sink to the bottom of the flowing layer and are deposited on the upstream portion of the heap while the lightest particles (light colors) rise to the top of the flowing layer and are advected to the downstream portion of the heap where they are deposited. The intermediate density particles rise above the heaviest but fall below the lightest particles and deposit midway along the heap. As a result, the final density distribution of particles deposited on the heap in figure 3.8(a) varies from mostly heavy particles upstream (on the left) to mostly light particles downstream (on the right). Similar to the size polydisperse case discussed in Section 3.3, some light particle are deposited on the upstream portion of the heap with the heavy particles. This is because the light particles are randomly distributed across the flowing layer thickness when they enter the flowing layer. The light particles near the bottom of the flowing layer do not have adequate time to rise to the top portion of the flowing layer before they are deposited on the upstream portion together with heavy particles. On the other hand, few heavy particles are deposited on the downstream end of the heap because they have adequate time to segregate through the entire flowing layer before reaching the downstream end wall and are deposited along the heap, leaving mostly light particles at the downstream end of the heap.

To test the model for density polydisperse segregation, we compare the steady solutions of the continuum model with DEM simulations at the same operating conditions

(feed rate, size distribution and inlet condition). The velocity profiles are identical to those used in Section 3.3 and in a previous study [112]. Figure 3.8(b, c) compares the spatial distribution of the average density in the flowing layer for an initially well-mixed uniform density polydisperse particle distribution with 2500 kg/m^3 $\leq \rho \leq$ 7500 kg/m^3 and bulk flow rate $q = 1700$ mm^2/s. Similar to figure 3.3, figure 3.8(b) shows the average local density, $\langle\rho\rangle$, measured from DEM simulation in the flowing layer (not to scale), and figure 3.8(c) shows the corresponding model prediction. As expected, heavier particles fall quickly below light particles and deposit mainly on the upstream portion of the heap; lighter particles move upward and deposit on the downstream portion of the heap. Figure 3.8(d) shows the average particle density for particles deposited onto the heap [corresponding to the bottom of figures 3.8(b,c)]. As for size polydisperse particles, the average density of the particles deposited on the heap predicted by the model matches the DEM simulation results reasonably well with a slight deviation near the feed zone due to light particles being trapped in the heap below the feed zone. Figure 3.9 further quantitatively compares the model and simulation predictions for particle density distributions of particles deposited on the heap in upstream ($\tilde{x} \leq 1/3$), midstream ($1/3 \leq \tilde{x} \leq 2/3$), and downstream ($\tilde{x} > 2/3$) sections of the heap. Results from the DEM simulations are in close agreement with predictions from the continuum model.

Conclusions

In this chapter, we have extended a model for size and density segregation [27, 91, 90, 89, 112, 19] to accurately predict segregation of polydisperse granular material in both steady developing and transient free surface gravity-driven segregation. To our knowledge,

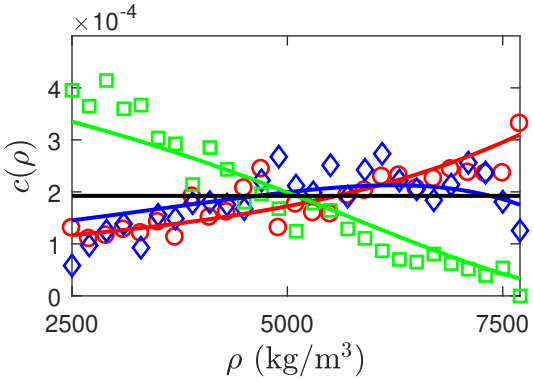

Figure 3.9. Particle density distributions at the bottom of the flowing layer (equivalent to distribution of particles deposited on the heap) from DEM simulation (symbols) and model predictions (curves). Red circles represent upstream ($\tilde{x} \leq 1/3$), blue diamonds represent midstream ($1/3 \leq \tilde{x} \leq 2/3$), green squares represent downstream ($\tilde{x} > 2/3$), and the black curve shows the initial uniform particle size distribution.

this is the first continuum model to demonstrate quantitative agreement with experimentally validated DEM simulations for polydisperse segregation in developing segregation (quasi-2D bounded heap) and in developing transient segregation (rotating tumbler flow). This is in contrast to the previously studied cases of size polydisperse segregation in periodic chute flow where $\frac{\partial}{\partial x} = 0$. In addition to size polydisperse segregation, we also extended the model to density driven polydisperse segregation. Overall, the model requires knowledge of the kinematics of the flow (specifically, the velocity field and flowing layer thickness), but involves no arbitrary fitting parameters, though the dependence of the segregation length scale on either size ratio or density ratio is based on simulations or experiments for bidisperse mixtures (equation 3.3). However, this is not a weakness in the model. It only reflects the strong effect of the particles on the degree of segregation.

While we have successfully applied a polydisperse modeling framework for segregating spherical particles in two canonical flows, the framework can be readily adapted to other

flow geometries, provided that the kinematics of the flow are known through theory, experiments, or simulations. Furthermore, the approach should be applicable to other types of particle dispersity (e.g, particle shape), provided that relations are known for the dependence of the segregation velocity on the particle dispersity (equivalent to equations 3.2 or 3.12) and for the dependence of diffusion on the kinematics of the flow. It is likely that these relations can be determined either through experiment or DEM simulation as is the case for size and density segregation. For example, we have recently determined the percolation velocity characteristics (specifically S) for rod-like particles using DEM simulations of super-ellipsoid particles [119]. Thus, using a percolation velocity based on a kinetic sieving model [86], thereby incorporating the shear rate, along with a dependence on the linear combination of the local concentration of surrounding particles having a particle-specific segregation length scale S as represented in equation 3.2, appears to be a robust approach for accurately modelling any type of polydisperse particle segregation. Furthermore, we emphasize that the segregation length scale S is not a fitting parameter but rather a physical characteristics of the granular mixture, much like the diffusion coefficient or solubility of a species in a liquid is a characteristic of the mixture that can obtained via experiment. Moreover, the advection-diffusion-segregation model (equation 3.1) provides a straight-forward, physically-connected framework for solving segregation problems in a broad range of flow geometries using only physical parameters of the problem (kinematics, segregation length scale, and diffusion coefficient), while avoiding obscure or arbitrary fitting parameters that have no physical basis or are difficult to evaluate. Hence, the approach is ideal for use in predicting segregation in industrial-scale systems as well as in the more controlled setting of the laboratory.

However, challenges remain that need to be addressed in future work. For example, we have not yet considered the interaction between simultaneous density and size effects, which have been shown to be a counter mechanism for size segregation [48, 49, 30]. We have also not yet considered the coupling between a predictive framework for the kinematics, such as the $\mu(I)$ rheology [83, 84, 39, 23, 7], and our theoretical framework or the possibility of interplay between the segregation and kinematics. These extensions will further complement the current model and advance it toward becoming a general framework for modeling particle segregation in many different flow situations.

CHAPTER 4

Modeling Segregation in Modulated Granular Flow

While granular segregation in steady flows has been investigated for various operating conditions and geometries in previous chapters, unsteady granular flows, even though ubiquitous in many industrial applications, remain largely unexplored with the exception of unsteady segregation in a tumbler. In this chapter, we consider another type of segregating granular flow, focusing on stratification in unsteady bidisperse bounded heap flow. Experiments show that periodically changing the feed rate of particles falling onto the upstream portion of a heap results in stratified segregation similar to that which occurs at low feed rates, but with more regular stratified layers of large and small particles and a higher overall feed flow rate. Here we model this stratification in a bounded heap stratification using the unsteady form of the advection-diffusion-segregation equation. Simply repeatedly switching the model from a low volume flow rate to a high volume flow rate instantaneously along the entire length of the flowing layer results in stratification patterns similar to those observed in experiments. However, it is also possible to more accurately model the moving front of particles after a change in the flow rate to further investigate the formation of stratified layers. Using a modulated feed rate offers the potential to intentionally create layers of bidisperse granular materials to enhance the effective mixing of the deposited materials at heap length scales.

Portions of the material in this chapter were published in a slightly different form in Lueptow, *et al.,* "Modeling Segregation in Modulated Granular Flow" *EPJ Web Conf*

(2017) [68] ©EDP Sciences, reprinted with permission. My contribution to this work is the application of the unsteady form of the advection-diffusion-segregation model.

4.1. Introduction

Flowing granular materials can segregate due to particle size or density differences [74, 4, 86] to form many different patterns including stratified layers of particles [70, 111, 40, 24]. The degree of segregation and nature of the segregation pattern depends on the flow conditions and the differences between particle species. Previous research on segregating granular materials in heaps has focused largely on steady feed rates [70, 25, 27]. For constant feed rates, the particles form stratified layers only at low feed rates, but segregate completely for moderate flow rates [25]. At high enough flow rates, the particles remain mixed [25]. In most industrial situations, the preference is for mixed particles to assure product uniformity. Although this can be achieved using very high feed rates, such high flow rates are sometimes difficult to accomplish in practical situations. On the other hand, if an uniform and periodic stratified pattern can be forced to occur by modulating the feed rate as shown in figure 4.1, the particles are essentially mixed at the length scale of the container. It is this situation that we investigate here.

In this chapter, we consider the impact of modulating the feed rate in order to intentionally manipulate the segregation to generate a stratified segregation pattern. To do so, we apply an advection-diffusion-segregation model that has been successfully implemented in steady segregating flows in quasi-2D bounded heaps. We demonstrate that the advection-diffusion-segregation approach can be used to model the modulation of the feed rate of mixed size bidisperse particles such that a well-ordered stratification of the small

and large particles can occur, much like that shown for experiments in figure 4.1. Such stratification may be useful in providing a better overall homogeneity at scales larger than that can be achieved without stratification for application in industrial situations such as filling a hopper.

4.2. Experiments

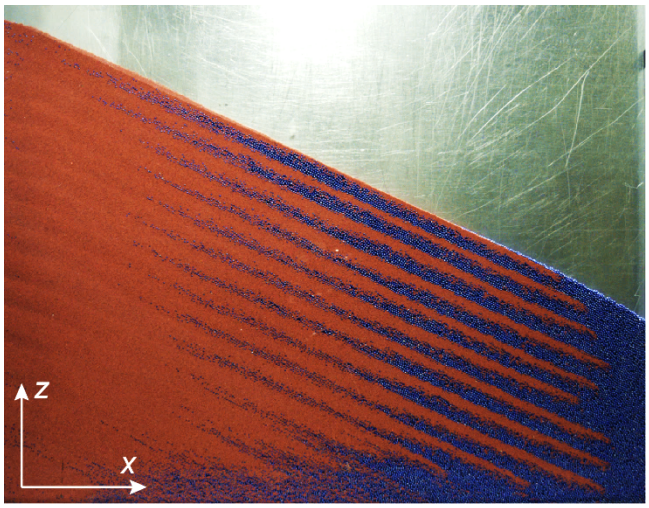

Figure 4.1. A stratified pattern (with computationally enhanced contrast) generated by feeding a size bidisperse mixture (0.5 mm red particles and 2 mm blue particles) onto a quasi-2D bounded heap with $W = 0.69$ cm and $T = 1.27$ cm at alternating feed rates of $q_f = 37.0$ cm^2/s for $t_f = 3$ s, and for $q_s = 0.4$ cm^2/s for $t_s = 62$ s. Experimental results are courtesy of Hongyi Xiao.

It is helpful to first demonstrate the formation of a stratified segregation pattern in an experimental apparatus consisting of a pair of parallel vertical rectangular plates, an aluminum back wall and a glass front wall for visualization, as described previously [113]. Spacers between the plates fix the gap at either $T = 1.27$ cm or $T = 1.5$ cm and the width at $W = 69$ cm, comparable in length to the flowing layer length in small industrial scale

silos. Well-mixed size bidisperse spherical glass particles (confirmed by direct sampling) are fed from a screw feeder into the system at the upper left corner and flow down the slope in a thin layer, segregating as they flow until they reach the bounding wall at the right side. The surface of the heap rises as particles fill the space between the front and back plates. The feed rate is modulated by using the screw feeder to feed the particles at alternating 2D flow rates $q = Q/T$: a fast flow rate q_f for duration t_f and a slow flow rate q_s for duration t_s.

A typical experimental result is shown in figure 4.1 for an equal volume mixture of small red 0.5 mm particles and large blue 2 mm spherical glass particles. As a result of the feed flow rate modulation, layers of small and large particles appear. If the flow is not modulated, but operates at the same average flow rate, irregular stratification occurs [25]. On the other hand, higher flow rate results in a segregated pattern in which the small red particles deposit on the fixed bed upstream of the large blue particles resulting in a distinct vertical boundary between the red and blue particles [25, 113]. Though completely mixed particles would be preferred, in many applications layers of particles like that shown in figure 4.1 would be preferable to completely segregated particles or particles in an irregularly stratified pattern.

4.3. Model

To understand this unsteady segregation that leads to stratification, we extend the application of a continuum transport model for segregation to accommodate the modulated heap flow. This model is based on the advection-diffusion equation with an additional

term for segregation [13] that has been successfully applied for modeling steady, developing, and transient granular flows of size segregating and density segregating materials [38, 100, 27, 104, 112]:

$$\frac{\partial c_i}{\partial t} + \underbrace{\frac{\partial (u c_i)}{\partial x} + \frac{\partial (w c_i)}{\partial z}}_{\text{advection}} + \underbrace{\frac{\partial (w_{p,i} c_i)}{\partial z}}_{\text{segregation}} - \underbrace{\frac{\partial}{\partial x}(D \frac{\partial c_i}{\partial x}) + \frac{\partial}{\partial z}(D \frac{\partial c_i}{\partial z})}_{\text{diffusion}} = 0, \tag{4.1}$$

where c_i is the concentration of species i, u and w are the mean granular velocity in the streamwise (x) and surface-normal (z) directions, respectively, in the flowing layer (note that this coordinate system differs that for the experiments in figure 4.1). The first term in the equation is the rate of change of species concentration c_i, the second and third terms account for advection due to mean flow, the fourth term accounts for segregation via a mixture-specific percolation velocity for each of the species $w_{p,i} = w_i - w$ where w_i is the local velocity component for species i and w is the local velocity component of the mixture normal to the free surface, and the last two terms account for collisional diffusion. A key aspect of this bidisperse model is the dependence of the percolation velocity of species i on the local shear rate and the local concentration of the other particle species [27, 89] such that $w_{p,i} = S\dot{\gamma}(1 - c_i)$, where S is a mixture-specific segregation length scale parameter and $\dot{\gamma} = \frac{\partial u}{\partial z}$ is the local shear rate.

Xiao et al. [113] experimentally studied segregation patterns in modulated heap flows by varying the modulation parameters q_f, q_s, t_f, and t_s. They postulated that the stratification patterns occur due to flow kinematics propagation and relaxation from the left feed zone to the right end wall. To test this hypothesis, we apply the unsteady form of the continuum transport model (equation 4.1) to the modulated heap flow. However, implementing modulated flow by varying streamwise velocity field in the continuum model

is quite challenging, because the flow rate, flowing layer thickness, local free surface rise velocity, and thus the velocity field all vary continuously with respect to time and streamwise locations. To avoid these issues, we simplify the kinematics and apply the model using conditions for fully-developed steady flow on a quasi-2D bounded heap [27], but instantaneously changing the velocity field (and thereby shear rate) and flowing layer thickness everywhere in the flowing layer from that for a low flow rate to that for a high flow rate and vice versa. In this way, the deposition of particles corresponding to the modulated feed flow rate (alternating between low and high) can be modeled. Although this approach does not account for the propagation of the flow rate change along the length of the flowing layer [114], it provides a first order approximation of the effect of a modulated feed flow rate on the particle segregation and subsequent deposition of particles on the heap.

Before solving, equation 4.1 is non-dimensionalized using characteristic streamwise and normal length scales L and δ, respectively, where L is the length of the flowing layer and δ is its thickness, and a characteristic streamwise surface velocity scale $2q/\delta$, as follows:

$$\tilde{x} = \frac{x}{L},\ \tilde{z} = \frac{z}{\delta},\ \tilde{t} = \frac{t}{\delta L/2q},\ \tilde{u} = \frac{u}{2q/\delta},\ \text{and}\ \tilde{w} = \frac{w}{2q/L}. \tag{4.2}$$

We assume that the streamwise diffusion term in equation 4.1 is negligible as a consequence of $\delta/L \ll 1$. The dimensionless governing equation for the concentration of species i after substituting in the expression for the percolation velocity $w_{p,i}$ is then:

$$\frac{\partial c_i}{\partial \tilde{t}} + \tilde{u}\frac{\partial c_i}{\partial \tilde{x}} + \tilde{w}\frac{\partial c_i}{\partial \tilde{z}} + \Lambda(1-\tilde{x})\frac{\partial}{\partial \tilde{z}}\left[g(\tilde{z}c_i(1-c_i))\right] = \frac{\partial}{\partial \tilde{z}}\left(\frac{1}{Pe}\frac{\partial c_i}{\partial \tilde{z}}\right). \tag{4.3}$$

Here $\Lambda = SL/\delta^2$ is a dimensionless parameter representing the ratio of an advection time scale $L/u = L/(2q/\delta)$ to the segregation time scale $\delta/w_{p,i} = \delta/(2Sq/\delta^2)$, and $Pe = 2q\delta/DL$ is a Peclet number representing the ratio of the diffusion time scale δ^2/D to the advection time scale $L/(2q/\delta)$. The function $g(\tilde{z}) = \dot{\gamma}(z)/(2q/\delta^2)$ is the nondimensionalized local shear rate.

Equation 4.3 is solved separately for each of the two flow rates in this problem: the fast flow rate q_f and the slow flow rate q_s. As a result, when nondimensionalizing equation 4.3 as described above, the appropriate flow rate is used resulting in different values of Pe for each of the two flow conditions. There is also an additional dimensionless parameter in this problem related to the duty cycle of the modulation of the feed flow rate. We define $\tau_j = t_j/(\delta L/2q_j)$ where j is f or s for fast and slow, respectively, which represents the duration for each flow rate t_j normalized by the characteristic residence time $\delta L/2q_j$ for particles in the flowing layer.

It is necessary to have an expression for streamwise and normal velocities, $u(\tilde{z})$ and $w(\tilde{z})$, respectively, to solve equation 4.3. To do so, we utilize standard exponential expressions for the velocity profiles. As suggested previously [27], an exponential expression $f(z) = e^{kz/\delta}$ provides an accurate approximation to the velocity profile, where k is a scaling constant. The full velocity profiles based on $f(z)$ are [27]:

$$u = \frac{kq}{\delta(1-e^{-k})}\left(1-\frac{x}{L}\right)e^{kz/\delta}$$
$$w = \frac{q}{L(1-e^{-k})}\left(e^{kz/\delta}-1\right). \tag{4.4}$$

Additionally, equations 4.4 are non-dimensionalized using the same parameters discussed previously and are expressed as:

$$\tilde{u} = \frac{k}{2(1-e^{-k})}\,(1-\tilde{x})\,e^{k\tilde{z}}$$
$$\tilde{w} = \frac{1}{2(1-e^{-k})}\left(e^{k\tilde{z}}-1\right). \tag{4.5}$$

The model of equation 4.3 and 4.5 is solved using an operator splitting approach [27, 88]. The advection step is solved with a matrix mapping method [96], and the segregation/diffusion step is solved with an implicit Crank-Nicolson method.

4.4. Model results

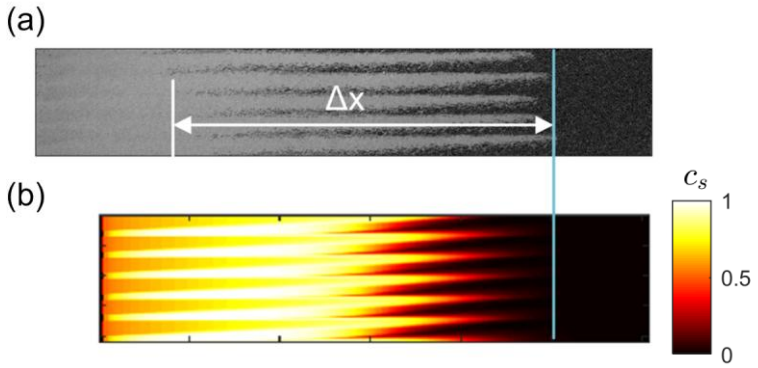

Figure 4.2. Comparison of concentration fields from (a) experiment and (b) continuum model solved with steady state parameters for bidisperse modulated bounded heap flow. Experiments used 0.5 mm (light) and 2 mm (dark) particles. Modulated feed flow conditions: $q_f = 23.6$ cm^2/s for $t_f = 5$ s, and $q_s = 2.0$ cm^2/s for $t_s = 20$ s. The extent of the model domain is reduced on the left to exclude the feed zone that is necessary in the experiment. Heap width $W = 0.69$ m and thickness $T = 0.012$ m.

Figure 4.2 compares a segregation pattern from numerical solution of the continuum model to an experiment at the same parameters (extracted from an image like that in figure 4.1) as described previously [113]. In this case, $Pe_f = 28$, $\Lambda_f = 0.65$, and $\tau_f = 2$ during the fast phase corresponds to $q_f = 23.6$ cm^2/s with $t_f = 5$ s, and $Pe_s = 5.9$, $\Lambda_s = 3.71$, and $\tau_s = 1.6$ during the slow phase correspond to $q_s = 2$ cm^2/s with $t_s = 20$ s. Lighter

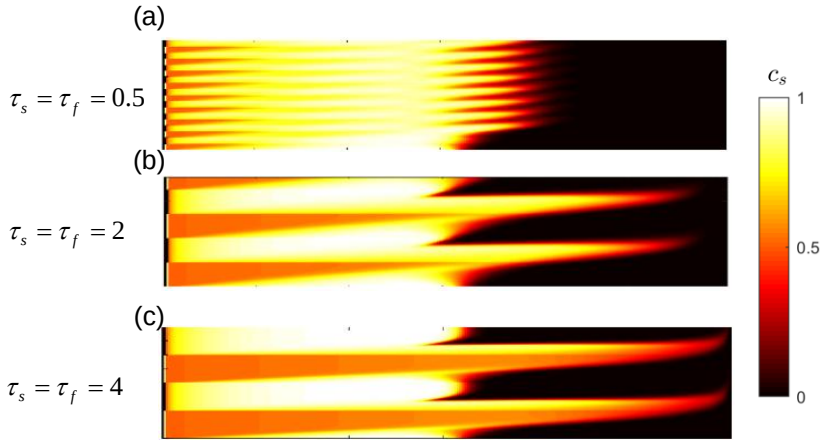

Figure 4.3. Effect of duty cycle on the deposition of particles on the heap for $\tau_f = \tau_s$. The operating condition is $\Lambda_f = 2$, $Pe_f = 60$ for the fast flow rate and $\Lambda_s = 0.067$, $Pe_s = 60$.

color represents a higher concentration of small particles, while darker color represents a higher concentration of large particles. For each stratification layer (composed of a layer of large (dark) particles and a layer of small (light) particles), the Δx characterizes the interpenetration length, which quantifies the streamwise extent of stratification. It is clear that even the simple application of the model (alternating between high and low flow rates) reproduces the stratification in the experiment quite well, particularly in terms of the interpenetration length of the stratified layers.

At this point, it is possible to consider the effect of the duty cycle on the deposition of stratified layers. Figure 4.3 shows the results of the simulation for three duty cycles with $\tau_f = \tau_s$. In all cases, the operating condition is $\Lambda_f = 2$, $Pe_f = 60$ for the fast flow rate and $\Lambda_s = 0.067$, $Pe_s = 60$ for the slow flow rate to isolate the effects of duty cycle, even though both Λ and Pe would normally change during flow rate modulation. It is evident that the value for τ_j has a significant effect on the formation of layers. First, for

$\tau_j < 1$, the duration of each flow rate is smaller than the characteristic time for a particle to flow down the slope of the heap. As a result, the duration is too short for smaller particles to deposit further than about halfway down the heap. This results in mostly small particles depositing upstream except for some short layers of small particles about halfway along the slope that extend into the region of large particles (dark region). For $\tau_j > 1$ the duration is long enough for small particles to travel far enough to deposit near the downstream end of the heap forming long layers of small particles extending into the region of large particles. This occurs during the fast flow rate (q_f) when advection is fast enough down the slope of the heap that few small particles can segregate through the thickness of the flowing layer to deposit in the upstream portion of the heap. In all cases, there are layers of mixed particles (orange) between layers of mostly small particles (yellow to white) at the upstream (left) portion of the heap. This results from some large particles that depositing in this region during the fast flow rate (q_f) because they do not have adequate time to segregate upward toward the surface before depositing on the heap.

It is also evident in figure 4.3 that the layers become thicker as τ_j increases. That is, the total time $t = t_f + t_s$ increases, so the particles are flowing for a longer time during each full cycle, resulting in thicker layers being deposited. In fact, we can compare to previous experimental data [113] for the thickness ΔH of the pair of layers deposited during one full cycle normalized by the average particle diameter $\bar{d} = (d_s + d_l)/2$ as a function of the total volume deposited on the heap, shown in figure 4.4. The match between the model data and the experimental data is quite good. Of course, this is to be expected, given that this is simply a statement of mass conservation. That is, the thickness of layers deposited

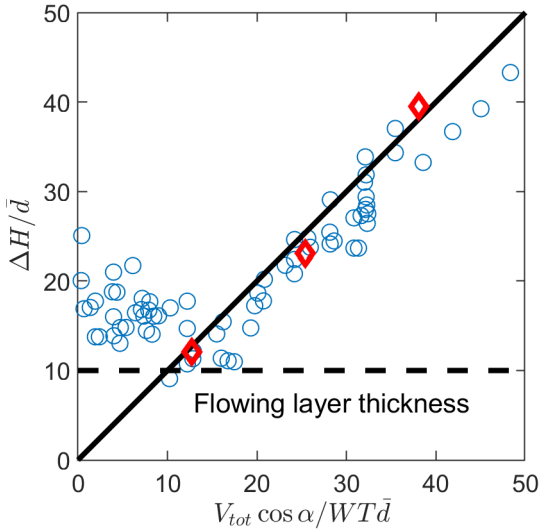

Figure 4.4. The stratification spacing ΔH as a function of the total volume of particles deposited each cycle. Experimental data (circles) reproduced from [113] and model data (diamonds) corresponding to $q_f = 23.6$ cm^2/s for $t_f = 5, 10$ and 15 s, and $q_s = 2.0$ cm^2/s for $t_s = 20, 40$ and 60 s.

during one full cycle is simply related to the volume of particles that are fed onto the heap during that cycle.

4.5. Segregation during single flow rate transition

Even though the results of simple application of the model match the stratification in the experiments quite well, it is unclear how segregation and material deposition varies in the unsteady flow that occurs during the transition between flow rates. That transition is modeled quite simplistically in the preceding figures as an instantaneous change that occurs simultaneously along the entire length of the slope of the heap. However, the transition actually propagates down the heap from the top after the flow rate changes. To further clarify the nature of the segregation, we consider the single transition that occurs when the flow rate changes from low to high or from high to low.

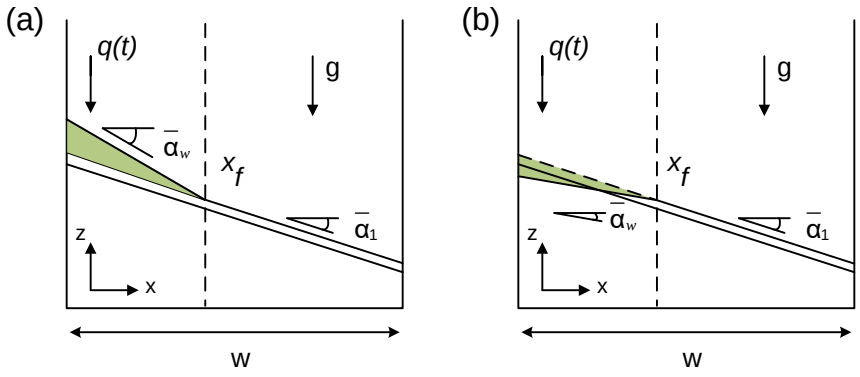

Figure 4.5. In monodisperse flow, a wedge of material inclined at angle $\bar{\alpha}_w$ propagates downstream with front location x_f, while the rest of the heap is inclined at angle $\bar{\alpha}_1$ in a W wide heap. (a) "positive" wedge in slow-to-fast transition; (b) "negative" wedge in fast-to-slow transition. From [114].

Although the focus of this chapter is a continuum approach to modeling modulated heap flow of segregating bidisperse granular materials, we review the kinematics in monodisperse flows where the feed rate is instantaneously changed to provide context. Assume that, the feed rate $q(t)$ is first set to q_1 until the flow is fully developed. Then, the feed rate is changed to different value q_2. Upon the transition, a wedge is formed that propagates downstream with the front location x_f as depicted in figure 4.5. Xiao et al. [114] showed that for a slow-to-fast rate transition ($q_1 < q_2$) shown in figure 4.5(a), after the feed rate has increased to q_2, the surface near the feedzone rises quickly and forms a wedge shape of material with an average surface angle $\bar{\alpha}_w$ that is steeper than the steady-state average surface angle $\bar{\alpha}_1$ under q_1, while the rest of the heap rises with steady state rise velocity v_{r1} under q_1. As time advances, the downstream front of the wedge labeled x_f propagates downstream until it reaches the endwall. For the fast-to-slow feed rate transition ($q_1 > q_2$) shown in figure 4.5(b), the situation is similar. After q is

reduced to q_2, the rise velocity near the feedzone decreases quickly, while the rest of the heap rises with steady state rise velocity v_{r1} under q_1, forming a "negative" wedge. The downstream front of the wedge (x_f) propagates down the heap as time advances. Using mass conservation, Xiao et al. [114] proposed a model for monodisperse flows that can capture front position during the sudden change in the feed rate as:

$$x_f = \sqrt{Ct}, \tag{4.6}$$

where x_f is the instantaneous front position and $C = \frac{2(q_2-q_1)}{\tan\bar{\alpha}_w - \tan\bar{\alpha}_1}$. Additionally, through mass balance and the local relation between the flux and surface slope, the transient local flow rate $q(x,t)$ is shown to follow a diffusion-like equation as:

$$\frac{\partial \tilde{q}}{\partial t} = A\frac{\partial^2 \tilde{q}}{\partial x^2}, \tag{4.7}$$

where $\tilde{q} = q(x,t) - q_1(1 - x/W)$, and A is a fitting parameter. Solving equation 4.7 with appropriate boundary conditions gives

$$\tilde{q}(x,t) = (q_2 - q_1)\left[1 - \frac{\mathrm{erf}(\frac{x}{\sqrt{4tA}})}{\mathrm{erf}(\frac{x_f}{\sqrt{4tA}})}\right]. \tag{4.8}$$

For regions ahead of the wedge front x_f, $q(x,t) = q_1$. With this description of monodisperse flow as background, we now consider applying the continuum model to the modulated heap flow taking into account the transient kinematics.

To apply the transport equation (equation 4.1), the velocity field in the flowing layer is needed. Four assumptions are made in order to simplify the flow kinematics calculation. First, we assume that flowing layer thickness is constant at $\delta = 10\bar{d}$, even though it varies slightly with streamwise location and depends on the flow rate [27, 89]. Second, we assume that the velocity profile in the flowing layer scales exponentially with respect to depth of the flowing layer, which is usually the case for free surface granular flows as suggested by previous studies [27]. Third, because advection is usually orders of magnitude larger than

diffusion in the streamwise direction [27], we ignore diffusion in the streamwise direction and only consider diffusion in the normal direction. Fourth, we implement the solution to equations 4.6 - 4.8 for monodisperse flow to model the propagation of the wedge during a transition from one flow rate to another, assuming that the model for the wedge in figure 4.5 is independent of the bidisperse mixture and any segregation that occurs.

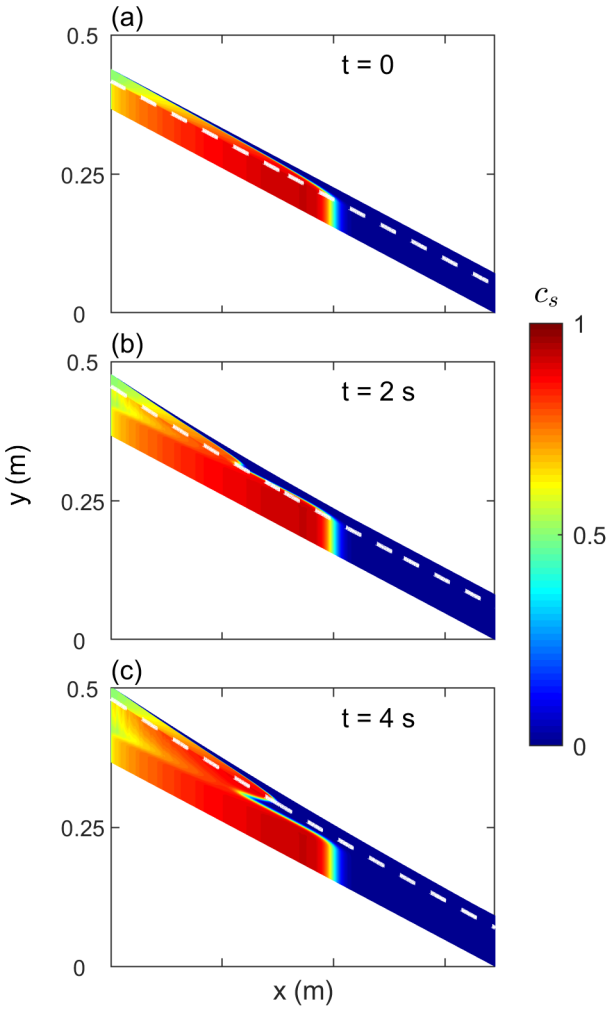

Figure 4.6. Wedge propagation in continuum model after transition from $q_1 = 35$ cm^2/s to $q_2 = 65$ cm^2/s at (a) $t = 0$, (b) $t = 2$ s, and (c) $t = 4$ s ($W = 0.69$ m and $T = 1.2$ cm).

To solve equation 4.1, the finite element method (FEM) using the Arbitrary Eulerian Lagrangian (ALE) method is implemented to handle the moving boundary for the flowing layer and bulk region, and the Streamline Upwind Petrov Galerkin (SUPG) method is implemented to stabilize advection dominated regions.

Figure 4.6 shows the segregation during wedge propagation at a transition from a slow flow rate to a fast flow rate. The steady state condition for the slow flow rate just before the transition to the fast flow rate is shown in figure 4.6(a). The large particle layer (blue) that extends upstream into the small particle region at the free surface represents large particles that have already segregated upward in the flowing layer. These particles will flow downstream much farther toward the endwall before eventually being deposited. When the fast phase starts, a large volume of mixed particles falls onto the upstream portion of the heap and flows downstream. The new particles from the high feed rate quickly form a wedge shape, the front of which propagates downstream at $t = 2$ s in figure 4.6(b). As the particles flow downstream, large particles segregate upward and move toward the free surface of the wedge while small particles percolate downward toward the bottom of the flowing layer. Because of the inclined wedge shape, large particles on the free surface move faster than the small particles deeper in the flowing layer and consequently are concentrated at the "front" of the wedge as evident at $t = 2$ s. This phenomena is much that described previously for single avalanches [83, 35]. As the fast phase continues, some large particles deposit onto the heap and are buried by small particles in the flow behind them, thus forming the large particle enriched layer in the upstream portion of the heap at $t = 4$ s in figure 4.6(c).

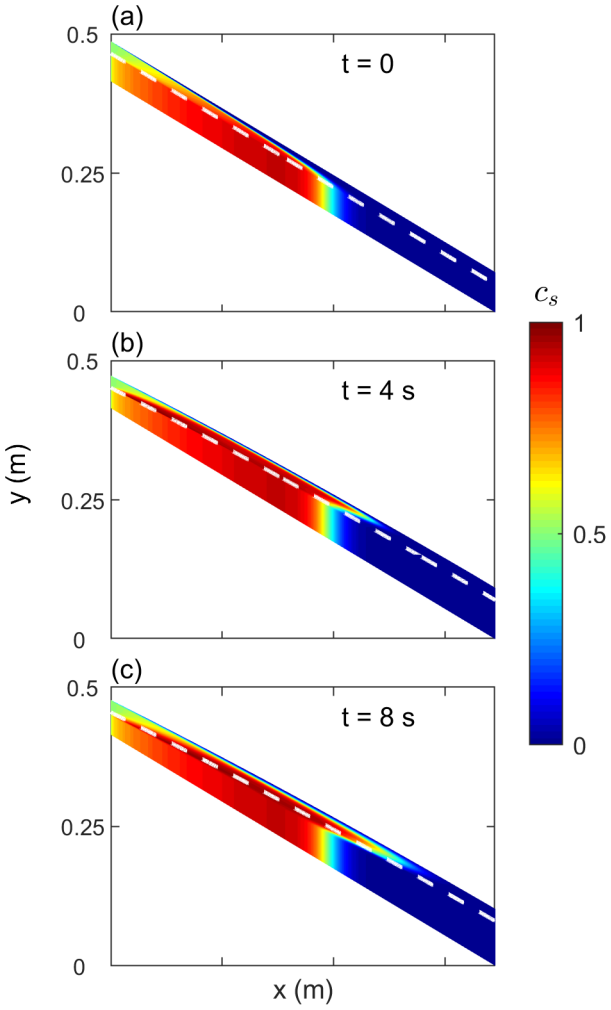

Figure 4.7. Wedge propagation in continuum model after transition from $q_1 = 35$ cm^2/s to $q_2 = 12$ cm^2/s at (a) $t = 0$, (b) $t = 4$ s, and (c) $t = 8$ s ($W = 0.69$ m and $T = 1.2$ cm).

Figure 4.7 shows the analogous process after the transition from a fast flow rate to a slow flow rate. Figure 4.7(a) shows the steady segregation at the fast flow rate just before the transition to the slow flow rate. Comparing figure 4.7(b) to figure 4.7(a), it is clear that the surface height in the upstream positions decreases during the first few seconds of the transition ($t \leq 4$ s) due to surface relaxation, forming a "negative"

wedge. Thus, some previously deposited small particles re-enter the flowing layer and are carried downstream together with the slower flowing materials. During this process, the segregation is amplified because the remaining partially mixed particles can segregate even further when they re-enter the flowing layer, which now moves more slowly than before the transition. This is most evident in the higher small particle concentrations on the bottom of the flowing layer at $t = 4$ s in figure 4.7(b). The decrease in the upstream surface height also means that the newly added particles are not deposited upstream, but are carried further downstream. Together these two effects extend the small particle layer further into the large particle region as shown in figure 4.7(c) at 8 s.

Of course, when the segregation processes in figures 4.6 and 4.7 occur sequentially, layers of large particles deposit further upstream during a slow to fast transition (figure 4.6) and layers of small particles deposit further downstream during a fast to slow transition (figure 4.7) resulting in layering of the large and small particle species.

4.6. Summary

Modulation of the feed flow rate can be used to force a stratified segregation pattern for a size bidisperse material in bounded heap flow. This may have significant advantages over the usual fully segregated pattern that otherwise occurs. For instance, if the heap is formed in a hopper that is to be emptied later, a stratified segregation pattern deposited in the hopper during the filling process using a modulated flow rate will exit the hopper as mixed particles as the layers remix, whereas a fully segregated deposition pattern upon filling the hopper will result in smaller particles exiting before larger particles exit as shown in Chapter 5 [115].

Further work is necessary to fully understand the impact of the feed flow parameters (high and low flow rate magnitudes and durations) so that they can be optimized for stratification. The stratification model shown in figure 4.2 and 4.3 is simplistic in that the transition between flow rates occurs instantaneously along the entire flowing layer length, and the flow kinematics model used here (figure 4.6 and 4.7) only considers a single isolated transition between high and low flow rates or vice versa. More work is necessary to understand the flow modulation in which multiple transitions occur simultaneously in the heap. Additionally, we have not considered the flow modulation in 3D flows, in which the sidewall friction has a much smaller influence on flow kinematics. This could lead to different forms of equations 4.6 and 4.8 and may result in different transient phenomena. Nevertheless, these results demonstrate the potential for modeling feed flow modulation and using it to intentionally generate stratified patterns in segregating granular flows.

This material is based upon work supported by the US National Science Foundation under Grant No. CBET-1511450.

CHAPTER 5

Modeling segregation of polydisperse granular materials in hopper discharge

Similiar to modulated heap flow, hopper discharge flow is an unsteady flow because particles in the flowing layer encounter different velocity fields when they reach different depths in the hopper as the hopper empties. Size segregation modeling of polydisperse materials during hopper discharge is important because hoppers are widely used in various industrial situations. However, due to the complexity of hopper discharge flow kinematics, accurate modeling of polydisperse segregation during hopper discharge has been challenging. We extend the application of a general predictive continuum model that captures the effects of segregation, diffusion, and advection to polydisperse hopper flow. Model predictions of segregation within the hopper and the average particle diameter during discharge match experimentally validated discrete element method simulations and experiments.

5.1. Introduction

Granular materials with different properties (size, density, shape, etc.) tend to segregate spontaneously when they flow. Hence, segregation has important implications in many bulk solids handling processes where a homogeneous mixture is desired for both subsequent processes and final product quality. Until recently, most mathematical approaches to modeling segregation in granular flows focused on size bidisperse mixtures

(two particle sizes). These approaches have been helpful in understanding the underlying physical mechanisms in segregating flows and in developing predictive frameworks for bidisperse segregating systems [21, 86, 22, 41, 42, 38, 100, 73, 110, 24, 99, 64, 104, 65, 27].

Multidisperse and polydisperse granular segregation (i.e., involving three or more monodisperse species or a continuous distribution of a particular particle property), though far less studied, are nevertheless frequently encountered in physical systems. These systems have been explored both in experiments [46, 80, 9, 16] and in simulations using the discrete element method (DEM) [72, 46, 82, 9] for various flow geometries. Only a handful of studies have proposed continuum models for polydisperse granular segregation, and most of these studies have been limited to the idealized case of streamwise-periodic chute flow in which periodic streamwise boundary conditions are used to model fully-developed segregation in a section of a chute [72, 71, 91].

Recently, a polydisperse segregation model that extends the continuum segregation modeling approach of Fan et al. [27] has been successfully applied to developing (spatially-dependent) segregation in a bounded heap and transient (time-dependent) segregation in a rotating tumbler [20]. However, when the flow geometry and kinematics become more complicated, polydisperse segregation becomes more challenging to predict. One such example is polydisperse segregation during hopper discharge, which has wide industrial applications in solids processing. However, due to the relative complexity of hopper geometries and flow kinematics, research on polydisperse segregation in hopper discharge flow has been limited. Previous studies on bidisperse segregation have shown that segregation depends on the hopper flow regime (mass flow versus funnel flow), initial filling conditions, and the hopper shape [57, 115].

Hopper operation can be split into two steps: filling and discharge. These steps can occur simultaneously or sequentially. In simultaneous (steady) hopper operation, the composition of discharging particles is the same as the composition of filling particles at steady state based on mass balance. However, in sequential hopper operation, significant segregation can occur during both hopper filling and discharge, making prediction of hopper discharge profiles more difficult.

In this chapter, we focus on sequential hopper operation where hopper discharge starts after the completion of hopper filling. Particles are first center fed into the hopper to form a heap. During this process, material flows continuously down the slope of the bounded heap within the hopper, and the heap surface rises uniformly (as opposed to intermittently) at a sufficiently high feed rate. Typical segregation patterns of an initially well-mixed polydisperse material fed into a hopper are small-particle enriched near the hopper center and large particle enriched near the hopper periphery. This occurs because upon falling onto the peak of the heap within the hopper, the smallest particles quickly percolate to the bottom of the flowing layer and deposit in the center portion of the hopper near the feed zone. The largest particles segregate toward the top of the flowing layer of particles and are advected further down the heap to be deposited near the hopper periphery. Intermediately sized particles deposit midway along the slope of the heap. Consequently, the final distribution of particles in the hopper varies from small particle enriched at the center to large particle enriched at the hopper periphery [19, 115], with the degree of segregation controlled by details of the particle size distribution and the flow kinematics.

The post-filling state of hopper is the initial condition for the hopper discharge process. For an initially segregated hopper presented here, mixed particles in the bottom center region flow out of the hopper first followed by the large particles near the hopper sidewalls [51, 97, 58]. On the other hand, for an initially well-mixed particles in the hopper, the discharge profile can be quite different. In this case, the initial discharge of particles is well-mixed. However, as particles continue to flow out of the hopper, the initially well-mixed outlet stream is followed by a large particle enriched phase and then by a small particle enriched phase [5, 57, 59]. This occurs as initially mixed particles segregate in the flowing layer. Changing the details of how the hopper is filled, say by setting the feed off-center from the hopper axis, can also influence the discharge profile. Additionally, changing the hopper geometry can also influence the discharge particle size profile by alternating the discharge flow (e.g., mass flow versus funnel flow) [51, 78].

It is evident then that hopper discharge segregation depends strongly on initial conditions and hopper geometry. As a result, predicting industrial scale hopper discharge can be challenging and time consuming because of the high computational cost associated with DEM simulations and the difficulty associated with scaling up lab-scale experiments. Continuum models, however, offer the potential to quickly solve and accurately predict polydisperse segregation.

Bridgwater et al. [13] were apparently the first to propose a modified advection-diffusion continuum equation with a segregation term to model segregating granular flows through a scalar transport equation. Many variations on this approach exist [21, 22, 41, 42, 38, 36, 39, 27, 91]. Here we use the approach of Fan et al. [27] and Schlick et al. [91]:

$$\frac{\partial c(\boldsymbol{x},t,\alpha)}{\partial t} + \nabla \cdot [\mathbf{u} c(\boldsymbol{x},t,\alpha)] + \frac{\partial}{\partial z}\left[w_{p,\alpha} c(\boldsymbol{x},t,\alpha)\right] = \nabla \cdot [D \nabla c(\boldsymbol{x},t,\alpha)], \tag{5.1}$$

where $\mathbf{u} = u\hat{\mathbf{x}} + v\hat{\mathbf{y}} + w\hat{\mathbf{z}}$ is the bulk particle velocity with streamwise ($\hat{x}$), spanwise ($\hat{y}$), and normal ($\hat{z}$) components, u, v, and w, respectively; $c(\boldsymbol{x},t,\alpha)$ is the probability density for a particle with diameter α at position $\boldsymbol{x}$ at time t; D is a diffusion coefficient that accounts for random particle collisions (remixing); and $w_{p,\alpha} = w_\alpha - w$ is the percolation velocity of particles with diameter α as determined by the difference between the velocity of particles with diameter α normal to the free surface, w_α, and the mean normal flow velocity, w. This model is an extension of the bidisperse segregation model that has been applied and validated in bounded heaps [27, 89] and rotating tumblers [90]. More recently, this model was extended to model tridisperse segregation in inclined chutes [19], tridisperse segregation in bounded heaps [91], polydisperse segregation with relatively simple flow kinematics in fully developed steady streamwise-periodic chute flow [91], and polydisperse segregation in bounded heaps and rotating tumblers [20]. Results using this approach agree well with validated DEM simulations and experiments.

The key to modeling of polydisperse segregation is an accurate expression for the component of the segregation velocity normal to the free surface, $w_{p,\alpha}$. The relation used here is based on an integral form of a linearization of Savage and Lun's kinetic sieve model [86, 55] for size bidisperse mixtures composed of particles with diameters α_i and α_j [91, 27]. In this approach, the segregation velocity of particles with diameter α depends on the local shear rate, $\dot{\gamma}$, and the local particle probability distribution (akin to concentration), $c(\boldsymbol{x},t,\beta)$, as

$$w_{p,\alpha} = \int_{\alpha_{\min}}^{\alpha_{\max}} S(\alpha_i,\alpha_j)\dot{\gamma} c(\boldsymbol{x},t,\beta) d\beta, \tag{5.2}$$

where $S(\alpha_i, \alpha_j)$ is an empirically determined segregation length scale dependent on particle size ratio and diameters [89] as well as gravity and the local pressure [31]. $S(\alpha_i, \alpha_j)$ in equation 5.2 is well-approximated by the relation:

$$S(\alpha_i, \alpha_j) = B \min(\alpha_i, \alpha_j) \ln(\alpha_i/\alpha_j), \tag{5.3}$$

where B is a dimensionless constant independent of particle size [89]. Based on one-sided bounded heap DEM simulations of mm-sized spherical glass particles with size ratios, $1/3 \leq \alpha_i/\alpha_j \leq 3$, $B = 0.26$ [89] (we use this value for the rest of this chapter). For size ratios outside this range, $S(\alpha_i, \alpha_j)$ could still be measured by performing bidisperse bounded heap DEM simulations similar to previous work [27, 89] or by extracting S from experiments, even though the functional dependence on size ratio might be different. Equations 5.2 and 5.3 capture the downward percolation of small particles due to kinetic sieving and the upward movement of large particles due to squeeze expulsion in flowing size polydispese mixtures [86, 20].

In this chapter, we apply the general continuum model for polydisperse segregating materials (equation 5.1) to the hopper discharge flow and validate the model using DEM simulations with polydisperse particle size distributions and experiments with quasi-polydisperse size particle distributions using several particle species with relatively narrow size distributions. Lastly, we explore the effects of initial particle distributions and hopper geometries on the hopper discharge profile to demonstrate the potential of the modeling approach for a range of practical applications.

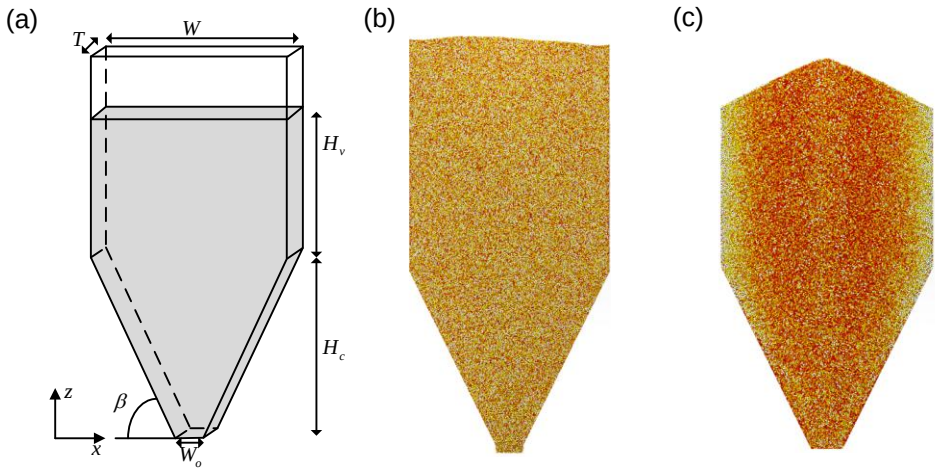

Figure 5.1. (a) Schematic of a quasi-two-dimensional hopper of width $W = 0.4$ m and thickness $T = 0.012$ m with bottom hopper wall inclined at $\beta = 65°$ and outlet width $W_o = 0.06$ m. Initial conditions for DEM simulation of hopper discharge of size polydisperse mixtures with a truncated log-normal size distribution 1 mm (red) $\leq \alpha \leq$ 4 mm (white) for (b) mixed initial condition and (c) segregated initial condition due to hopper filling.

5.2. Polydisperse segregation during hopper discharge

We consider size polydisperse segregation in a hopper discharge flow for both an initially well-mixed hopper and an initially segregated hopper for the same hopper geometry (see figure 5.1(a)) used in a previous study of size bidisperse segregation [115]. The quasi-2D hopper has inlet width W, outlet width W_o, and gap thickness T. The initial height of the material in the vertical section (parallel walls) is H_v. The height of the converging section with sidewalls inclined at β from horizontal is $H_c = (W - W_o)\tan(\beta)/2$. The origin of the coordinate system is the lower-left corner of the setup with x horizontal and z vertical.

We compare results of the continuum model approach with DEM simulations. Details of the DEM simulations are provided in Appendix B. We consider a truncated lognormal

size distribution with mean $\ln(\tilde{\alpha}) = 0.27$ and characteristic width $\sigma = 0.3$ for $0.5 \leq \tilde{\alpha} \leq 1.5$, where $\tilde{\alpha} = \alpha/d_0$ and d_0 is a typical particle diameter set to $d_0 = 2$ mm in this study. Two different initial conditions are considered: a well-mixed initial condition (figure 5.1(b)) and a segregated initial condition (figure 5.1(c)). For the well-mixed initial condition, the feed width equals the hopper width (W) in the DEM simulations so that no heap forms during the filling and deposited particles remain well-mixed (figure 5.1(b)). While this initial condition does not correspond to a typical industrial setting, it is helpful to consider as it isolates segregation during hopper discharge [5, 57, 58, 85]. The segregated initial condition is generated in the DEM simulations by feeding particles in a narrow region ($W_f = 0.04$ m) at the center of the hopper at a 2D volumetric flow rate q_f [27], which forms a heap. A typical heap segregation pattern is shown in figure 5.1(c), in which small particles (red) deposit in the center portion of the hopper and large particle (yellow and white) deposit near the sidewalls [25]. The lighter color at the centerline in figure 5.1(c) consists of mixed large and small particles because these particles have inadequate time to segregate before being deposited on the heap. This initial condition corresponds to hopper filling segregation in typical industrial settings [97, 44].

5.3. Continuum modeling of hopper discharge segregation

5.3.1. Well-mixed hopper

We first examine hopper discharge starting with a well-mixed initial condition because it removes the influence of segregation that occurs during hopper filling. Although the focus in this chapter is a continuum approach to modeling hopper discharge, we begin with DEM simulations to provide context. Figure 5.2 shows an example of hopper discharge using the

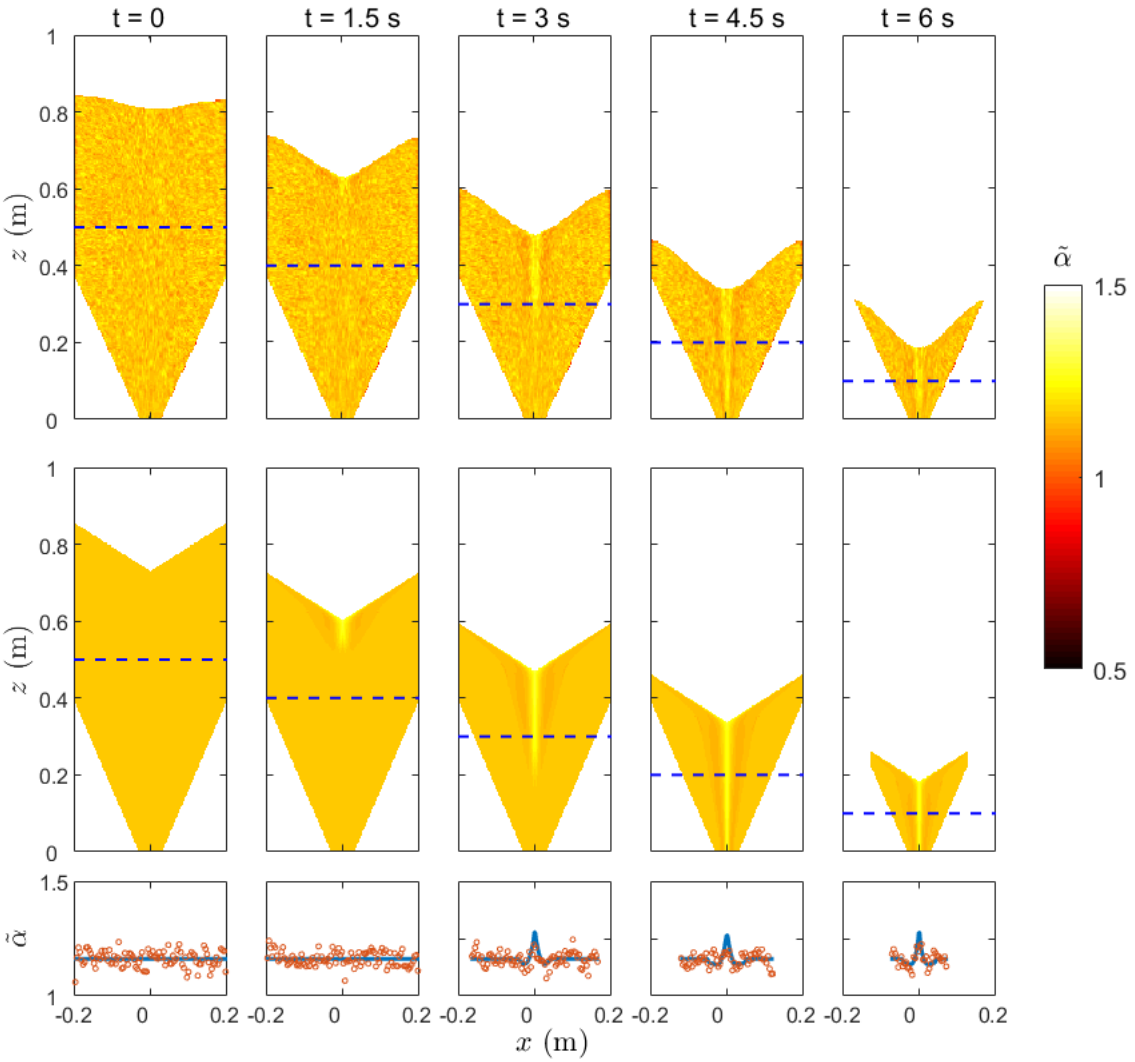

Figure 5.2. Comparison of mean local particle diameter for size-polydisperse segregation in hopper discharge flow between (top row) DEM simulations and (middle row) model predictions for a mixed initial condition hopper with $W = 0.4$ m, $W_o = 0.06$ m, $\beta = 65°$, $H_v + H_c = 0.84$ m at different stages of hopper discharge. Log normal particle size distribution with mean $\ln(\tilde{\alpha}) = 0.27$ and $\sigma = 0.3$ for $0.5 \leq \tilde{\alpha} \leq 1.5$. (bottom row) Average particle radius, $\bar{\alpha}$, at different depths (blue dashed line) from DEM simulations (symbols) and model predictions (curve).

DEM simulation with a well-mixed and nominally flat free surface initial condition. At $t = 0$, the particle mixture is well-mixed and has average radius $\bar{\alpha} = 2.3$ mm throughout the hopper. After the hopper outlet opens, the upper free surface quickly forms a V-shape, consistent with observations from previous experiments and simulations [115]. The V-shape is maintained throughout the hopper discharge process as shown in figure 5.2 (top row). During the transition from the flat to the V-shape, minimal segregation occurs. As a result, the first particles exiting the hopper are mixed ($t = 1.5$ s). After the V-shape forms, segregation becomes evident along the centerline extending from the low point of the V-shaped surface as shown in figure 5.2 ($t = 3$ s). The large particles that segregated as they flowed down the V-shaped surface form a narrow vertical line along the centerline of the hopper and move downward as the heap discharges. Small particles, in contrast, are enriched on both sides of the vertical line of large particles, again due to segregation in the free surface flowing layer, and extend toward the outlet as well. Other regions of the hopper remain well-mixed including the particles exiting the hopper ($t = 3$ s). As particles flow out of the hopper through the outlet, the V-shaped free surface continuously moves downward. As a result, particles just below the V-shaped surface flowing layer are subsumed into the surface flowing layer and flow toward the hopper centerline. As particles in the surface flowing layer flow toward the hopper center, small particles percolate toward the bottom of the flowing layer, and large particles rise upward toward the free surface until they meet the particles from the other side of the V-shaped surface. The partially segregated layers converging from the right and left merge at the base of the V-shape and flow downward. In the process they form a sandwich of large particles bounded on either side by a small particle enriched layer. This segregation

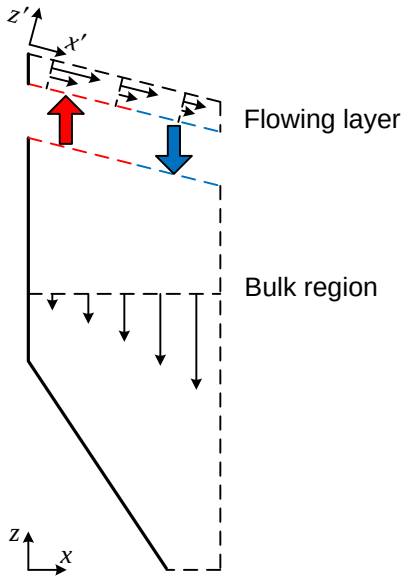

Figure 5.3. Schematic of kinematic coupling between flowing layer and bulk in hopper discharge flow showing local flowing layer coordinates (x', z') and fluxes into (red) and out of (blue) the flowing layer in a co-moving frame.

pattern persists through the remainder of the hopper discharge process, even after the free surface reaches the converging flow section of the hopper, and the segregated large particles at the centerline eventually reach the hopper outlet ($t = 4.5$ s and $t = 6$ s).

With this description of the flow and segregation as background, we now consider the detailed flow kinematics and continuum model for hopper discharge. Due to its reflection symmetry, we only consider the left half of the hopper as depicted in figure 5.3. This half is split into two regions [115]: the flowing layer and the bulk flow region. Material at the interface between the flowing layer and the bulk region is exchanged continuously during discharge, as depicted in figure 5.3 by the large red and blue arrows. Two assumptions are made in order to simplify the flow kinematics calculation. First, we assume that each side of the V-shaped free surface is straight and inclined at a constant angle η during the entire hopper discharge process. Second, we assume that the flowing layer thickness

is constant at $\delta = 15\bar{d}$, even though it varies slightly with streamwise location [115, 27]. With these assumptions, the instantaneous position of the interface between the bulk region and the flowing layer can be calculated from mass conservation since the volume of particles between the location of the free surface at time t_0 and its location at time t equals the discharged volume, $Q(t - t_0)/2$, where Q is the volumetric discharge rate, considering only one side of the hopper. In this way, the position of the interface between the flowing layer and the bulk region can be calculated in both the non-converging and converging portions of the hopper. Additionally, the descent velocity of this surface can be calculated from the time derivative of the interface position. If we define the particle velocity relative to the moving interface velocity as $\boldsymbol{u}_r = u_r\boldsymbol{x'} + w_r\boldsymbol{z'}$, the region where $w_r + u_r \tan(\eta) > 0$ is the portion of the interface where particles leave the bulk region and enter the flowing layer, as marked by the red arrow and red dashed lines in figure 5.3, and the region where $w_r + u_r \tan(\eta) < 0$ is the portion of the interface where particles leave the flowing layer and enter the bulk region, as marked by the blue arrow and blue dashed lines in figure 5.3.

To apply the transport equation (equation 5.1), velocity fields in both the flowing layer and the bulk region are needed. A kinematic model exists that can capture the bulk velocity field in both the parallel and converging regions of the quasi-2D hopper [78, 79, 15, 115]. The model is based on the assumption that the horizontal velocity is proportional to the horizontal gradient of the vertical velocity component [78, 79, 15] as

$$u = -b\frac{\partial w}{\partial x}, \tag{5.4}$$

where b is a kinematic scaling parameter with dimensions of length. Previous studies have found that b does not significantly affect prediction of velocity; b is usually chosen

between $1.5\bar{d} \leq b \leq 4.5\bar{d}$ where $\bar{d}$ is the average particle diameter [15, 115]. Here, we use $b = 3\bar{d}$ and solve the kinematic model using the same numerical scheme used in previous studies [15, 115]. The velocity field in the flowing layer is constructed separately by using information from the kinematic model for the bulk region, which defines the flows (red and blue arrows) across the interface in figure 5.3, and a velocity profile from DEM simulations [115]. The velocity in the flowing layer can be well approximated by an exponential function $u/u_s = \exp[k(z - z_s)/\delta]$, where u_s is the streamwise velocity at the free surface, z_s is the free surface location, and δ is the flowing layer thickness, which is defined as the depth where $u = 0.1u_s$ [115, 27]. Because segregation is initiated in the flowing layer at the free surface of the hopper, the modified transport equation (equation 5.1) is applied in the flowing layer, while the standard advection diffusion equation (equation 5.1 with $w_{p,\alpha} = 0$) is applied to the bulk region where no or minimal segregation occurs. Material at the interface between the flowing layer and bulk region is exchanged continuously as indicated by the red and blue arrows in figure 5.3.

In the flowing layer, similar to other quasi-2D geometries such as bounded heap flow and rotating tumbler flow [27, 90, 20], the segregation term in equation 5.1 acts normal to the free surface. Consequently, equation 5.1 can be solved more readily in a coordinate system moving downward with the flowing layer, having its origin at the upper-left corner of the flowing layer, the streamwise direction x' parallel to the free surface, and the normal direction z' perpendicular to the free surface, as depicted in figure 5.3. Because advection-driven fluxes are usually orders of magnitude larger than diffusion-driven fluxes in the streamwise direction [27], we ignore diffusion in the streamwise direction and only consider diffusion in the normal direction. As in previous studies [28, 102, 106], the

diffusion coefficient in the bulk and the flowing layer is calculated as:

$$D = C_D \dot{\gamma} \bar{d}^2, \tag{5.5}$$

where C_D is a material-dependent constant [28, 102, 106] and $\bar{d}$ is the average particle diameter [28]. Here we use $C_D = 0.1$, consistent with a previous study [115]. Similar to a previous study [115], a finite element method (FEM) using the Arbitrary Eulerian Lagrangian (ALE) method is implemented to handle the moving boundary for the bulk region and the Streamline Upwind Petrov Galerkin (SUPG) method is implemented to stabilize advection dominated regions. The particle diameter, $\tilde{\alpha}$, is discretized between $\tilde{\alpha}_{\min}$ and $\tilde{\alpha}_{\max}$ with a resolution of $\Delta\tilde{\alpha} = 0.03$ to ensure solution convergence. A finite difference method using the midpoint rule is used to approximate the integral term resulting from substituting equation 5.2 in equation 5.1.

The continuum model segregation predictions for the local mean particle diameter in an initially well-mixed hopper during discharge are shown in the middle row of figure 5.2. Note that he model is solved for the left side of the hopper and the results are reflected across the centerline in the figure. For simplicity, the model starts with a V-shaped upper surface having the same repose angle as in the DEM simulations after the V-shape has formed. When discharge begins, the continuum model captures the large particle enrichment at the free surface seen in the DEM simulation ($t \leq 1.5$ s). The large particles rise to the surface of the flowing layer and are advected in the flowing layer toward the hopper centerline to be carried downward at the centerline in the hopper bulk. The small particles percolate downward toward the bottom of the flowing layer and are carried into the bulk flow just outside of the center region. At the same time particles on interface between the flowing layer and the bulk region exchange continuously based on the local

particle velocity relative to the moving interface. That is, particles close to the hopper centerline (right side of the portion of the interface marked in blue in figure 5.3) exit the bottom of the flowing layer, enter the bulk region, and are then transported by the bulk flow toward the outlet in a large particles enriched region at the centerline. The large particles are surrounded by regions that are slightly enriched with small particles on either side ($t = 3$ s and $t = 4.5$ s in figure 5.2). This results from small particles at the interface but farther from the centerline (left side of the portion of the interface marked in blue in figure 5.3) entering the bulk region being transported by the bulk flow toward the exit. Although it is not evident in figure 5.2, particles closer to the sidewall (portion of the interface marked in red in figure 5.3) leave the bulk region, enter the flowing layer, and segregate as they flow down the surface flowing layer. Segregation in the model prediction occurs slightly earlier than in the DEM simulation as is most evident in comparisons at $t = 1.5$ s and $t = 3$ s in figure 5.2. This is because the continuum model starts with a V-shaped surface instead of a flat surface as in the DEM simulations. Nevertheless, because the transition time from a flat surface to the V-shaped surface is short, the segregation predicted by the model still agrees well with the DEM simulations.

The bottom row of figure 5.2 further compares horizontal profiles of the average particle diameter, $\bar{\alpha}$, at different depths in the hopper (indicated by the horizontal blue dashed lines) at different stages of the hopper discharge. When hopper discharge begins, the segregated particles initially in the flowing layer have not yet reached the level in the hopper marked by the blue dashed lines ($t = 0$ and $t = 1.5$ s). Consequently, $\bar{\alpha}$ from DEM simulations (circles) and continuum model (solid curve) remain nearly constant across the width of the hopper and match the mean of the initial well-mixed particle

distribution. As the discharge continues, the segregated particles are transported by the bulk flow through the hopper bulk and toward the outlet. This is evident by a small peak in the $\bar{\alpha}$ profile corresponding to large particles at the center of the hopper and a slight dip in average diameter on either sides in both DEM simulation and continuum model at later stages of the hopper discharge ($t \geq 3$ s). Overall, the continuum model predictions agree well with DEM simulation at different depths of the hopper bed and at different times during discharge.

Because segregation mainly occurs in the free surface flowing layer and propagates downward in the hopper with the bulk flow, it is important to demonstrate the effectiveness of the model in the flowing layer. Figure 5.4 compares DEM simulations (figure 5.4(a)) and continuum model predictions (figure 5.4(b)) for segregation in the flowing layer. In both subfigures, the left boundary ($\tilde{x} = x/L = 0$) is the left sidewall of the hopper; the top ($\tilde{y} = y/\delta = 1$) is the flowing layer free surface; the bottom boundary ($\tilde{z} = 0$) is the bottom of the flowing layer; and the right boundary ($\tilde{x} = 1$) is the hopper centerline. The color scale indicates the local volume averaged particle diameter, $\bar{\alpha}$. Once large particles enter the flowing layer, they segregate upward toward the free surface and flow to near the hopper centerline. The small particles percolate downward toward the bottom of the flowing layer. At the same time, however, mixed particles enter the upper half of the flowing layer through its bottom boundary (red arrow and dashed line in figure 5.3). As a result, particles remain mixed throughout most of the flowing layer with only a slight enrichment of small particles moving downstream. The only obvious evidence of segregation is the lighter color at the downstream (right) end, which corresponds to larger particles in the flowing layer that enter the bulk region at the centerline of the hopper.

Figure 5.4(c) further compares the average diameter, $\bar{\alpha}$, at the bottom of the flowing layer ($\tilde{z} = -1$) from DEM simulation (open symbols) and the corresponding continuum model prediction (solid line). As shown in figure 5.4(c), the average size of the particles on the bottom of the flowing layer predicted by the model matches the DEM simulation results: the largest particles are concentrated near the hopper center, but elsewhere the particles are mixed. This is to be expected in the upstream portion where mixed particles are entering the bottom of the flowing layer from the mixed bulk. As the flow re-orients to the vertical direction (blue arrow and dashed line in figure 5.3) in the downstream portion of the flowing layer, segregated flowing layer creates the sandwich-like pattern shown in figure 5.2, in which mixed particles slightly enriched with small particles bound both sides of the large particles enriched region on the centerline.

5.3.2. Initially segregated hopper

Compared to an initially well-mixed hopper, an initially segregated hopper represents a more common situation for industrial applications. Figure 5.5(top row) shows an example of a DEM simulation of hopper discharge with a segregated initial condition that forms when a well-mixed polydisperse particle mixture is fed into the center of the hopper. The initial segregated condition comes about during filling as particles flow down the slope of the heap forming in the hopper. As they flow, small particles percolate to the bottom of the flowing layer and deposit onto the upstream portion of the heap, which corresponds to the central region of the hopper, while large particles flow further down the heap to deposit onto the downstream portion of the heap near the side walls, resulting in the segregation pattern shown at $t = 0$ s. When the discharge begins, the heap at the surface

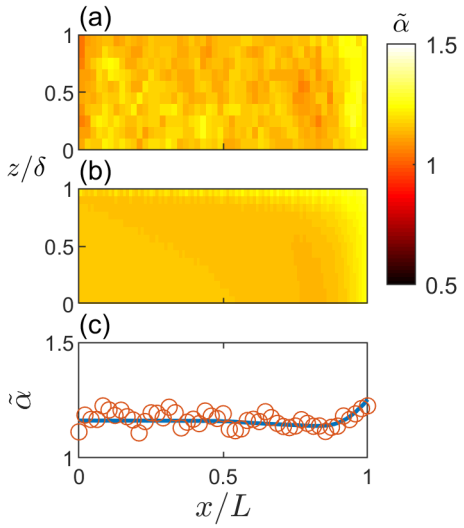

Figure 5.4. Comparison of DEM simulation and continuum model prediction for the average diameter $\tilde{\alpha}$ in the flowing layer for a mixed initial condition with $W = 0.4$ m, $W_o = 0.06$ m, $\beta = 65°$, $H_v + H_c = 0.84$ m. Truncated log-normal size distribution with mean $\ln(\tilde{\alpha}) = 0.27$, $\sigma = 0.3$ and $0.5 \leq \tilde{\alpha} \leq 1.5$. (a) Instantaneous average diameter distribution at $t = 2.4$ s from (a) the DEM simulation and (b) the continuum model. (c) Comparison of average diameter at the bottom of the flowing layer between continuum model prediction (solid curve) and DEM simulation (circles).

inverts to become V-shaped. Once the V-shaped surface forms ($t = 1.5$ s), particles flow down the slope. Large particles from near the sidewalls segregate upward in the flowing layer toward the free surface, and are transported toward the center, resulting in a large particle enriched region at the hopper center. At the same time, particles in the bulk region are transported downward by the bulk flow toward the hopper outlet creating a segregation pattern with large particle enriched regions at the hopper sidewalls and centerline and small particle enriched regions between between the walls and the center of the hopper ($t = 3, 4.5,$ and 6 s). As a result, the first particles exiting the hopper are

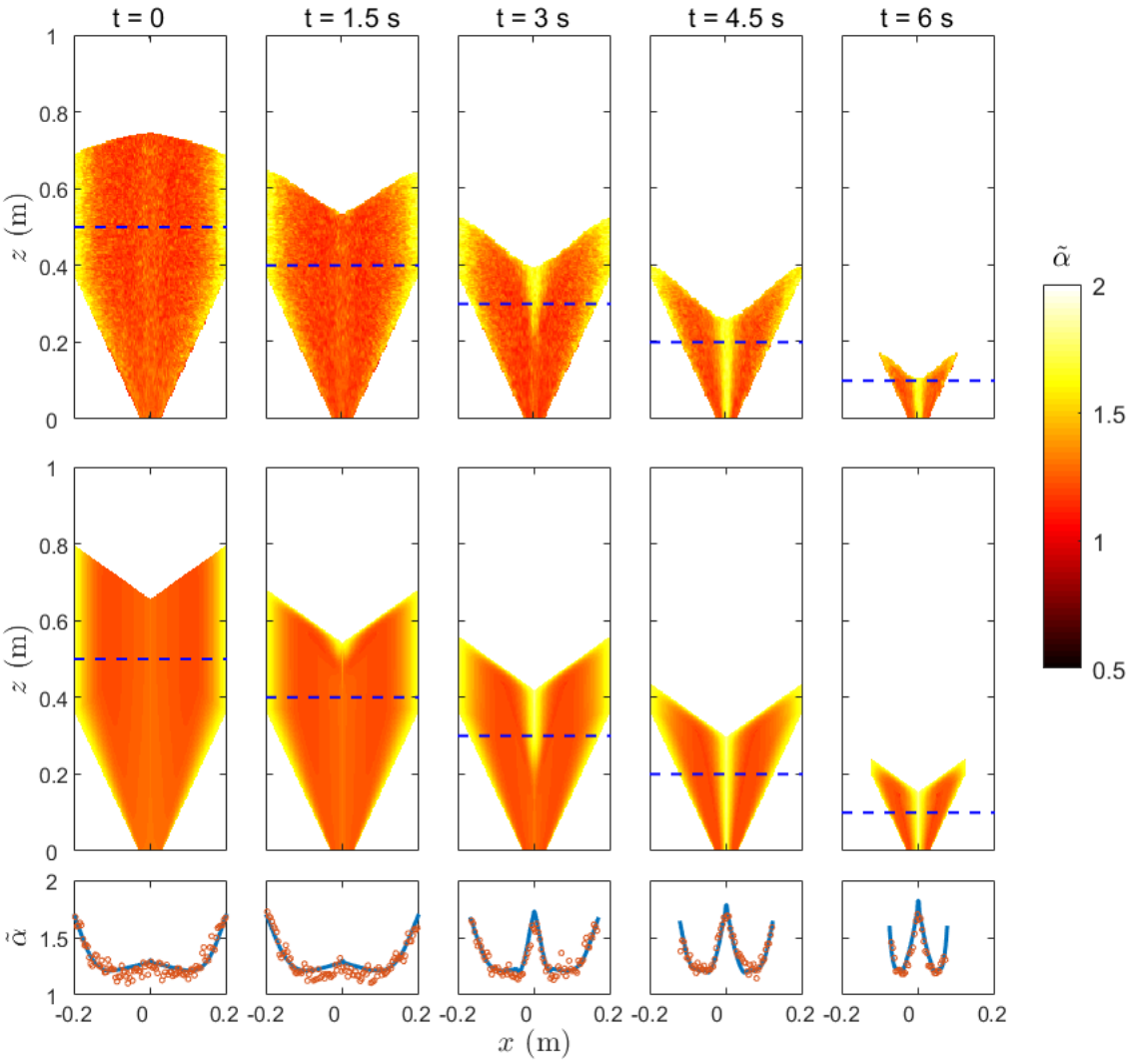

Figure 5.5. Comparison of segregation in hopper discharge flow between DEM simulations and model predictions for a segregated initial condition hopper with $W = 0.4$ m, $W_o = 0.06$ m, $\beta = 65°$, $H_v + H_c = 0.8$ m at different stages of hopper discharge for a truncated log-normal size distribution with mean $\ln(\tilde{\alpha}) = 0.27$, $\sigma = 0.3$ and $0.5 \leq \tilde{\alpha} \leq 2$. Average particle radius, $\bar{\alpha}$, from (top row) DEM simulations and (middle row) continuum model at different times from the start of the outlet flow. (bottom row) Profile of average particle radius, $\bar{\alpha}$, at different depths (blue dashed line) from DEM simulations (symbols) and model predictions (curve).

from the converging portion of the hopper, but at later times large particles from the remainder of the bulk region dominate the discharge ($t = 4.5, 6$ s)

The middle row of figure 5.5 shows a time series of average particle diameter patterns in the hopper from the model for an initially segregated condition corresponding to the DEM simulation at $t = 0$ in the top row of the figure, except with a V-shaped surface. The model matches the simulation quite well at all times. The model starts with a V-shaped surface that has a repose angle matching the angle of the V-shaped discharge region in the DEM simulations. When the discharge begins, the continuum model captures the segregation occurring in the surface layer, where large particles segregate toward the free surface ($t = 3$ s). The segregated large particles from the left and right sides meet at the the center of the V-shaped surface and are then transported by the bulk flow toward the outlet. At the same time, small particles at the bottom of the flowing layer also enter the bulk flow, but slightly upstream of the large particles at the centerline. The result is a segregation pattern where small particle enriched regions surround the central region of mostly large particles ($t = 3$ s and $t = 4.5$ s). Segregation in the model prediction occurs slightly earlier than in the DEM simulation, because the initial transition from the heap free surface to the V-shape is ignored in the continuum model. This is most evident in comparisons at $t = 1.5$ s. However, because the transition time is short, the segregation predicted by the model still agrees well with the DEM simulation.

The bottom row of figure 5.5 further compares the average particle diameter at different depths in the hopper marked by the blue dashed lines in DEM simulations and in continuum model predictions at different stages of the hopper discharge process. Early in the hopper discharge process ($t = 0, 1.5$ s), the segregated particles at the free surface

are above the measurement depth (blue dashed lines). Consequently, the average diameter profiles from DEM simulations (open circles) and continuum model (solid curve) are those resulting from the initial segregation pattern introduced during the hopper filling process. Large particles are mostly concentrated near the side walls, and small particles are concentrated near the hopper center. As the discharge continues, large particles that were initially deposited close to the sidewalls enter the flowing layer, segregate upward toward the free surface, deposit along the centerline of the hopper, and are transported by the bulk flow into the hopper bed. This is evident as a peak in average diameter at the center of the hopper both in the DEM simulations and the continuum model at later stages of the discharge ($t \geq 3$ s). It is clear that the continuum model predictions agree quite well with DEM simulation at different depths of the hopper bed.

Because segregation mainly occurs in the free surface flowing layer, it is again worthwhile to examine segregation in the flowing layer between the continuum model and the DEM simulation. Figure 5.6 compares DEM simulation and the corresponding continuum model for the left half of the hopper. The agreement between DEM simulation and model prediction is quite good throughout the flowing layer. Large particles (light color) that are deposited near sidewall (left side) during hopper filling enter the flowing layer, segregate upward to the free surface, and then flow over the small particles to deposit near the hopper center (right side). Small particles that enter the flowing layer on the left side, but to the right of the large particles, are not carried as far down the flowing layer before depositing on the bulk. Figure 5.6(c) further compares the average diameter, $\bar{\alpha}$, on the bottom of the flowing layer ($\tilde{z} = -1$) from DEM simulation and the corresponding continuum model prediction. The average size of the particles on the bottom

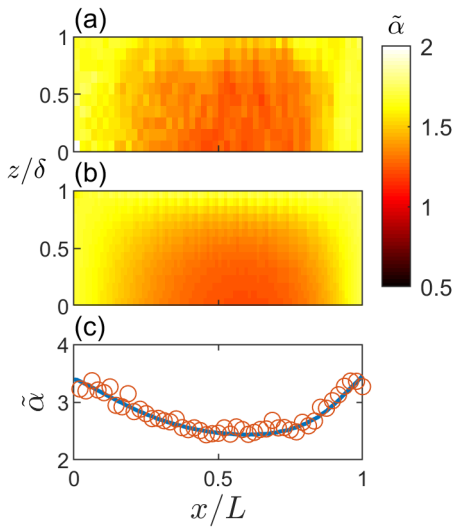

Figure 5.6. Comparison of (a) DEM simulation and (b) continuum model prediction for the average diameter $\bar{\alpha}$ in the flowing layer at $t = 2.4$ s starting from an initially segregated condition with $W = 0.4$ m, $W_o = 0.06$ m, $\beta = 65°$, $H_v + H_c = 0.84$ m. Log normal size distribution with mean $\ln(\tilde{\alpha}) = 0.27$ and $\sigma = 0.3$ for $0.5 \leq \tilde{\alpha} \leq 2$. (c) Comparison of average diameter comparison at the bottom of the flowing layer between continuum model prediction (solid curve) and DEM simulation (open circles).

of the flowing layer predicted by the model matches the DEM simulation results well. That is, the particles entering the flowing layer from the bulk (red arrow and dashed lines in figure 5.3) consist of the largest particles near the sidewalls and smaller particles to their right. The particles entering the bulk at the downstream end of the flowing layer (blue arrow and dashed lines in figure 5.3) consist of smaller particles upstream and larger particles downstream. Accounting for both sides of the V-shaped surface, this results in small particle rich regions surrounding the center region of large particles, as is evident for $t \geq 3$ s.

In addition to comparing the mean particle diameter at different locations within the hopper, we also compare the discharge profiles between the continuum model and DEM

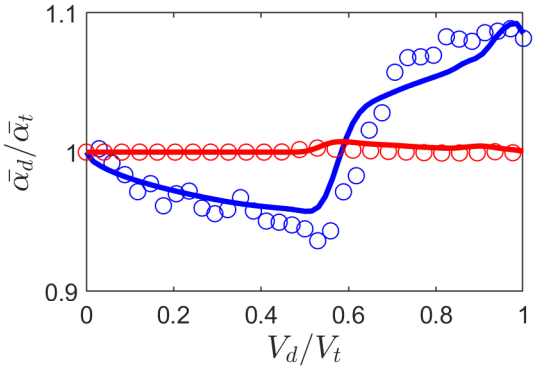

Figure 5.7. Comparison of average diameter of particle discharge between continuum model predictions (curves) and DEM simulation results (circles) starting from an initially well-mixed hopper (red) and an initially segregated hopper (blue).

simulation results in figure 5.7. The instantaneous average particle diameter discharged from the hopper, $\bar{\alpha}_d$, is normalized by the volume average initial particle diameter in the entire hopper, $\bar{\alpha}_t$. Thus, $\bar{\alpha}_d/\bar{\alpha}_t = 1$ indicates near perfectly mixed particles, $\bar{\alpha}_d/\bar{\alpha}_t > 1$ indicates more large particles than the average initial particle distribution, and $\bar{\alpha}_d/\bar{\alpha}_t < 1$ indicates more small particles than the average initial particle distribution. The volume of the discharged material, V_d, is normalized by V_t, the total volume of material initially in the hopper. For the initially well-mixed hopper, the particles remains well-mixed ($\bar{\alpha}_d/\bar{\alpha}_t \approx 1$) throughout the entire discharge process according to both the continuum model and DEM simulations, consistent with previous studies on bidisperse hopper flow with similar geometries [57, 58, 85, 115]. For the initially segregated case, the segregation at the discharge is much more significant. After discharge begins, the small particles initially concentrated in the hopper center (due to filling segregation) are discharged first, resulting in a lower average diameter in the discharge profile. When the front of the large particle region at the center of the hopper reaches the hopper outlet, large particles

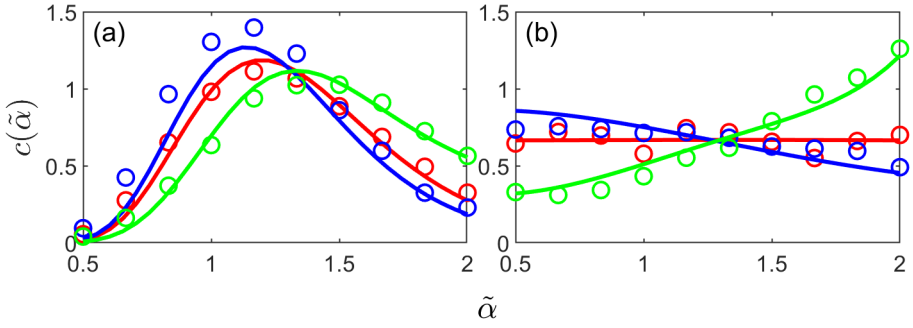

Figure 5.8. Comparison of discharged particle size distributions between DEM simulations (circles) and model predictions (curves) for an initially segregated hopper discharge with the same flow geometry in figure 5.1. (a) Log-normal and (b) uniform particle size distributions. Discharged particle probability density distribution at initial ($V_\mathrm{d}/V_\mathrm{t} = 0$) (red), middle ($V_\mathrm{d}/V_\mathrm{t} = 0.5$) (blue), and final ($V_\mathrm{d}/V_\mathrm{t} = 1$) (green) stages of hopper emptying.

dominate the discharge profile, resulting in an increase in average particle diameter in the discharge profile. The transition point predicted by the continuum model leads that for the DEM simulation because the continuum model starts with a V-shape and ignores the transition in the DEM simulation of the surface from a heap to a V-shape. However, this only affects the transition time slightly, and the continuum model still predicts the average radius at the outlet after the transition reasonably well. Overall, the continuum model prediction of the mean particle diameter at discharge agrees well with the DEM simulation results.

Additionally, it is also possible and instructive to quantitatively compare the discharged particle size distributions, $c(\tilde{\alpha})$, between the continuum model and DEM simulation results at different times during discharge. Figure 5.8 shows the model and simulation results for two different particle size distributions starting from a segregated initial condition during hopper discharge at the beginning ($V_\mathrm{d}/V_\mathrm{t} = 0$), middle ($V_\mathrm{d}/V_\mathrm{t} = 0.5$), and end

($V_d/V_t = 1$) stages of hopper discharge. We consider the log-normal particle distribution shown in figure 5.8(a) first. As the hopper discharge begins, the well-mixed particles at the bottom the hopper are discharged first, resulting in a log-normal particle size distribution corresponding to the initial particle distribution. As the discharge process continues, small particles on the hopper center dominate the discharge as is evident in figure 5.5 at $t = 3$ s, resulting in an increase in small particles and a decrease in large particles that shifts the distribution leftward. When the front of the large particle concentrated region reach the outlet, the large particles become more predominant, causing a decrease in small particles and an increase in large particles shifting the distribution rightward. The variation in the particle size distribution with time is even more evident for a uniform particle size distribution between 1 mm and 4 mm, shown in figure 5.8(b). In this case, the distribution starts flat but shifts toward smaller particles in the middle of the discharge. By the end of the discharge, large particles become predominant. These particle distribution patterns are consistent with the trend observed from particle discharge profiles in figure 5.7. It is also important to note that the model predictions match the DEM simulation results quite well, indicating the continuum model faithfully represents the segregation that occurs.

5.4. Experimental validation

Up to this point, we have demonstrated quantitative agreement between DEM simulation and continuum model predictions of size segregation despite several simplifying assumptions. To further validate the continuum model, we conduct experiments in a quasi-2D hopper that consists of a glass front wall, an aluminum back wall, and acrylic

Table 5.1. Size range for each particle species used to create quasi-polydisperse mixture

Color	Size range (mm)
black	$1.0 \leq \alpha \leq 1.3$
green	$1.3 \leq \alpha \leq 1.7$
blue	$1.7 \leq \alpha \leq 2.1$
silver	$2.4 \leq \alpha \leq 2.9$
yellow	$2.9 \leq \alpha \leq 3.4$
brown	$3.4 \leq \alpha \leq 4.0$

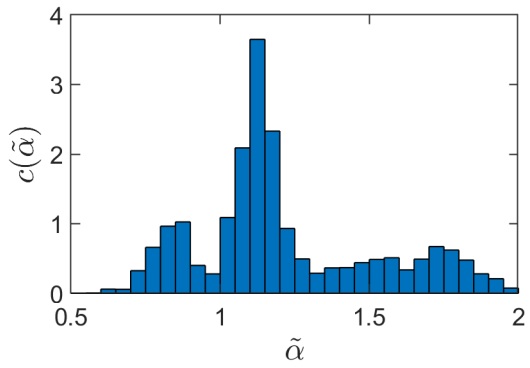

Figure 5.9. Polydisperse particle size distribution used in the experiment.

sidewalls using spherical glass particles (Deco glass beads by Ceroglass Technologies Inc., TN). We create a polydisperse particle distribution using various volumes of specified particle species nominal particle diameters ranging from 1 mm to 4 mm. Details of each particle species size range and color are provided in table 5.1. The final polydisperse particle mixture size distribution is characterized from optical images of particle samples using the scientific image analysis software, ImageJ [87]. The experimental polydisperse distribution shown in figure 5.9 is used as the input for the continuum model for the model calculation.

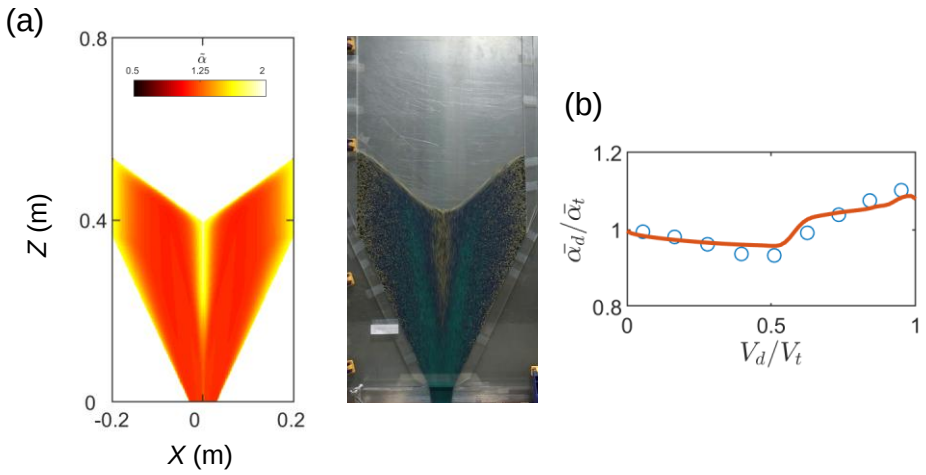

Figure 5.10. Comparison of discharged particle size distributions between model prediction and experiment with for hopper discharge started with an initially segregated condition and fed with $q = 16$ cm^2/s for hopper filling (a) segregation predicted by continuum model (left) and experimental results of corresponding hopper filling (right) (b) Comparison of discharged particle average diameter between continuum model predictions (curves) and experimental results (circles).

In the experiments, a well-mixed polydisperse particle mixtures is center-fed into the hopper by an auger feeder (101-1-DD/2, Acrison, Inc., NJ, USA) at a constant feed rate q with the hopper outlet closed. A quasi-2D let-down tube consisting of two vertical bars at the feed zone on the heap surface is raised at the heap rise velocity to minimize particle bouncing. After filling the hopper, the material is discharged onto a belt conveyor that is positioned under the hopper outlet. The conveyor belt moves at a constant speed to preserve the sequence of discharged materials, but it has no influence on the flow inside the hopper. After the discharge is completed, the material on the belt is divided into nine approximately equal samples, and the mean radius of discharged particles is measured by sifting particle mixtures using different mesh sizes to calculate the volume fraction of each monodisperse species. The segregation pattern based on the continuum model

and the corresponding experiment at the same instant are shown in figure 5.10(a). The segregation pattern consists of a region of large particles that are concentrated near the hopper periphery upon filling and second region of large particles at the centerline forming as particles flow out of the hopper during discharge, much like DEM simulations shown in figure 5.5. The segregation pattern in the experiments is well captured by the continuum model. Figure 5.10(b) also shows a good agreement for the discharge profiles between that predicted from the continuum model and the experimental results. The trend is similar to that in figure 5.7. That is, small particles exit the hopper first followed by large particles toward the ned of the discharge. The transition occurs around $V_d/V_t \approx 0.5$. Overall, the model result matches experimental data reasonably well, demonstrating the potential for the model to predict hopper segregation during filling and discharge.

5.5. Conclusions

In this chapter, a polydisperse continuum segregation model is applied to quantitatively predict the polydisperse size segregation in quasi-2D hopper discharge flow. The model accurately predicts the segregation patterns inside the hopper and the discharge segregation profiles for both initially well-mixed and segregated conditions resulted from center filling. The agreement between experiment and continuum model further corroborates the modeling approach.

However, challenges remain to be addressed in future work. For example, we have not yet extended the continuum model to 3D hoppers (cylindrical and wedge shaped), which could have significantly different flow kinematics. For example, the flowing layer thickness in a 3D hopper could be much larger than the flowing layer thickness in a quasi-2D hopper

due to the minimal influence of wall friction [56]. Additionally, for certain flow regimes, the free surface of a 3D hopper remains relatively flat until materials enter the converging portion of the hopper. However, these flow kinematics could be easily incorporated into the segregation model once the flow kinematics are fully understood. Additionally, we have not considered the coupling between the continuum segregation model presented here and predicative models for the flow proposed in previous studies [83, 84, 39, 23, 7]. These extensions will further advance model development toward a general framework for modeling particle segregation in many different flows.

CHAPTER 6

Summary and future work

In this chapter, the major conclusions from this dissertation are summarized. Additionally, future research work directions that could be built on top of these conclusions are outlined.

6.1. Summary

This dissertation focuses on extending the application of the modified continuum model for bidisperse segregation that captures the effects of segregation, diffusion, and advection to polydisperse (continuous distribution of particle size) segregating materials and to unsteady flow (time-dependent flow kinematics).

• The continuum transport model for bidisperse size segregation was first extended to describe tridisperse size segregation in a developing chute flow, which is an important stepping stone between bidisperse and polydisperse segregation. The model uses the kinematics of the flow and other physical parameters such as the diffusion coefficient and the percolation length scale, quantities that can be determined directly from experiment, simulation or theory and that are not arbitrarily adjustable. The approach also introduced a characteristic streamwise length scale related to the relative strengths of segregation for the smallest and largest particles. The model was validated against DEM simulations over a wide range of chute geometries and flow conditions. Additionally, a parametric study on quasi-2D chute flow was done in terms of Pe, κ_{ij}, and L to demonstrate how particle

segregation patterns depend on the interplay of advection, segregation, and diffusion. The model also makes possible the study of how the segregation is affected by the velocity profile and slip at the surface of the chute.

• The transport model for multidisperse segregation was then extended to describe polydisperse segregation in steady flow including developing flow (bounded heap) and transient flow (rotating tumbler). This requires the solution of the continuum transport model with an integral to account for the dependence of the percolation length scale on the local species concentration. Additionally, the polydisperse approach was applied to density polydisperse materials with the same particle size. Predictions of the model agree quantitatively with experimentally validated DEM simulations of both size polydisperse and density polydisperse mixtures over a range of particle distributions and flow conditions. This is particularly remarkable given the simplifying assumptions in the model and that the segregation parameters are based on bidisperse mixtures.

• To demonstrate the applications of the continuum transport model to unsteady flow, we also showed that the model can be adapted to account for the modulated heap flow, in which the flow kinematics are inherently unsteady due to the time-varying feed rate. The predictions of the model are consistent with experimental results and provide physical insight into the stratification that occur in such flows. Using a modulated feed rate as a method to create and control extended layers of granular materials could potentially enhance the effective mixing of deposited materials by layering small and large particles rather than having all small particles deposited upstream of the large particles.

• The transport equation approach was further extended to describe size segregation of polydisperse granular particles in a hopper flow, which has wide industrial applications in

solids processing. This required combining the polydisperse segregation model of Chapter 2 with the kinematics of filling and emptying a hopper. Model results consistent with DEM simulations and experiments were obtained. Although the continuum transport model was applied to a quasi-2D hopper, it could be extended to a fully 3D hopper.

6.2. Future work

Using continuum approach to understand and model granular flow remains to be a tremendously rich area. There are many improvements that can be further explored based on work presented in this thesis. For example, we have not studied the interplay between simultaneous density and size effects, which have been shown to be a counter mechanism for size segregation [48, 49, 30]. The approach should be applicable to this case, provided that the relations are known for dependence of the segregation velocity on the particle dispersity and for the dependence of diffusion on the kinematics of the flow. These relations could be determined either through DEM simulations or experiments, following the similar approach by Schlick et al. [89]. Additionally, we have not yet considered the coupling between flow kinematics models, such as the $\mu(I)$ rheology [83, 84, 39, 23, 7], and our transport continuum model, or the possibility of interplay between the segregation and kinematics, which is minimal in the cases studied here but can be significant in other situations.

Moreover, most of the flow geometries considered in this thesis are quasi-2D, which are idealized versions of 3D flows. It would be worthwhile to extend the continuum transport model for segregation to 3D flow geometries such as 3D conical hopper flow, 3D wedge hopper flow, and V-shaped blender flow. It may even be possible to extend the model to

situations in a blade passes through a granular medium as is the case in bladed particle blenders and the agricultural application of plowing. Applying this model to these 3D geometries could provide insights into the segregation mechanism in these geometries and yield practical guidance for design and operation of granular materials handling systems in a wide range of applications. These extensions will further enhance the current model and advance it toward a general framework for modeling particle segregation in many different flow situations.

References

[1] *Discrete Element Modeling and Simulation Laboratory (DEMSLab).* URL `http://www.demslab.com`.

[2] A. Alexander, T. Shinbrot, and F. J. Muzzio. Scaling surface velocities in rotating cylinders as a function of vessel radius, rotation rate, and particle size. *Powder Technol*, 126(2):174 – 190, 2002.

[3] C. Ancey. Dry granular flows down an inclined channel: experimental investigations on the frictional-collisional regime. *Phys Rev E*, 65:011304, 2001.

[4] I. S. Aranson and L. S. Tsimring. Patterns and collective behavior in granular media: Theoretical concepts. *Rev Mod Phys*, 78:641–692, 2006.

[5] P. Artega and U. Tzn. Flow of binary mixtures of equal-density granules in hopperssize segregation, flowing density and discharge rates. *Chem Eng Sci*, 45(1):205 – 223, 1990.

[6] R. Bagnold. Experiments on a gravity-free dispersion of large solid spheres in a newtonian fluid under shear. *Proc R Soc A*, 225(1160):49–63, 1954.

[7] J. Baker, T. Barker, and J. M. N. T. Gray. A two-dimensional depth-averaged $\mu(I)$ rheology for dense granular avalanches. *J Fluid Mech*, 787:367–395, 2016.

[8] R. Besseling, E. R. Weeks, A. B. Schofield, and W. C. K. Poon. Three-dimensional imaging of colloidal glasses under steady shear. *Phys Rev Lett*, 99(2):028301, 2007.

[9] T. Bhattacharya and J. J. McCarthy. Chute flow as a means of segregation characterization. *Powder Technol*, 256:126–139, 2014.

[10] W. Bi, R. Delannay, P. Richard, and A. Valance. Experimental study of two-dimensional, monodisperse, frictional-collisional granular flows down an inclined chute. *Phys Fluids*, 18:123302, 2006.

[11] D. Bonamy, F. Daviaud, and L. Laurent. Experimental study of granular surface flows via a fast camera: A continuous description. *Phys Fluids*, 14(5):1666–1673, 2002.

[12] G. E. P. Box and M. E. Muller. A note on the generation of random normal deviates. *Ann Math Statist*, 29(2):610–611, 1958.

[13] J. Bridgwater, W. S. Foo, and D. J. Stephens. Particle mixing and segregation in failure zonestheory and experiment. *Powder Technol*, 41(2):147 – 158, 1985.

[14] P. Chen, J. M. Ottino, and R. M. Lueptow. Subsurface granular flow in rotating tumblers: A detailed computational study. *Phys Rev E*, 78(2):021303, 2008.

[15] J. Choi, A. Kudrolli, and M. Z. Bazant. Velocity profile of granular flows inside silos and hoppers. *J Phys Condens Mat*, 17(24):S2533, 2005.

[16] S. L. Conway, A. Lekhal, J. G. Khinast, and B. J. Glasser. Granular flow and segregation in a four-bladed mixer. *Chem Eng Sci*, 60(24):7091–7107, 2005.

[17] A. Cromer. Stable solutions using the euler approximation. *Am J Phys*, 49(5): 455–459, 1981.

[18] P. G. de Gennes. Granular matter: a tentative view. *Rev Mod Phys*, 71(2):S374–S382, 1999.

[19] Z. Deng, P. B. Umbanhowar, J. M. Ottino, and R. M. Lueptow. Continuum modelling of segregating tridisperse granular chute flow. *Proc R Soc A*, 474(2211), 2018.

[20] Z. Deng, P. B. Umbanhowar, J. M. Ottino, and R. M. Lueptow. Modeling segregation of polydisperse granular materials in developing and transient free-surface flows. *AIChE J*, 65(3):882–893, 2019.

[21] V. N. Dolgunin and A. A. Ukolov. Segregation modeling of particle rapid gravity flow. *Powder Technol*, 83(2):95–103, 1995.

[22] V. N. Dolgunin, A. N. Kudy, and A. A. Ukolov. Development of the model of segregation of particles undergoing granular flow down an inclined chute. *Powder Technol*, 96:211–218, 1998.

[23] A. Edwards and J. M. N. T. Gray. Erosion deposition waves in shallow granular free-surface flows. *J Fluid Mech*, 762:35–67, 2015.

[24] Y. Fan and K. M. Hill. Theory for shear-induced segregation of dense granular mixtures. *New J Phys*, 13:095009, 2011.

[25] Y. Fan, Y. Boukerkour, T. Blanc, P. B. Umbanhowar, J. M. Ottino, and R. M. Lueptow. Stratification, segregation, and mixing of granular materials in quasi-two-dimensional bounded heaps. *Phys Rev E*, 86:051305, 2012.

[26] Y. Fan, P. B. Umbanhowar, J. M. Ottino, and R. M. Lueptow. Kinematics of monodisperse and bidisperse granular flows in quasi-two-dimensional bounded heaps. *Proc R Soc A*, 469:20130235, 2013.

[27] Y. Fan, C. P. Schlick, P. B. Umbanhowar, J. M. Ottino, and R. M. Lueptow. Modelling size segregation of granular materials: the roles of segregation, advection and diffusion. *J Fluid Mech*, 741:252–279, 2014.

[28] Y. Fan, P. B. Umbanhowar, J. M. Ottino, and R. M. Lueptow. Shear-rate-independent diffusion in granular flows. *Phys Rev Lett*, 115:088001, 2015.

[29] S. J. Fiedor and J. M. Ottino. Mixing and segregation of granular matter: multi-lobe formation in time-periodic flows. *J Fluid Mech*, 533:223–236, 2005.

[30] G. Flix and N. Thomas. Evidence of two effects in the size segregation process in a dry granular media. *Phys Rev E*, 70:051307, 2004.

[31] A. M. Fry, P. B. Umbanhowar, J. M. Ottino, and R. M. Lueptow. Effect of pressure on segregation in granular shear flows. *Phys Rev E*, 97:062906, 2018.

[32] P. Gajjar and J. M. N. T. Gray. Asymmetric flux models for particle-size segregation in granular avalanches. *J Fluid Mech*, 757:297–329, 2014.

[33] C. Geuzaine and J. F. Remacle. Gmsh: A 3-d finite element mesh generator with built-in pre- and post-processing facilities. *Int J Numer Meth Eng*, 79(11):1309–1331, 2009.

[34] L. A. Golick and K. E. Daniels. Mixing and segregation rates in sheared granular materials. *Phys Rev E*, 80:042301, 2009.

[35] J. M. N. T. Gray and C. Ancey. Segregation, recirculation and deposition of coarse particles near two-dimensional avalanche fronts. *J Fluid Mech*, 629:387423, 2009.

[36] J. M. N. T. Gray and C. Ancey. Multi-component particle-size segregation in shallow granular avalanches. *J Fluid Mech*, 678:535–588, 2011.

[37] J. M. N. T. Gray and C. Ancey. Particle-size and -density segregation in granular free-surface flows. *J Fluid Mech*, 779:622668, 2015.

[38] J. M. N. T. Gray and V. A. Chugunov. Particle-size segregation and diffusive remixing in shallow granular avalanches. *J Fluid Mech*, 569:365–398, 2006.

[39] J. M. N. T. Gray and A. Edwards. A depth-averaged $\mu(I)$ rheology for shallow granular free-surface flows. *J Fluid Mech*, 755:503–534, 2014.

[40] J. M. N. T. Gray and K. Hutter. Pattern formation in granular avalanches. *Continuum Mech Therm*, 9(6):341–45, 1997.

[41] J. M. N. T. Gray and A. R. Thornton. A theory for particle size segregation in shallow granular free-surface flows. *Proc R Soc A*, 461:1447–1473, 2005.

[42] J. M. N. T. Gray, M. Shearer, and A. R. Thornton. Time-dependent solutions for particle-size segregation in shallow granular avalanches. *Proc R Soc A*, 462:947–972, 2006.

[43] J. E. Guyer, D. Wheeler, and J. A. Warren. Fipy: Partial differential equations with python. *Comput Sci Eng*, 11(3):6–15, 2009.

[44] D. B. Hastie and P. W. Wypych. Segregation during gravity filling of storage bins. In *IUTAM Symposium on Segregation in Granular Flows*, pages 61–72. Springer, 2000.

[45] H. M. Jaeger, S. R. Nagel, and R. P. Behringer. Granular solids, liquids, and gases. *Rev Mod Phys*, 68(4):1259–1273, 1996.

[46] A. Jain, M. J. Metzger, and B. J. Glasser. Effect of particle size distribution on segregation in vibrated systems. *Powder Technol*, 237:543–553, 2013.

[47] N. Jain, J. M. Ottino, and R. M. Lueptow. An experimental study of the flowing granular layer in a rotating tumbler. *Phys Fluids*, 14(2):572–582, 2002.

[48] N. Jain, J. M. Ottino, and R. M. Lueptow. Regimes of segregation and mixing in combined size and density granular systems: an experimental study. *Granular Matter*, 7(2):69–81, 2005.

[49] N. Jain, J. M. Ottino, and R. M. Lueptow. Combined size and density segregation and mixing in noncircular tumblers. *Phys Rev E*, 71(5):051301, 2005.

[50] G. Jasion, J. Shrimpton, M. Danby, and K. Takeda. Performance of numerical integrators on tangential motion of dem within implicit flow solvers. *Chem Eng Sci*, 35(11):2218 – 2226, 2011.

[51] A. W. Jenike. Storage and flow of solids. *Bulletin No. 123, Utah State University*, 1964.

[52] L. Jing, C. Y. Kwok, Y. F. Leung, and Y. D. Sobral. Characterization of base roughness for granular chute flows. *Phys Rev E*, 94:052901, 2016.

[53] L. Jing, C. Y. Kwok, and Y. F. Leung. Micromechanical origin of particle size segregation. *Phys Rev Lett*, 118:118001, 2017.

[54] L. Jing, C. Y. Kwok, Y. F. Leung, and Y. D. Sobral. Effect of geometric base roughness on size segregation. *EPJ Web Conf.*, 140:03056, 2017.

[55] R. P. Jones, A. B. Isner, Xiao. H., J. M. Ottino, P. B. Umbanhowar, and R. M. Lueptow. Asymmetric concentration dependence of segregation fluxes in granular flows. *Phys Rev Fluids*, 3:094304, 2018.

[56] P. Jop, Y. Forterre, and O. Pouliquen. Crucial role of sidewalls in granular surface flows: consequences for the rheology. *J Fluid Mech*, 541:167–192, 2005.

[57] W. R. Ketterhagen, J. S. Curtis, C. R. Wassgren, A. Kong, P. J. Narayan, and B. C. Hancock. Granular segregation in discharging cylindrical hoppers: a discrete element and experimental study. *Chem Eng Sci*, 62(22):6423–6439, 2007.

[58] W. R. Ketterhagen, J. S. Curtis, C. R. Wassgren, and B. C. Hancock. Modeling granular segregation in flow from quasi-three-dimensional, wedge-shaped hoppers.

Powder Technol, 179(3):126–143, 2008.

[59] W. R. Ketterhagen, J. S. Curtis, C. R. Wassgren, and B. C. Hancock. Predicting the flow mode from hoppers using the discrete element method. *Powder Technol*, 195(1):1–10, 2009.

[60] D. V. Khakhar, J. J. McCarthy, T. Shinbrot, and J. M. Ottino. Transverse flow and mixing of granular materials in a rotating cylinder. *Phys Fluids*, 9(1):31–43, 1997.

[61] M. H. Kimberly and Y. Fan. Granular temperature and segregation in dense sheared particulate mixtures. *KONA Powder Part J*, 33:150–168, 2016.

[62] T. S. Komatsu, S. Inagaki, N. Nakagawa, and S. Nasuno. Creep motion in a granular pile exhibiting steady surface flow. *Phys Rev Lett*, 86(9):1757–1760, 2001.

[63] J. Kowalski and J. N. McElwaine. Shallow two-component gravity-driven flows with vertical variation. *J Fluid Mech*, 714:434462, 2013.

[64] M. Larcher and J. T. Jenkins. Segregation and mixture profiles in dense, inclined flows of two types of spheres. *Phys Fluids*, 25:113301, 2013.

[65] M. Larcher and J. T. Jenkins. The evolution of segregation in dense inclined flows of binary mixtures of spheres. *J Fluid Mech*, 782:405–429, 2015.

[66] F. Lominé and L. Oger. Dispersion of particles by spontaneous interparticle percolation through unconsolidated porous media. *Phys Rev E*, 79:051307, 2009.

[67] M. Y. Louge and S. C. Keast. On dense granular flows down flat frictional inclines. *Phys Fluids*, 13(5):1213–1233, 2001.

[68] R. M. Lueptow, Z. Deng, H. Xiao, and P. B. Umbanhowar. Modeling segregation in modulated granular flow. *EPJ Web Conf*, 140:03018, 2017.

[69] H. Makse. Continuous avalanche segregation of granular mixtures in thin rotating drums. *Phys Rev Lett*, 83:3186–3189, 1999.

[70] H. A. Makse, S. Havlin, P. R. King, and H. E. Stanley. Spontaneous stratification in granular mixtures. *Nature*, 386(6623):379–382, 1997.

[71] B. Marks and I. Einav. A mixture of crushing and segregation: The complexity of grainsize in natural granular flows. *Geophys Res Lett*, 42(2):274–281, 2015.

[72] B. Marks, P. Rognon, and I. Einav. Grainsize dynamics of polydisperse granular segregation down inclined planes. *J Fluid Mech*, 690:499–511, 2012.

[73] L. B. May, L. A. Golick, K. C. Phillips, M. Shearer, and K. E. Daniels. Shear-driven size segregation of granular materials: modeling and experiment. *Phys Rev E*, 81: 051301, 2010.

[74] S. W. Meier, R. M. Lueptow, and J. M. Ottino. A dynamical systems approach to mixing and segregation of granular materials in tumblers. *Adv Phys*, 56(5):757–827, 2007.

[75] J. Mellmann. The transverse motion of solids in rotating cylindersforms of motion and transition behavior. *Powder Technol*, 118(3):251–270, 2001.

[76] GDR MiDi. On dense granular flows. *Eur Phys J E*, 14:341–65, 2004.

[77] B. K Mishra. A review of computer simulation of tumbling mills by the discrete element method: Part I - contact mechanics. *Int J Miner Process*, 71(1):73 – 93, 2003.

[78] R. M. Nedderman and U. Tüzün. A kinematic model for the flow of granular materials. *Powder Technol*, 22(2):243–253, 1979.

[79] R. M. Nedderman, U. Tüzün, S. B. Savage, and G. T. Houlsby. The flow of granular materialsi: Discharge rates from hoppers. *Chem Eng Sci*, 37(11):1597–1609, 1982.

[80] M. Newey, J. Ozik, S. M. van der Meer, E. Ott, and W. Losert. Band-in-band segregation of multidisperse granular mixtures. *Europhys Lett*, 66(2):205, 2004.

[81] A. V. Orpe and D. V. Khakhar. Scaling relations for granular flow in quasi-two-dimensional rotating cylinders. *Phys Rev E*, 64:031302, 2001.

[82] G. G. Pereira and P. W. Cleary. Radial segregation of multi-component granular media in a rotating tumbler. *Granular Matter*, 15(6):705–724, 2013.

[83] O. Pouliquen. Scaling laws in granular flows down rough inclined planes. *Phys Fluids*, 11:542–548, 1999.

[84] O. Pouliquen and Y. Forterre. Friction law for dense granular flows: application to the motion of a mass down a rough inclined plane. *J Fluid Mech*, 453:133–151, 2002.

[85] A. Samadani, A. Pradhan, and A. Kudrolli. Size segregation of granular matter in silo discharges. *Phys Rev E*, 60(6):7203, 1999.

[86] S. B. Savage and C. K. K. Lun. Particle-size segregation in inclined chute flow of dry cohesionless granular solids. *J Fluid Mech*, 189:311–335, 1988.

[87] A. Scheider, C, W. S. Rasband, and K. W. Eliceiri. Nih image to imagej: 25 years of image analysis. *Nature Methods*, 9:671–675, 2012.

[88] C. P. Schlick, I. C. Christov, P. B. Umbanhowar, J. M. Ottino, and R. M. Lueptow. A mapping method for distributive mixing with diffusion: Interplay between chaos and diffusion in time-periodic sine flow. *Phys Fluids*, 25(5):052102, 2013.

[89] C. P. Schlick, Y. Fan, A. B. Isner, P. B. Umbanhowar, J. M. Ottino, and R. M. Lueptow. Modeling segregation of bidisperse granular materials using physical control parameters in the quasi-2d bounded heap. *AIChE J*, 61:1524–1534, 2015.

[90] C. P. Schlick, Y. Fan, P. B. Umbanhowar, J. M. Ottino, and R. M. Lueptow. Granular segregation in circular tumblers: theoretical model and scaling laws. *J Fluid Mech*, 765:632–652, 2015.

[91] C. P. Schlick, A. B. Isner, B. J. Freireich, Y. Fan, P. B. Umbanhowar, J. M. Ottino, and R. M. Lueptow. A continuum approach for predicting segregation in flowing polydisperse granular materials. *J Fluid Mech*, 797:95–109, 2016.

[92] A. M. Scott and J. Bridgwater. Interparticle percolation: A fundamental solids mixing mechanism. *Ind Eng Chem Fundam*, 14(1):22–27, 1975.

[93] J. Shäfer, S. Dippel, and D. E. Wolf. Force schemes in simulations of granular materials. *J Phys I France*, 6(1):5–20, 1996.

[94] L. E. Silbert, D. Ertas, G. S. Grest, T. C. Halsey, D. Levine, and S. J. Plimpton. Granular flow down an inclined plane: Bagnold scaling and rheology. *Phys Rev E*, 64:051302, 2001.

[95] L. E. Silbert, J. W. Landry, and G. S. Grest. Granular flow down a rough inclined plane: Transition between thin and thick piles. *Phys Fluids*, 15:1–10, 2003.

[96] M. K. Singh, O. S. Galaktionov, H. E. H. Meijer, and P. D. Anderson. A simplified approach to compute distribution matrices for the mapping method. *Comput Chem Eng*, 33(8):1354–1362, 2009.

[97] N. Standish. Studies of size segregation in filling and emptying a hopper. *Powder Technol*, 45(1):43–56, 1985.

[98] T. Takahashi. *Debris Flow*. 2014.

[99] A. Thornton, T. Weinhart, S. Luding, and O. Bokhove. Modeling of particle size segregation: Calibration using the discrete particle method. *Intl J Mod Phys C*, 23 (08):1240014, 2012.

[100] A. R. Thornton, J. M. N. T. Gray, and A. J. Hogg. A three-phase mixture theory for particle size segregation in shallow granular free-surface flows. *J Fluid Mech*, 550:1–25, 2006.

[101] J. M. Ting and B. T. Corkum. Computational laboratory for discrete element geomechanics. *J Comput Civil Eng*, 6(2):129–146, 1992.

[102] A. Tripathi and D. V. Khakhar. Density difference-driven segregation in a dense granular flow. *J Fluid Mech*, 717:643669, 2013.

[103] R. Tuley, M. Danby, J. Shrimpton, and M. Palmer. On the optimal numerical time integration for lagrangian dem within implicit flow solvers. *Chem Eng Sci*, 34(6): 886 – 899, 2010.

[104] D. R. Tunuguntla, O. Bokhove, and A. R. Thornton. A mixture theory for size and density segregation in shallow granular free-surface flows. *J Fluid Mech*, 749:99–112, 2014.

[105] D. R. Tunuguntla, A. R. Thornton, and T. Weinhart. From discrete elements to continuum fields: Extension to bidisperse systems. *Comput Part Mech*, 3:349–365, 2016.

[106] B. Utter and R. P. Behringer. Self-diffusion in dense granular shear flows. *Phys Rev E*, 69(3):031308, 2004.

[107] K. van der Vaart, P. Gajjar, G. Epely-Chauvin, N. Andreini, J. M. N. T. Gray, and C. Ancey. Underlying asymmetry within particle size segregation. *Phys Rev Lett*, 114(23):238001, 2015.

[108] O. R. Walton. Special issue on mechanics of granular materials numerical simulation of inclined chute flows of monodisperse, inelastic, frictional spheres. *Mech Mater*, 16(1):239–247, 1993.

[109] E. Wandersman, J. A. Dijksman, and M. Hecke. Particle diffusion in slow granular bulk flows. *Europhys Lett*, 100(3):38006, 2012.

[110] S. Wiederseiner, N. Andreini, G. Epely-Chauvin, G. Moser, M. Monnereau, J. M. N. T. Gray, and C. Ancey. Experimental investigation into segregating granular flows down chutes. *Phys Fluids*, 23:013301, 2011.

[111] J. C. Williams. The segregation of particulate materials. a review. *Powder Technol*, 15(2):245 – 251, 1976.

[112] H. Xiao, P. B. Umbanhowar, J. M. Ottino, and R. M. Lueptow. Modelling density segregation in flowing bidisperse granular materials. *Proc R Soc A*, 472:20150856, 2016.

[113] H. Xiao, D. McDonald, Y. Fan, P. B. Umbanhowar, J. M. Ottino, and R. M. Lueptow. Controlling granular segregation using modulated flow. *Powder Technol*, 312: 360–368, 2017.

[114] H. Xiao, J. M. Ottino, R. M. Lueptow, and P. B. Umbanhowar. Transient response in granular quasi-two-dimensional bounded heap flow. *Phys Rev E*, 96:040902, 2017.

[115] H. Xiao, Y. Fan, K. V. Jacob, P. B. Umbanhowar, M. Kodam, J. F. Koch, and R. M. Lueptow. Continuum modeling of granular segregation during hopper discharge.

Chem Eng Sci, 193:188–204, 2019.

[116] M. Yao and A. Anandarajah. Three-dimensional discrete element method of analysis of clays. *J Eng Mech*, 129(6):585–596, 2003.

[117] Y. Zhao, M. Jiang, Y. Liu, and J. Zheng. Particle-scale simulation of the flow and heat transfer behaviors in fluidized bed with immersed tube. *AIChE J*, 55(12): 3109–3124, 2009.

[118] Y. Zhao, Y. Cheng, C. Wu, Y. Ding, and Y. Jin. Eulerian-lagrangian simulation of distinct clustering phenomena and rtds in riser and downer. *Particuology*, 8(1): 44–50, 2010.

[119] Y. Zhao, H. Xiao, P. B. Umbanhowar, and R. M. Lueptow. Simulation and modeling of segregating rods in quasi-2d bounded heap flow. *AIChE J*, 64(5):1550–1563, 2017.

APPENDIX A

DEMSLab DEM Simulation details

All the simulations in the Chapter 2 and 3 are conducted using DEMSLab [1], a commercial DEM simulation software package. In DEM simulations, the translational and rotational momenta of each particle are tracked by integrating Newton's Second Law. For simplicity, a linear-spring-dashpot model for particle interaction forces is used, which, nonetheless, allows accurate simulation of ensembles of spherical glass particles for dense granular flow [117, 118]. For two contacting particles i and j, the normal force is $\boldsymbol{F}_{ij}^{n} = -k_n \boldsymbol{\delta}_{n,ij} - \eta_{n,ij} \boldsymbol{v}_{n,ij}$, and the tangential force is $\boldsymbol{F}_{ij}^{t} = -k_t \boldsymbol{\delta}_{t,ij} - \eta_{t,ij} \boldsymbol{v}_{t,ij}$. Here, k_n and k_t are the normal and tangential spring stiffnesses, respectively; $\eta_{n,ij}$ and $\eta_{t,ij}$ are the normal and tangential damping coefficients, respectively, which can be calculated using the effective mass of the two contacting particles, or a particle contacting an infinite mass wall, and the restitution coefficient [101]; $\boldsymbol{\delta}_{n,ij}$ is the normal displacement between two particles, $\boldsymbol{\delta}_{t,ij}$ is the tangential displacement which is measured by $\boldsymbol{\delta}_{t,ij} = \int_{t_0}^{t} \boldsymbol{v}_{t,ij} dt$, where t_0 is the initial contact time between two particles; and $\boldsymbol{v}_{n,ij}$ and $\boldsymbol{v}_{t,ij}$ are the relative velocities of particles in the normal and tangential direction, respectively. When the relation $|\boldsymbol{F}_{t,ij}| > \mu |\boldsymbol{F}_{n,ij}|$ is satisfied, the Coulomb friction model for sliding is used to calculate the tangential contact force as $\boldsymbol{F}_{t,ij} = -\mu |\boldsymbol{F}_{n,ij}| \boldsymbol{\delta}_{t,ij} / |\boldsymbol{\delta}_{t,ij}|$, where μ is the friction coefficient. The tangential stiffness is $k_s = (2/7)k_n$, which ensures that the normal and tangential oscillation frequencies are equal in the zero damping limit [93]. The damping

coefficients are $\eta_{n,ij} = 2|\ln e|\sqrt{k_n m_{\text{eff}}/(\pi^2 + \ln^2 e)}$ and $\eta_{t,ij} = (2/7)\eta_{n,ij}$, where $m_{\text{eff}} = m_i m_j/(m_i+m_j)$ is the effective mass of the two contacting particles or a particle contacting an infinite mass wall, and e is the restitution coefficient [101, 93]. DEM simulation parameters are listed in table A.1, see [119]. Negligible differences in segregation occur for different e, μ, and stiffness coefficients within the range of feed rates, size ratios, and density ratios tested in this specific geometry as suggested in previous study [112, 26]. The symplectic Euler integration algorithm [103, 50, 17] is used to update particle positions and velocities. The simulation time step is chosen to be smaller than the critical time step, which is one-tenth of the minimal natural oscillation period of the spring-mass system [77, 116, 117, 119]. Well mixed particle mixtures are randomly generated in a rectangular grid coordinate within the feed zone. Grid coordinates are spaced at least one large particle diameter apart to prevent particle collisions during particle generation and reduce particle segregation within the feedzone.

Table A.1. DEM Simulation parameters

Simulation parameter	Value
k_n	1400 (N/m)
k_t	400 (N/m)
ρ	2500 (kg/m^3)
μ	0.3
e	0.9

APPENDIX B

In-house GPU DEM Simulation details

All the simulations in Chapter 5 are conducted using in-house GPU DEM code [27, 90, 89, 91, 112, 115]. In GPU DEM simulations, the translational and rotational momenta of each particle are tracked by integrating Newton's Second Law. A linear-spring-dashpot model for particle interaction forces is used, which allows accurate simulation of ensembles of spherical glass particles for dense granular flow [115, 26, 27, 90, 117, 118]. For two contacting particles i and j, the normal force is $\boldsymbol{F}_{ij}^{n} = [k_n\epsilon_n - 2\eta_{n,ij}m_{\text{eff}}(\boldsymbol{V}_{ij}\cdot\hat{\boldsymbol{r}}_{ij})]\hat{\boldsymbol{r}}_{ij}$, where the overlap and relative velocity are ϵ_n and $\boldsymbol{V}_{ij}$, respectively, the unit normal vector is $\hat{\boldsymbol{r}}_{ij}$, and the effective mass is $m_{\text{eff}} = m_i m_j/(m_i + m_j)$. The restitution coefficient, e, and the binary collision time, t_c, are related to the spring stiffness and damping by $k_n = [(\pi/t_c)^2 - \gamma_n^2]m_{\text{eff}}$ and $\gamma_n = \ln(e/t_c)$. In the tangential direction, the contact force is modeled as $\boldsymbol{F}_{ij}^{t} = -\min(|k_t\epsilon_t|, |\mu\boldsymbol{F}_{ij}^{n}|)\text{sgn}(\epsilon_t)\hat{\boldsymbol{s}}$, which is a combination of a linear spring model and Coulomb sliding friction. The tangential stiffness, k_t, is determined as $k_t = \frac{2}{7}k_n$, μ is the friction coefficient, and $\hat{\boldsymbol{s}}$ is the unit vector in the tangential direction. The tangential displacement is determined as $\epsilon_t = \int_{t_s}^{t}\boldsymbol{V}_{ij}^{t}dt$, where t_s is the initial contact time, and $\boldsymbol{V}_{ij}^{t}$ is the relative tangential velocity. For particle-wall interactions, the same force models are applied, and the wall is treated as a sphere with infinite mass. For all simulations presented in this study, the binary collision time is $t_c = 10^{-4}$ s, the restitution coefficient is $e = 0.8$, and the friction coefficient is $\mu = 0.4$. The parameters have been used previous in many previous studies to accurately simulate surface flows

of glass particles [115, 26, 27, 90]. The time step is set to be $t_c/40$ to ensure numerical stability [115, 26, 27, 90]. The symplectic Euler integration algorithm [103, 50, 17] is used to update particle positions and velocities. Negligible differences in segregation occur for different e, μ, and stiffness coefficients within the range of feed rates, size ratios, and density ratios tested in this specific geometry as suggested in previous studies [112, 26]. Well-mixed particle mixtures are randomly generated in a rectangular grid coordinate within the feed zone. Box-Muller transformation method is used to generate polydisperse particle size distribution[12]. Grid coordinates are spaced at least one large particle diameter apart to prevent particle collisions during particle generation and to reduce particle segregation within the feedzone.

APPENDIX C

Diffusion coefficient

The spatio-temporal average of the diffusion coefficient, D, of the flow is calculated only in the normal direction. To do so, the time evolution of the non-affine trajectory component in the normal direction of every particle, $\Delta Z(\Delta t) = z(t_0 + \Delta t) - z(t_0) - \int_{t_0}^{t_0+\Delta t} w(t)dt$, is used to calculate the mean squared displacement in normal direction, $\langle \Delta Z(\Delta t)^2 \rangle$ [8, 109]. Here, $w(t)$ is the local mean normal velocity at time t, and $\langle * \rangle$ denotes the ensemble average. The diffusion coefficient is then calculated as the slope of the equation $\langle \Delta Z(\Delta t)^2 \rangle = 2D\Delta t$ for the range Δt where the relationship is linear (here, 0 to 0.3 s) [106].

APPENDIX D

Additional DEM simulations for tridisperse chute flow

Among the physical control parameters, the particle size ratio R, chute incline angle θ, and flow rate q have the greatest impact on the segregation [89] and bulk flow kinematics [3, 94, 76]. Figure D.1 shows a series of model predictions and simulation results for the concentration of each species at different streamwise locations for different R, θ, q, and with a simulated flowing length $l = 0.6\,\mathrm{m}$. The operating conditions for each simulation are shown in table D.1.

Though not meant to be a parametric study, figure D.1 (a) shows that there is less segregation for $R = 1 : 1.2 : 1.5$ compared to $R = 1 : 1.6 : 2.5$ in figure 2.4, even though θ and q are nearly the same. The decrease in R, which results in a decrease in Pe and an increase in the segregation scale L, leads to a decrease in segregation over the simulated length, especially for the medium size particles, which only minimally segregate with respect to small and large particles because their relative size ratios are small. Figure D.1 (b) shows a similar particle mixture to that shown in figure 2.4 but with a steeper chute incline ($\theta = 29\,^\circ$) and higher flow rate ($q = 17000\ \mathrm{mm}^2/\mathrm{s}$). The resulting thicker flowing layer δ leads to an advection dominated regime where particles flow out of the simulated region before they fully segregate ($\tilde{x} \ll 1$). The details of the advection, diffusion, and segregation time scales are discussed in section 2.5. In addition, to show that the model works for a larger range of R and high q, the predictions of the model are compared with simulation for $R = 1 : 2 : 3.5$ for different θ and q in figure D.1 (c,d). The model

predictions are consistent with DEM simulations in both cases even though $R = 3.5$ is slightly out of the range of applicability for equation 2.4. We note that for the two cases with the highest flow rates (D.1 (b,d)), there are slight deviations between the model and simulation, which are likely due to a slight dependence of the velocity profile on streamwise position, especially in the region close to the free surface [110], which differs from the model's fully developed velocity profile assumption. We further compare the predictions of the model with $R = 1 : 2 : 3$ but with a smaller absolute particle diameter, $\alpha_s = 1\,\text{mm}$, in figure D.1 (e), and, again, the predictions of the model agree well with the DEM simulation. From the DEM simulations presented in figures 2.4 and D.1, it is evident that the model is effective over a wide range of flow and particle conditions. Thus, it is possible to confidently explore the continuum model to analyze the impact of operating conditions on segregation over a range of dimensionless parameters.

Table D.1. Parameters for DEM simulations shown in figure D.1. $\alpha_s = 2\,\text{mm}$ for (a-d) and $\alpha_s = 1\,\text{mm}$ for (e). T is the gap thickness.

Fig D.1	θ	T (mm)	R	q (mm^2/s)	δ (mm)	velocity	L (m)	Pe
(a)	26.5°	25	1 : 1.2 : 1.5	3400	23	Linear	2.4	12
(b)	29°	35	1 : 1.6 : 2.5	17000	45	Exponential	4.7	22
(c)	22°	35	1 : 2 : 3.5	3200	24	Bagnold	0.85	21
(d)	29°	35	1 : 2 : 3.5	18000	44	Exponential	2.9	21
(e)	29°	15	1 : 2 : 3	2800	16	Linear	0.90	10

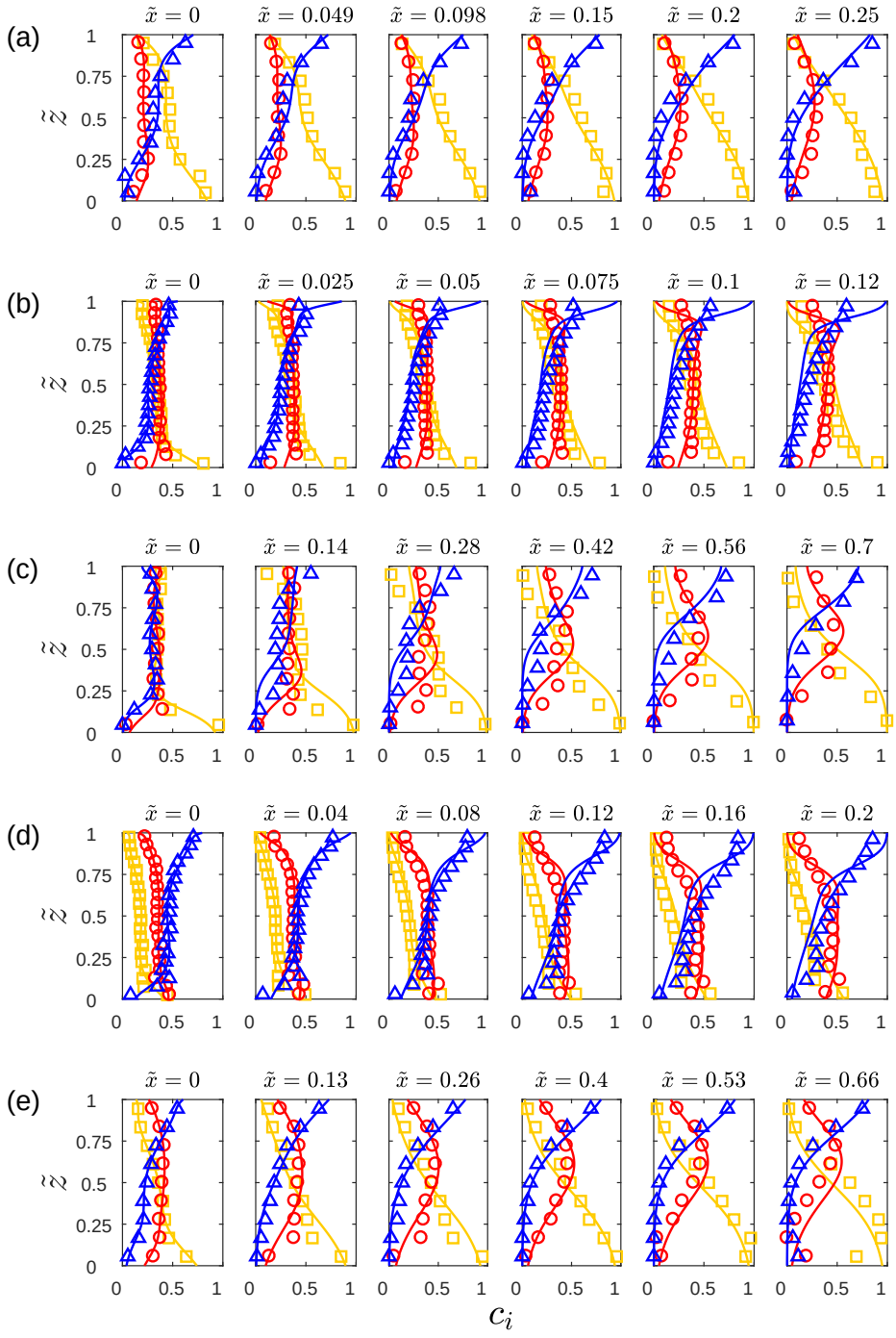

Figure D.1. Comparisons of concentration profiles from DEM simulations and the continuum model for tridisperse chute flow under different operating conditions at different streamwise positions. See table D.1 for operating conditions.

APPENDIX E

Bounded heap flow kinematics

To implement the polydisperse segregation model, the velocity profile, flowing layer depth and diffusion coefficient are needed. Here, these characteristics of the flow are measured from the DEM simulations. As suggested previously [27], an exponential expression $f(z) = e^{kz/\delta}$ provides an accurate approximation to the velocity profile, where k is a scaling constant. The full velocity profiles based on $f(z)$ are:

$$u = \frac{kq}{\delta(1-e^{-k})}\left(1-\frac{x}{L}\right)e^{kz/\delta}$$
$$w = \frac{q}{L(1-e^{-k})}\left(e^{kz/\delta}-1\right). \tag{E.1}$$

Additionally, equations 3.4 and E.1 are non-dimensionalized as follows:

$$\tilde{x} = \frac{x}{L},\ \tilde{z} = \frac{z}{\delta},\ \tilde{u} = \frac{u}{2q/\delta} \text{ and } \tilde{w} = \frac{w}{2q/L}. \tag{E.2}$$

In this way, the domain (the flowing layer) is transformed into a square ($0 \leq \tilde{x} \leq 1$ and $0 \leq \tilde{z} \leq 1$), and the dimensionless velocities ($\tilde{u}$ and $\tilde{w}$) can be expressed as:

$$\tilde{u} = \frac{k}{2(1-e^{-k})}\left(1-\tilde{x}\right)e^{k\tilde{z}}$$
$$\tilde{w} = \frac{1}{2(1-e^{-k})}\left(e^{k\tilde{z}}-1\right). \tag{E.3}$$

Figure E.1 shows the kinematics of a polydisperse log-normal distribution of particles (1 mm $\leq \alpha \leq$ 4 mm, $\sigma = 0.3$) with $q = 1700$ mm^2 s^{-1} from DEM simulations of bounded heap flow (Figure 3.2). Representative streamwise velocity profiles at different streamwise locations are shown in figure E.1(a). The streamwise velocity decreases rapidly from the free surface ($z = 0$) and then decreases more slowly in the lower portion of the flowing

layer to the quasi-static region where particles are deposited on the heap. The streamwise surface velocity u_s decreases nearly linearly with the streamwise position as shown in figure E.1(b). The streamwise velocity profiles at different streamwise locations collapse onto a single curve, as shown in figure E.1(c) when the streamwise velocity is normalized by the local surface velocity and z is normalized by the local flowing layer thickness [26]. Figure E.1(d) compares normal velocities from simulation with the analytic form of w/v_r. In the coordinate system moving upward with the rise velocity, v_r, the normal velocity is zero on the free surface ($\tilde{z} = 0$) and decreases to $-v_r$ at the bottom of the flowing layer $\tilde{z} = -1$. Because normal velocity is typically an order of magnitude smaller than the streamwise velocity, the data are more scattered especially on the free surface of the flow ($\tilde{z} = 0$), where effects of small particle bouncing become more evident. Nevertheless, reasonable agreement between simulation and equation E.3 is achieved.

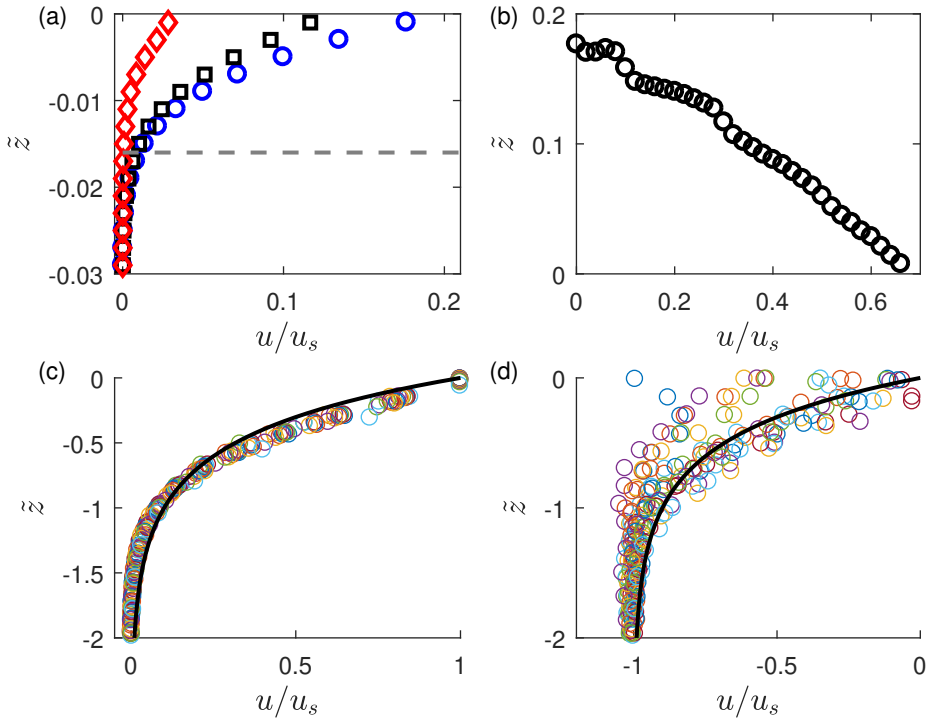

Figure E.1. Kinematics of a polydisperse log-normal distribution of particles (1 mm $\leq \alpha \leq$ 4 mm, $\sigma = 0.3$) from DEM simulations of bounded heap flow with $q = 1600$ mm^2 s^{-1}. (a) Streamwise velocity profiles vs. depth at three different streamwise locations $x = 0, 0.3, 0.6$ m. Gray dashed line represents the bottom of the flowing layer. (b) Surface velocity u_s decreases linearly with streamwise location. (c) Dimensionless streamwise velocity vs. dimensionless depth at different streamwise locations ($0.25 \leq x \leq 0.68$ m). The solid curve is $u/u_s = e^{k\tilde{z}}$. (d) Scaled normal velocity w/v_r in the depth direction at different streamwise locations ($0.25 \leq x \leq 0.68$ m). The solid curve is $w/v_r = e^{k\tilde{z}-1}$.

APPENDIX F

Tumbler flow kinematics

There have been many detailed studies of flow kinematics in tumblers [69, 81, 2, 11, 47, 74, 90]. The velocity field in the flowing layer is typically assumed to have a constant shear rate [47, 74, 90], yielding the following velocity field:

$$u(x,z) = \begin{cases} \omega\left(\frac{R^2}{\delta_0^2} - 1\right)[z + \delta(x)] & \text{if } z > -\delta(x), \\ \omega z & \text{if } z \leq -\delta(x), \end{cases} \tag{F.1}$$

$$w(x,z) = \begin{cases} \omega\left(1 - \frac{\delta_0^2}{R^2}\right)\frac{xz}{\delta(x)} & \text{if } z > -\delta(x), \\ -\omega x & \text{if } z \leq -\delta(x), \end{cases} \tag{F.2}$$

where R is the tumbler radius, u and w are the velocity components in the streamwise (x) and normal (z) directions, respectively, and ω is the rotation rate. Here $\delta(x)$ is the flowing layer thickness at streamwise location x and is defined [69, 74, 90] as

$$\delta(x) = \delta_0\sqrt{1 - \left(\frac{x}{R}\right)^2}, \tag{F.3}$$

where δ_0 is the maximum flowing layer thickness and is measured directly from DEM simulation. As indicated in a previous study [90], the velocity field given by equations F.1 and F.2 is an approximation, and there is a discontinuity near the bottom of the flowing layer. Nevertheless, equations F.1 and F.2 are sufficient for the modeling approach if δ_0/R is not too large [90]. From equation F.1, the surface velocity is

$$u_s = \omega\left(\frac{R^2}{\delta_0} - \delta_0\right)\sqrt{1 - \left(\frac{x}{R}\right)^2}. \tag{F.4}$$

To implement the polydisperse segregation model based on this flow model, all that is needed are the maximum flowing layer thickness, δ_0, and diffusion coefficient, D, for the given rotation speed, ω, and tumbler radius, R. The velocity field and local flowing layer thickness come from equations F.1, F.2, and F.3. In this study, we measure δ_0 as the maximum depth at which the streamwise velocity is 5% of the surface velocity by averaging over 3 s of rotation after the mixture reaches its dynamic angle of repose. To non-dimensionalize equations F.1 and F.2, lengths are scaled by R and time is scaled by $\frac{1}{\omega}$. Dimensionless variables are denoted with a tilde. The dimensionless velocities in the flowing layer (equation F.3) are

$$\left.\begin{aligned} \tilde{u}(\tilde{x},\tilde{z},\epsilon) &= \tfrac{1-\epsilon^2}{\epsilon^2}\left(\tilde{z}+\epsilon\sqrt{1-\tilde{x}^2}\right) \\ \tilde{w}(\tilde{x},\tilde{z},\epsilon) &= \tfrac{1-\epsilon^2}{\epsilon}\tfrac{\tilde{x}\tilde{z}}{\sqrt{1-\tilde{x}^2}}, \end{aligned}\right\} \tag{F.5}$$

where $\epsilon = \delta/R$ is the dimensionless flowing layer depth. As shown in figure F.1(a), the surface velocity from the DEM simulations matches equation F.4 reasonably well. In figure F.1(b), the streamwise velocity from the DEM simulation decreases approximately linearly as z decreases, matching equation F.1 reasonably well. The discrepancies are likely due to the simplifications assumed in equations F.1 and F.2, as discussed previously. The diffusion coefficient D is based on the dependence of D on the shear rate in bounded heap flow [89, 27] using the average shear rate of the velocity field given in equation F.1.

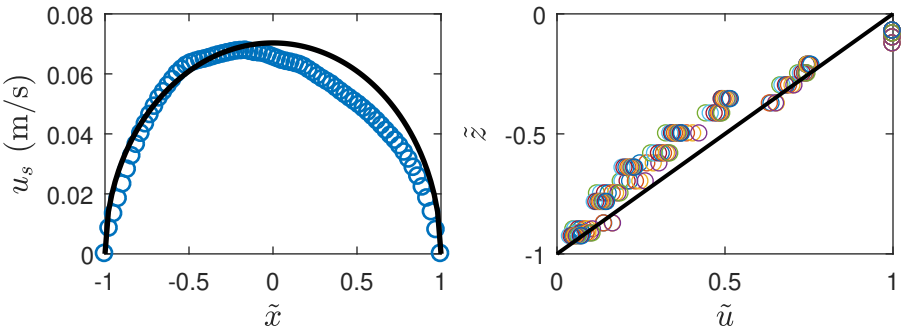

Figure F.1. (a) Surface velocity $u(x, 0)$ vs. streamwise position $\tilde{x}$. (b) Dimensionless streamwise velocity vs. dimensionless depth at different streamwise locations ($-1 \leq \tilde{x} \leq 1$).

APPENDIX G

Hopper discharge flow kinematics

To apply the polydisperse segregation model to hopper flow, the velocity profiles in the flowing layer and the bulk region are needed. Even though the velocity profiles have been tested in a previous study for size bidisperse hopper flow [115], it is unclear whether the same scalings will apply size polydisperse hopper flow. To resolve this, we first validate the velocity field using polydisperse hopper flow DEM simulation, and then apply the model to solve the continuum model using the validated velocity field.

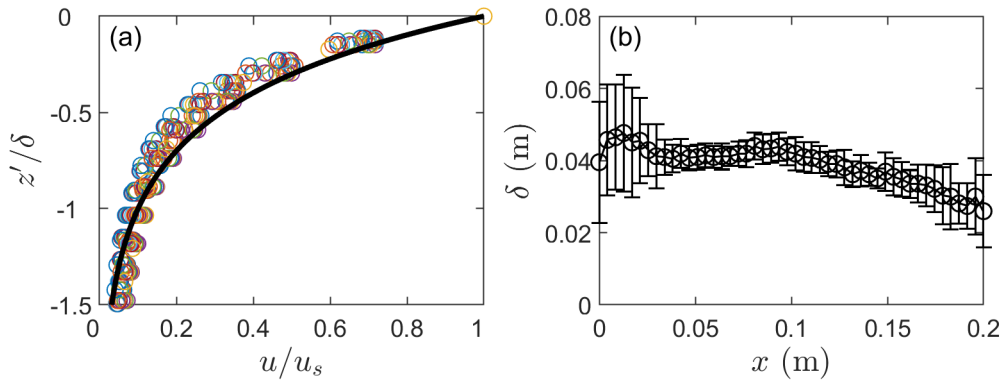

Figure G.1. Flow kinematics of truncated log-normal size distribution mixture with mean $\ln(\tilde{\alpha}) = 0.27$, $\sigma = 0.3$ and $0.5 \leq \tilde{\alpha} \leq 1.5$ from DEM simulations of hopper discharge in the surface flowing layer at $t = 2$ s. (a) Streamwise velocity profiles vs. depth at different streamwise locations. Black curve represents $u/u_s = e^{kz'/\delta}$. (b) Flowing layer thickness vs. streamwsie position

Figure G.1 shows the kinematics within the flowing layer of a mixture with a truncated log-normal size distribution with mean $\ln(\tilde{\alpha}) = 0.27$, $\sigma = 0.3$ and $0.5 \leq \tilde{\alpha} \leq 1.5$ from DEM simulations of hopper discharge flow. In the free surface flowing layer, the largest streamwise (horizontal) velocity occurs at the free surface ($z = 0$), and the velocity decreases in the depth direction z. We define the flowing layer thickness δ as the depth where $u = 0.1u_s$, where u_s is the free surface streamwise velocity. Representative dimensionless streamwise velocity (u/u_s) at different streamwise locations (different colors) is plotted against dimensionless depth (z/δ). The velocity decreases rapidly at the free surface ($z/\delta = 0$), and then slowly close to the bottom of the flowing layer ($z/\delta = -1$). Previous studies [115, 27] suggested that an exponential velocity profile $u/u_s = e^{kz/\delta}$ provides a reasonable approximation to the velocity profile in the flowing layer, where $k = 2.3$ is a scaling constant. The streamwise velocity profiles at different streamwise locations collapse onto this exponential velocity profile curve, as shown in figure G.1(a). Figure G.1(b) further shows the flowing layer thickness across different streamwise locations for the left half of the hopper averaged over 2 s, and the error bars represent one standard deviation. The flowing thickness variances close to the hopper side wall ($x \approx 0$ m) are larger than the variances in the hopper, which is likely due to the boundary effects on the sidewall. Also, the flowing thickness standard deviations increase slightly at hopper center ($x \approx 0.2$ m) where the two opposing surface flows meet. Nevertheless, the constant average flowing layer thickness is a reasonable first order approximation.

Figure G.2 compares the bulk velocity profiles between DEM simulation and the kinematic model calculation (equation 5.4) and DEM simulation of size polydisperse for hopper discharge bulk flow kinematics at different depths (different colors) for the left half

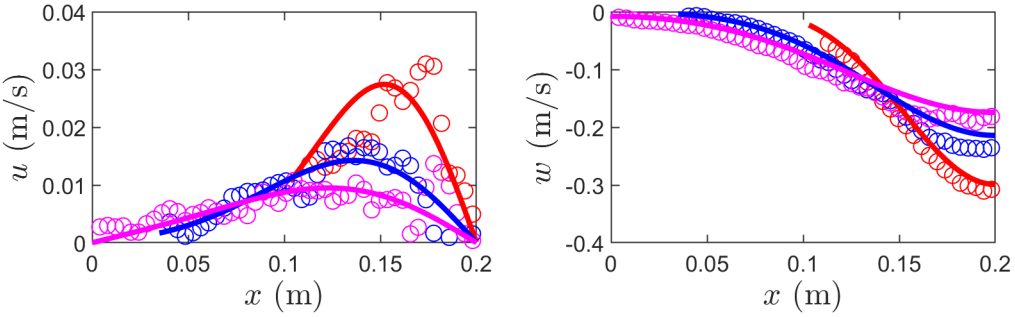

Figure G.2. Velocity comparison between DEM simulation (circles) and the corresponding kinematic model predictions (curves) for bulk flow velocity profiles of the left half of the hopper flow with $W = 0.4$ m, $W_o = 0.06$ m, $\beta = 65°$, and $H_v + H_c = 0.84$ m. (a) Streamwise velocity at $z = 0.4H_c$ (red), $z = 0.8H_c$ (blue), and $z = 1.2H_c$ (magenta). (b) Vertical velocity at $z = 0.4H_c$ (red), $z = 0.8H_c$ (blue), and $z = 1.2H_c$ (magenta).

of the hopper. At almost all depths, the model predictions agrees well with the DEM simulations results. Particles move toward the hopper center ($x = 0.2$ m) and meet the particles from the opposite side at the center. Additionally, particles near the sidewalls also move toward the outlet as opposed to forming a stagnant zone near the sidewalls. As the particles move toward the outlet, the streamwise velocity starts to deviate from the kinematic model prediction slightly ($z = 0.4H_c$). This is likely due to the simplification we made for the outlet velocity. That is, for the vertical boundary condition, we assume that there is a uniform outlet velocity, $w(x, 0) = q_d/W_0$, so that no additional parameters are needed. Nevertheless, the kinematic model gives relatively good agreement with DEM simulations as shown in figure G.2.